The thermal and rheological state of the Central Andes and its relationship to active deformation processes

---

Federico Ibarra, Lic.

Univ.-Diss.

zur Erlangung des akademischen Grades
"doctor rerum naturalium"
(Dr. rer. nat.)
in der Wissenschaftsdisziplin "Geologie"

eingereicht an der
Mathematisch-Naturwissenschaftlichen Fakultät
Institut für Geowissenschaften
der Universität Potsdam

und

Sektion 4.5 Sedimentbeckenanalyse
Deutsches GeoForschungsZentrum Potsdam

Ort und Tag der Disputation: Potsdam, 25/03/2021

BetreuerInnen: Prof. Manfred R. Strecker, PhD
Prof. Dr. Magdalena Scheck-Wenderoth

GutachterInnen: Priv. Doz. Dr. Sascha Brune
Dr. Laura Beatriz Giambiagi
Prof. Dr. Augusto Ernesto Rapalini

Published online on the
Publication Server of the University of Potsdam:
https://doi.org/10.25932/publishup-50622
https://nbn-resolving.org/urn:nbn:de:kobv:517-opus4-506226

Declaration of Authorship

I hereby declare that this dissertation was prepared independently by the author, Federico Ibarra, without the use of any other means than the specified. All ideas derived from other sources are indicated as such. This work has been submitted only to the University of Potsdam and the University of Buenos Aires, in compliance with an individual cotutelle agreement.

Abstract

The Central Andes region in South America is characterized by a complex and heterogeneous deformation system. Recorded seismic activity and mapped neotectonic structures indicate that most of the intraplate deformation is located along the margins of the orogen, in the transitions to the foreland and the forearc. Furthermore, the actively deforming provinces of the foreland exhibit distinct deformation styles that vary along strike, as well as characteristic distributions of seismicity with depth. The style of deformation transitions from thin-skinned in the north to thick-skinned in the south, and the thickness of the seismogenic layer increases to the south. Based on geological/geophysical observations and numerical modelling, the most commonly invoked causes for the observed heterogeneity are the variations in sediment thickness and composition, the presence of inherited structures, and changes in the dip of the subducting Nazca plate. However, there are still no comprehensive investigations on the relationship between the lithospheric composition of the Central Andes, its rheological state and the observed deformation processes. The central aim of this dissertation is therefore to explore the link between the nature of the lithosphere in the region and the location of active deformation. The study of the lithospheric composition by means of independent-data integration establishes a strong base to assess the thermal and rheological state of the Central Andes and its adjacent lowlands, which alternatively provide new foundations to understand the complex deformation of the region. In this line, the general workflow of the dissertation consists in the construction of a 3D data-derived and gravity-constrained density model of the Central Andean lithosphere, followed by the simulation of the steady-state conductive thermal field and the calculation of strength distribution. Additionally, the dynamic response of the orogen-foreland system to intraplate compression is evaluated by means of 3D geodynamic modelling.

The results of the modelling approach suggest that the inherited heterogeneous composition of the lithosphere controls the present-day thermal and rheological state of the Central Andes, which in turn influence the location and depth of active deformation processes. Most of the seismic activity and neo--tectonic structures are spatially correlated to regions of modelled high strength gradients, in the transition from the felsic, hot and weak orogenic lithosphere to the more mafic, cooler and stronger lithosphere beneath the forearc and the foreland. Moreover, the results of the dynamic simulation show a strong localization of deviatoric strain rate second invariants in the same region suggesting that shortening is accommodated at the transition zones between weak and strong domains. The vertical distribution of seismic activity appears to be influenced by the rheological state of the lithosphere as well. The depth at which the frequency distribution of hypocenters starts to decrease in the different morphotectonic units correlates with the position of the modelled brittle-ductile transitions; accordingly, a fraction of the seismic activity is located within the ductile part of the crust. An exhaustive analysis shows that practically all the seismicity in the region is restricted above the 600°C isotherm, in coincidence with the upper temperature limit for brittle behavior of olivine. Therefore, the occurrence of earthquakes below the modelled brittle-ductile could be explained by the presence of strong residual mafic rocks from past tectonic events. Another potential cause of deep earthquakes is the existence of inherited shear zones in which brittle behavior is favored through a decrease in the friction coefficient. This hypothesis is particularly suitable for the broken foreland provinces of the Santa Barbara System and the Pampean Ranges, where geological studies indicate successive reactivation of structures through time. Particularly in the Santa Barbara System, the results indicate that both mafic rocks and a reduction in friction are required to account for the observed deep seismic events.

Zusammenfassung

Die südamerikanischen Zentralanden zeichnen sich durch eine komplexe und heterogene Deformationsstruktur aus. Erdbebenaufzeichnungen und geologisch-tektonische Kartierungen zeigen, dass innerhalb der Südamerikanischen Platte die Hauptdeformation entlang beider Gebirgsränder stattfindet. Zusätzlich variiert die Art der aktiven Deformation und die Tiefenverteilung von Erdbeben im östlichen Vorland von Nord nach Süd. Dabei erstreckt sich das Auftreten von Erdbeben, auch seismogene Zone genannt, über einen zunehmend größeren Tiefenbereich. Die tektonische Deformation schließt ebenso, nach Süden hin zunehmend, größere Tiefenbereiche der Erdkruste mit ein. Erklärungen dieses Verhaltens auf der Grundlage von geologisch-geophysikalischen Untersuchungen sowie von numerischen Modellen legten bisher nahe, dass die Unterschiede der Sedimentmächtigkeiten, das Vorhandensein ererbter tektonischer Strukturen und die Variation des Eintauchwinkels der unter Südamerika abtauschenden Nazca-platte als Gründe dafür in Frage kommen. Allerdings gab es bislang keine Untersuchungen dazu, welche Rolle die lokale Zusammensetzung der Lithosphäre sowie ihr Fließverhalten dabei spielen. Das Hauptziel dieser Dissertation ist daher, den Zusammenhang zwischen Lithosphäreneigenschaften in der Region und dem Auftreten gewisser Deformationstypen an der Erdoberfläche zu untersuchen. Die Zuhilfenahme voneinander unabhängiger, geophysikalischer Beobachtungsparameter ermöglicht eine Beurteilung des thermischen und rheologischen Zustands der Zentralanden und angrenzender Vorlandgebiete, und damit eine bessere Einschätzung der komplexen Deformation. Der Workflow dieser Dissertation startet zunächst mit der Erstellung eines 3D-Dichtemodells auf der Grundlage von geologischen und seismologischen Beobachtungen, das zusätzlich mit Schweredaten untermauert wird. Dies ermöglicht die Simulation der räumlichen variierenden, stationären Wärmeleitung in der Lithosphäre und die Berechnung der mechanischen Stabilität. Schlussendlich werden diese Erkenntnisse in ein dreidimensionales geodynamisches Modell übertragen, welches Aufschluss über die Kompressionsdeformation zwischen dem Gebirge und dessen Vorland Auskunft gibt.

Die Modellergebnisse zeigen, dass die ungleichmäßige Zusammensetzung der Lithosphäre der Schlüssel für den heute beobachtbaren thermischen und rheologischen Zustand der Zentralanden ist und damit auch der wichtigste Faktor zur Erklärung der räumlichen Variation und Tiefenverteilung aktiver Deformationsprozesse. Die meisten Erdbeben und neotektonischen Strukturen sind in Bereichen zu finden, für die der stärkste Festigkeitskontrast modelliert wurde. Dies betrifft den Übergang von felsischer, heißer und daher weicher Gebirgslithosphäre des Hauptkamms zu der eher mafischen, kalten und festeren Lithosphäre des Vorlands. Außerdem ergab die dynamische Simulation eine räumliche Zentrierung der zweiten Invariante der Rate des deviatorischen Spannungstensors in der gleichen Region. Damit kann davon ausgegangen werden, dass die stärkste Stauchung genau in diesem Übergang zwischen weichem und festen Material abläuft. Die Erdbebenverteilung in der Vertikalen scheint ebenso vom rheologischen Zustand der Lithosphäre abzuhängen. Für die verschiedenen morphotektonischen Provinzen korreliert die Tiefe, ab der die Erdbebenhäufigkeit abnimmt, jeweils mit der Lage der Übergangszone zwischen Sprödbruchdeformation und duktiler Verformung. Dadurch tritt ein Teil der Erdbeben im duktil verformten Bereich der Erdkruste auf. Weitere Untersuchungen zeigen, dass praktisch die gesamte Seismizität oberhalb der 600°C Isotherme abläuft, welche das obere Temperaturlimit für das Sprödbruchverhalten von Olivin darstellt. Daher kann das Auftreten von Erdbeben unterhalb der modellierten Übergangszone von Sprödbruch zu duktiler Deformation mit dem Vorhandensein von mafischen Gesteinsanteilen erklärt werden, welche als Überbleibsel aus vorangegangenen tektonischen Ereignissen installiert wurden. Eine weitere mögliche Erklärung für solche tiefen Erdbeben ist die Existenz von internen Scherzonen, entlang welcher Sprödbruchdeformation durch herabsetzen des Reibungswiderstandes erleichtert wird. Diese Hypothese lässt sich insbesondere im Santa Barbara System und den Sierras Pampeanas anwenden, da geologische Studien bereits die sukzessive Reaktivierung von Strukturen über einen längeren Zeitraum identifizierten. Insbesondere für das Santa Barbara System zeigen die hier vorgestellten Ergebnisse, dass beide Faktoren, mafische Gesteinsanteile und die Reduzierung des Reibungswiderstandes, nötig sind, um das Auftreten der zu beobachtenden größeren Erdbebentiefe zu erklären.

Contents

List of Figures

List of Tables

Chapter 1. Introduction

In this section, the topic and primary aim of the dissertation are introduced. A short review of the state of the art of the research topic is first presented, together with the scientific questions that arise and are addressed in this dissertation. Then, the general workflow and organizational structure of the dissertation are briefly described.

1.1. Research topic and scientific questions

Large orogenic belts influence not only the local and far-field stress state of the lithosphere, but also magmatic and resource-generating processes, erosion, sedimentation, seismicity, the climate, and many other geological and atmospheric phenomena (e.g., Barazangi and Isacks, 1976; Masek et al., 1994; Molnar et al., 1993; Molnar and Tapponnier, 1975; Oncken et al., 2006; Richter et al., 1992; Royden, 1996; Ruddiman et al., 1997; Sillitoe, 1972; Yin and Harrison, 2000). The synergies between many of the associated processes, but also the role of lithospheric-scale heterogeneities, inherited from paleo-tectonic processes and reactivated under present-day stress-field conditions, are pivotal for the evolution of orogens (e.g., Butler et al., 2006; Kley et al., 1999; Marshak et al., 2003; Vauchez et al., 1998; Vauchez and Barruol, 1996). In this regard, the study of the physical state of the lithosphere is essential, since composition and temperature control the rheology of mountain belts, and consequently their deformation and the development of topography and surface processes.

The thermal evolution of orogens has been widely investigated from the perspective of metamorphic history and thermo-mechanical modelling. Currie and Hyndman (2006) have shown that, particularly in subduction zone backarcs, the orogenic lithospheres are hot despite the cooling effect of the subducting plates. Hyndman et al. (2005) suggested in their review of mobile belts and orogenic heat that such elevated temperatures are a major factor in mountain building processes because of their weakening effect on the lithosphere. With respects to the heat sources, some authors suggested that shallow

asthenosphere convection is responsible for the observed elevated geotherms beneath orogens (i.e. incoming heat-flow from the mantle), ignoring any residual heat and radiogenic heat production (e.g., Hyndman et al., 2005; Platt and England, 1994). However, other authors stressed that, for particular scenarios, the internal crustal heat sources, such as radioactive decay and viscous dissipation, are the dominant heat sources accounting for the elevated geotherms (e.g., Huerta et al., 1998; Sandiford and McLaren, 2002). In this line, Vanderhaeghe et al. (2003) have shown by means of 2D thermo-mechanical modelling that a thickened felsic crust can produce a significant temperature increment after 10-20 m.y. of incubation.

Although temperature is undoubtedly an important parameter because it controls ductile creep in rocks, their compositions as well as the state of crust-mantle coupling are also significant factors affecting the strength of the lithosphere (e.g., Burov et al., 1998; Burov, 2010; Burov and Watts, 2006; Ranalli, 2003, 1997; Ranalli and Adams, 2013). Furthermore, taking into consideration that the radiogenic heat production of rocks strongly depends on composition (e.g., Hasterok and Webb, 2017; Vilà et al., 2010), the latter has a double impact on lithospheric strength because it determines the contribution of radiogenic heat to the heat budget.

The first rheological models of the lithosphere have explored the distribution of strength with depth in synthetic 1D vertical profiles (known as yield strength envelopes or YSEs) for reference geotherms, rock compositions and lithospheric structures (e.g., Goetze and Evans, 1979; Kirby, 1983; Ranalli and Murphy, 1987). The two main models of possible rheological profiles for the lithosphere that have been published are known as the *jelly sandwich* model and the *crème brûlée* model; the former is characterized by the presence of a weak lower crust between a strong upper crust and a strong lithospheric mantle, while the latter consists of a strong upper crust with a weak lower crust and a weak lithospheric mantle (e.g., Burov and Watts, 2006; Jackson, 2002).

There has been debate over recent decades regarding the rheological stratification of the lithosphere and its correlation with the thickness of the seismogenic layer (T_S). On the basis of seismic observations and thermo-mechanical models, different authors have questioned the applicability of the *jelly sandwich* and *crème brûlée* models, suggesting that only one or the other are valid physical representations of the lithosphere (e.g., Burov, 2010; Jackson, 2002). Comparative analyses of intraplate seismicity and rheological stratification have revealed a correlation between frequency-depth distributions of earthquakes and lithospheric strength profiles, with peak seismicity occurring close to brittle-ductile transitions and cut-off depths of 10-20 km in most regions (e.g., Doser and Kanamori, 1986; Ito, 1990). However, the occurrence of intermediate to deep crustal earthquakes beneath the brittle-ductile transition in some regions has cast doubt over this correlation, leading some authors to propose variations in slip behavior with depth and different mechanisms for seismogenesis (e.g., Deichmann, 1992; Hobbs et al., 1986; Lamontagne and Ranalli, 1996; Petley-Ragan et al., 2019; Prieto et al., 2017; Scholz, 1988; Tse and Rice, 1986).

The lack of consensus suggests that there is no unique rheological profile for the lithosphere and that its relationship to T_S is not always straightforward. This means that each region needs to be investigated separately in order to understand its past and present deformation processes. The Central Andes region in South America is a particularly interesting area in which to explore the different hypotheses regarding the relationship between lithospheric strength and T_S because of its complex and heterogeneous orogenic system with variable deformation styles along and across strike, as well as different magmatic and sedimentary records, and inherited anisotropies (e.g., Allmendinger et al., 1997; Ramos, 1999).

Research into crustal seismicity and neotectonic structures in the Central Andes has shown that most of the recent activity has been concentrated along the margins of the orogen and that the different morphotectonic units exhibit distinct deformation styles (projects PUDEL, PUNA ’97, PISCO ‘94 and ANCORP ’96; e.g., Allmendinger et al., 1997;

Graeber, 1997; Heit et al., 2007b; Mulcahy et al., 2014; Rietbrock et al., 1997; Schurr et al., 1999; Proyecto Multinacional Andino: Geociencia para las Comunidades Andinas, 2008). Uppermost controls (e.g. sedimentary thickness and composition, inherited structures) and slab geometry have been generally invoked to explain the observed deformation patterns and styles (e.g., Kley and Monaldi, 2002; Ramos et al., 2002), however, it is well known that the more deep-seated spatiotemporal distribution of lithospheric rheological properties and temperatures have an effect on tectonic deformation (e.g., Lowe and Ranalli, 1993; Mareschal, 1994; Moisio and Kaikkonen, 2015; Ranalli, 1997). Since these parameters are directly related to rock composition and lithosphere thickness, a model of the configuration of the lithosphere beneath the Central Andes is required to better understand the regional variations in deformation. Although a large variety of models have been used previously to investigate the structures, seismicity, thermal field and lithospheric composition of the region (e.g., Babeyko et al., 2006, 2002; Eichelberger et al., 2015; Gerbault et al., 2003; Hindle et al., 2005; Metcalf and Kapp, 2015; Mulcahy et al., 2014; Ouimet and Cook, 2010; Prezzi et al., 2009; Salomon, 2018; Tassara et al., 2006; Yang and Liu, 2003), none have fully investigated rheology and thermal field as a function of lithology distribution, nor analyzed their relationships with active deformation processes.

In this dissertation, the thermal and rheological state of the Central Andes is therefore investigated by means of cumulative three-dimensional data-derived models of the lithospheric density configuration, the steady-state conductive thermal field, and the strength distribution. These models provide a base to address the first scientific question, which is how the lithospheric structure and composition shape the temperature and strength distribution in the region. Furthermore, the heterogeneous distribution of seismicity and neotectonic structures is analyzed in light of the modelling results to tackle the second scientific question: do the regional variations in the structure, temperature and rheology of the lithosphere exert any control on the observed active deformation processes.

1.2. Workflow and structure of the dissertation

The core workflow of the dissertation consists in the construction of a 3D data-derived density model of the Central Andes constrained by forward modelling of the Bouguer anomaly, the calculation of the 3D steady-state conductive thermal field, the computation of the 3D strength distribution in the lithosphere, and the analysis of active deformation processes in light of the modelling results. A general geologic framework is first presented in Chapter 2 to introduce to the reader the most important characteristics and tectonic events of the region, necessary to understand the results.

The construction of the density model is the central part of the workflow because the thermal and rheological models build upon it, after parametrization of thermal and rheological properties. A published density model together with a number of geological, geochemical, and geophysical studies were used to construct the density model presented in this dissertation. The most challenging task was to reconcile all the different datasets and establish a criterion to divide the model in units; a detailed description of the modelling procedure is presented in Chapter 3. The resulting lithospheric density configuration is analyzed from the perspective of tectonic evolution.

The parametrization of thermal properties and the calculation of the thermal field are described in Chapter 4. Given the controversy of steady-state simulations of the thermal field for tectonically active regions, the results are extensively discussed and compared to surface heat-flow and temperature data. In addition, an independent insight into the thermal field is computed from the spectral analysis of magnetic anomalies, which provides the depth to the bottom of the magnetic layer, interpreted here as the Curie isotherm.

Moving forward, the rheological state of the region is tackled in Chapter 5. The strength distribution calculated after the parametrization of rheological properties is presented as integrated strength maps and yield strength envelopes to examine lateral and vertical heterogeneities. In order to explore the link between strength profiles of the

lithosphere and effective elastic thickness, the latter is calculated from the strength distribution and the spectral analysis of flexure. Furthermore, the dynamic behavior of the orogen-foreland system in the model is analyzed by means of geodynamic modelling.

Finally, the modelling results are integrated in Chapter 6 to address the relation between the thermal and rheological state of the Central Andes and its active deformation processes. To that end, the distributions of seismicity and neotectonic structures are compiled from global and local datasets and compared against the configuration of temperature and strength throughout the model. The general conclusions of the dissertation are presented in Chapter 7.

Chapter 2. Geologic setting

The region of the Central Andes is part of a subduction-related orogen on the western margin of the South American plate (Figure 2.1). Subduction has been almost continuous since the early Paleozoic, with the region being subjected to alternating periods of compression and extension (e.g., Bock et al., 2000; Coira et al., 2009; Maloney et al., 2013; Ramos, 2010, 2009). The compressive Andean tectonic processes that have resulted in the present-day morphotectonic provinces did not start until the Middle Cretaceous (e.g., Amilibia et al., 2008; Bascuñán et al., 2016; Rossel et al., 2013). The interaction of this latest orogenic pulse, which became prominent during the Cenozoic, with inherited lithospheric structures from former deformation cycles, both compressive and extensional, has produced the complex present-day configuration.

The Central Andes region modelled in this dissertation consist of (from west to east) forearc, volcanic arc, and backarc areas, which are in turn sub-divided into different morphotectonic provinces on the basis of their tectonic evolution (Jordan et al., 1983; Ramos, 1999). The forearc comprises the Coastal Cordillera, the Longitudinal Valley and the Chilean Precordillera, and the volcanic arc is represented by the Western Cordillera. The backarc includes the Andean Plateau (Altiplano-Puna Plateau), the Eastern Cordillera, the Subandean fold-and-thrust belt, the broken-foreland provinces of the compressionaly inverted Santa Barbara System and the basement blocks of the Pampean Ranges, and the undeformed Chaco-Parana foreland basin (Figure 2.2).

The Altiplano-Puna plateau is one of the most remarkable features of the Central Andes. It is the largest plateau developed in a subduction system and the second largest in the world after Tibet (Allmendinger et al., 1997; Lamb, 2000), spanning ~2000 km and ~300 km in N-S and W-E directions, respectively, and with an average elevation of 3700 m (Figure 2.1). At the latitudes of the plateau, approximately 15°S to 28°S, the Nazca plate subducts steeply beneath the South American plate with an average angle of 30°, whereas to the north and south, the plateau is bounded by two flat subduction segments (Isacks, 1988; Jordan et al., 1983).

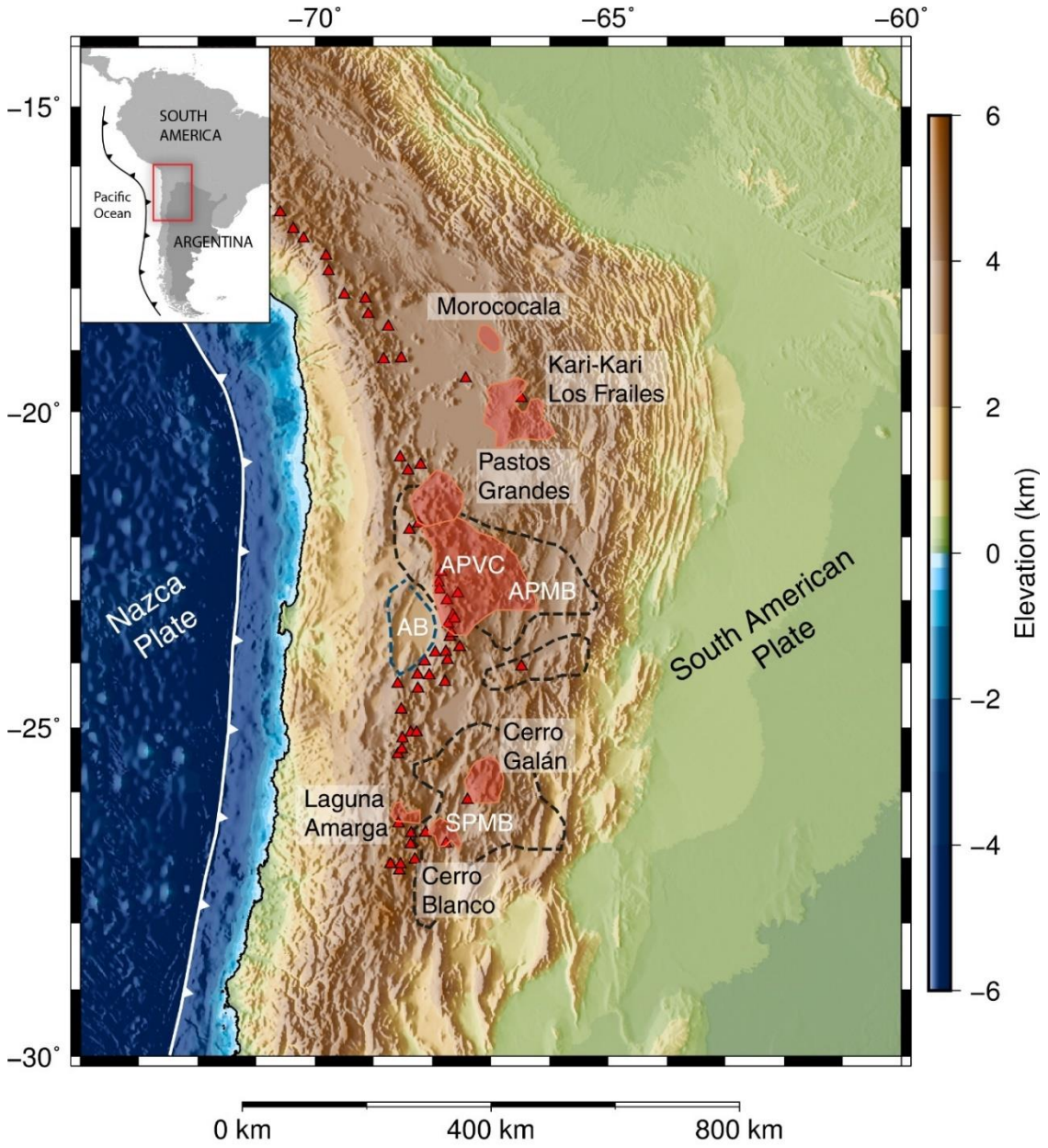

Figure 2.1: Elevation map of the Central Andes and adjacent lowlands showing the distribution of active volcanoes (red triangles – from the Global-Volcanism-Program, 2013), large calderas and volcanic provinces (red patches – compiled from Burns et al., 2015; Guzmán et al., 2014; Kay et al., 2010), regions with anomalous low crustal velocity and resistivity (dashed black lines – compiled from Beck et al., 2015; Bianchi et al., 2013), and a region with high seismic velocity (dashed blue line – after Schurr and Rietbrock, 2004). APVC: Altiplano-Puna Volcanic Complex; APMB: Altiplano-Puna Magma Body; SPMB: Southern Puna Magma Body; AB: Atacama Block.

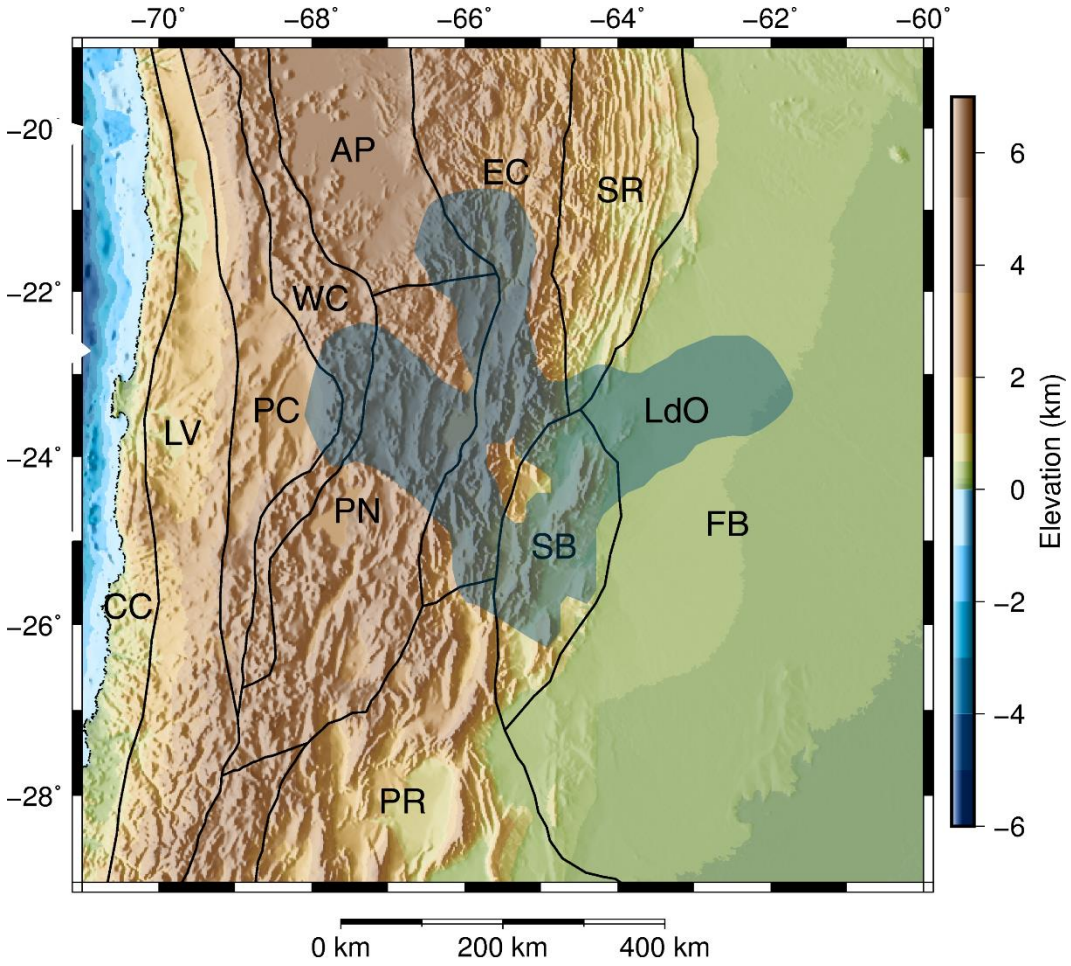

Figure 2.2: Elevation map of the modelled region, showing the boundaries between morphotectonic units (solid black lines – compiled from Jordan et al., 1983, and Ramos 1999) and the main Upper Cretaceous extensional depocenters (blue patch - after Reutter et al., 2006). CC: Coastal Cordillera; LV: Longitudinal Valley; PC: Chilean Precordillera; WC: Western Cordillera; AP: Altiplano; PN: Puna; EC: Eastern Cordillera; SR: Subandean Ranges; SB: Santa Barbara System; PR: Pampean Ranges; FB: Chaco-Paraná foreland basin; LdO: Lomas de Olmedo sub-basin.

2.1. Tectonic evolution

The main tectonic events that have shaped the basement configuration and the Cenozoic deformation characteristics of the Central Andes have been established in several studies, however, reconstruction of the Paleozoic and earlier evolution is problematic due to the scarcity of outcrops (Casquet et al., 2012; DeCelles et al., 2015; Franz et al., 2006; Kay et al., 1994; Ramos, 2008; Riller et al., 2001a; Rossel et al., 2013; Strecker et al., 1989). The assemblage of crustal domains took place in the Neoproterozoic-Cambrian during the last stage of formation of Gondwana; the basement remnants of the Pampean orogeny and the metasedimentary Puncoviscana Formation are records of this construction period (Escayola et al., 2011; Rapela et al., 2007; Trindade et al., 2006). Two end-member models of accretion stand out among the literature, the Pampia-Arequipa-Antofalla model (e.g., Ramos, 2008; Ramos et al., 2010; Figure 2.3, a & b) and the MARA craton model (Casquet et al., 2012; Figure 2.3, c & d). The relevance of the different hypothesis of accretion lies on the present-day distribution of terrane boundaries that could act as weak zones for the emplacement of deformation.

The Early Paleozoic was an orogenic period characterized by extensive regional metamorphism and magmatism. Metamorphic rocks from this period are compositionally uniform, with the prevailing rock types being felsic gneisses and migmatites (e.g., Lucassen et al., 2001, 2000). The magmatic rocks are associated with high-T metamorphism and are dominated by granitoid intrusions that show important involvement of crustal material or directly correspond to crustal melts (e.g., Pankhurst et al., 2000; Pankhurst and Rapela, 1998). Considering the generally felsic composition of the rocks, their geochemical signature, and the areal distribution of the outcrops some authors have proposed the existence of a large orogen, analogous to the present-day Central Andes and its plateau; discussion remains whether the orogen was the result of collision or mere subduction (e.g., Lucassen and Franz, 2005; Franz et al., 2006; Ramos, 2008).

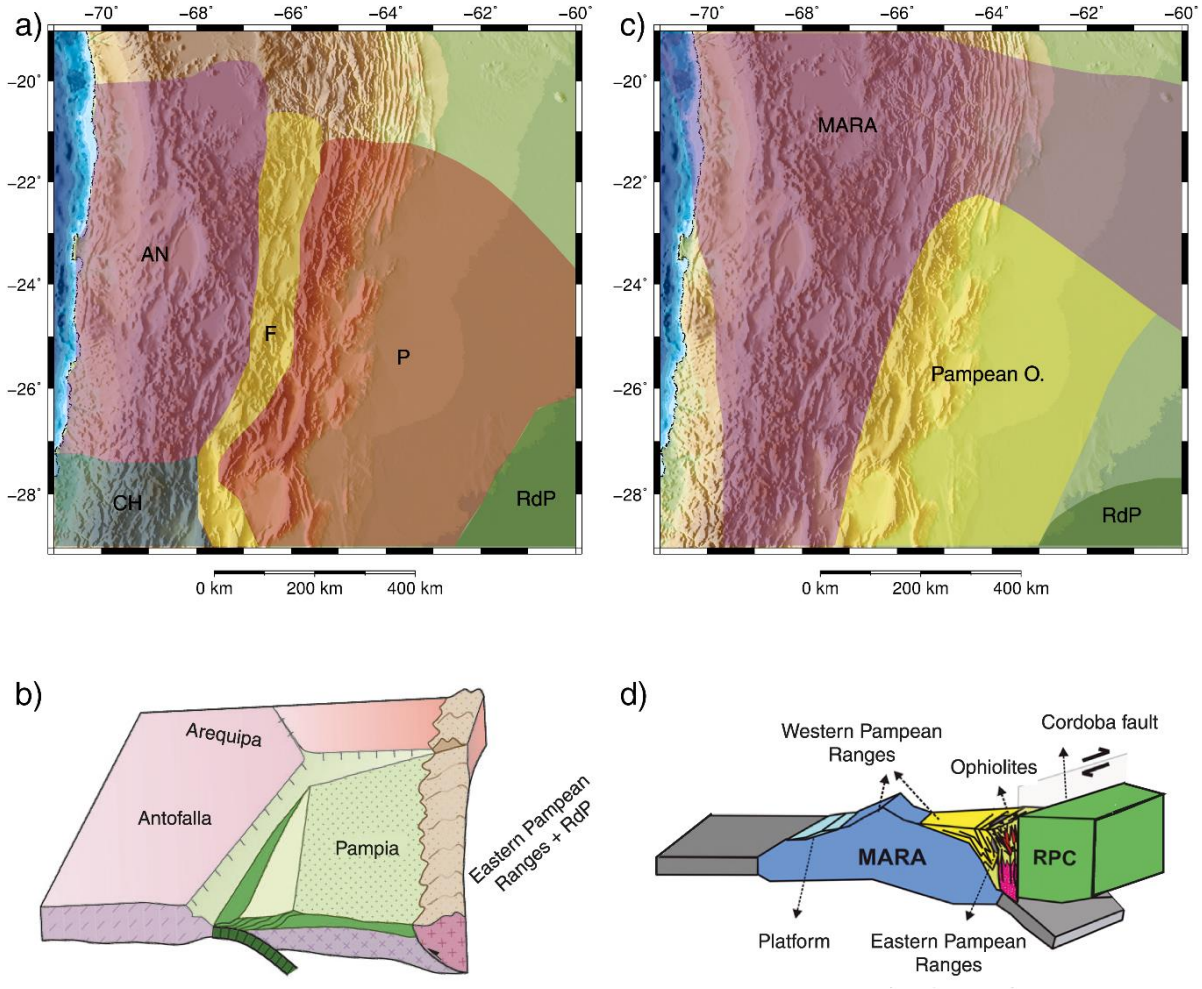

Figure 2.3: (a) Terrane distribution (after Rapalini, 2005) corresponding to the model of accretion of Arequipa-Antofalla shown in (b) (modified from Ramos, 2008). (c) Terrane distribution (after Casquet et al., 2012) corresponding to the model of accretion of MARA shown in (d) (modified from Rapela et al., 2017). AN: Antofalla; P: Pampia; CH: Chilenia; F: Famatina magmatic belt; RdP: Rio de la Plata cratón; Pampean O.: Pampean orogen metasediments.

The Andean Cycle started in the Late Triassic-Early Jurassic, marked by a drastic change in the subduction regime and magmatism. The onset of extension in the arc and backarc was accompanied by widespread and voluminous mantle-derived magmatic activity from the Jurassic to the Early Cretaceous, represented by the mafic rocks in the volcanic La Negra Formation and the coastal batholith (Lucassen et al., 2002; Rossel et al., 2013). As the South American plate increased its velocity towards the trench, compression and subduction erosion took place; subsequently, the volcanic arc migrated progressively eastward from the Late Cretaceous onwards, reaching its present position in the Western Cordillera by the Oligocene (e.g., Franz et al., 2006; Maloney et al., 2013; Schellart, 2017; Scheuber and Reutter, 1992; Figures 2.1 and 2.2).

Coetaneous with the onset of volcanic arc migration and compression in the west, the backarc between 21°S and 26°S experienced an extensional period in the Late Cretaceous-Paleocene (known as Salta Rift), with prevailing N-S trend except for its eastern W-E striking branch (Lomas de Olmedo; Figure 2.2) (e.g., Marquillas and Salfity, 1988). The sedimentary records of the rift system show that it extended throughout northwestern Argentina towards the Chilean Precordillera, along four main depocenters (Tres Cruces, Metán-Alemanía, Lomas de Olmedo, and Say) (e.g., Marquillas et al., 2005; Viramonte et al., 1999). Late Cretaceous basaltic rocks with alkaline affinity containing upper mantle and lower crustal xenoliths are found within the rift deposits, constraining the age of the basin and providing information on its origin (Lucassen et al., 2005, 1999).

From the Oligocene to present, volcanism has concentrated in the Western Cordillera and Altiplano-Puna plateau (e.g., Trumbull et al., 2006). Distribution of magmatism suggests that during the Oligocene-Miocene the slab shallowed and steepened back to its present position progressively from north to south, triggering asthenospheric upwelling and lithosphere delamination (Drew et al., 2009; Kay et al., 2010). Throughout the plateau there are volcanic rocks with arc affinity and Oligocene-Miocene age, large ignimbritic caldera deposits with major crustal contribution and Late Miocene to recent ages, and isolated, volumetrically small, mantle-derived basaltic

volcanics with Late Oligocene to Quaternary ages (Guzmán et al., 2014; Kay et al., 1994; Figure 2.1). The most important ignimbrite "flare-up" produced a major volcanic province, the Altiplano-Puna Volcanic Complex (APVC; de Silva, 1989; Figure 2.1). In association with these deposits, two pronounced low-velocity anomalies have been detected within the crust, interpreted to represent regions that are undergoing metamorphism and partial melting, the Altiplano-Puna Magma Body (APMB; Yuan et al., 2000; Figure 2.2) and the Southern Puna Magma Body (SPMB; Bianchi et al., 2013; Figure 2.2).

2.2. Andean compression

The first compressional stages in the construction of the present-day Andes date back to the Cretaceous (e.g., Bascuñán et al., 2016), in coincidence with the initiation of arc migration. However, the main stages of Andean compression began at ~40 Ma, affecting the entire region of the present-day Andean plateau (e.g., Henriquez et al., 2020; Lamb, 2015; Quade et al., 2015). North of 22°S, the Altiplano was structured between ~30-10 Ma by thin-skinned fold and thrust belts propagating from the Western Cordillera and the Eastern Cordillera; whilst deformation in the Puna started at ~20 Ma and is still active (e.g., Coutand et al., 2001; Elger et al., 2005; McQuarrie et al., 2005; Oncken et al., 2006; Schoenbohm and Strecker, 2009). Strike-slip and compressive fault systems have broken up the region into contractional "basins and ranges" with rhomb-shape geometry (Allmendinger et al., 1997).

The onset and style of deformation along the foreland are heterogeneous as well. The Subandean Ranges are a thin-skinned fold and thrust belt detached from the Paleozoic section of the stratigraphic column, with eastward-younging piggy-back basins and a decollement propagating further east, that started to form at~15-10 Ma (Dunn et al., 1995; Lamb, 2015; McQuarrie, 2002; Mingramm et al., 1979). In contrast, deformation in the broken-foreland provinces of the Santa Barbara System and the Pampean Ranges did not start until ~7 Ma (Löbens et al., 2011; Sobel and Strecker, 2003). The structural

style in the Santa Barbara System is strongly controlled by tectonic inversion of the Salta Rift, close to margin of the plateau (Kley and Monaldi, 2002); while in the Pampean Ranges, deformation is widely distributed and characterized by reverse-fault bounded basement blocks related to a sub-horizontal subduction zone (Ramos et al., 2002).

Information on seismicity over recent decades, as well as on active faulting, has been compiled in various projects, revealing that most of the activity has been focused on the Coastal Cordillera and along the eastern margin of the plateau area as well as in the Pampean Ranges and the Santa Barbara System (projects PUDEL, PUNA ’97, PISCO ‘94 and ANCORP ’96; Graeber, 1997; Heit et al., 2007b; Mulcahy et al., 2014; Proyecto Multinacional Andino: Geociencia para las Comunidades Andinas, 2008; Rietbrock et al., 1997; Schurr et al., 1999; Figure 2.4 and Figure 2.5). The Coastal Cordillera has recorded the deepest events (depths greater than 50 km), and also the largest range of depths because the majority of the earthquakes occur at the subduction interface. Most of the seismicity to the east of the plateau area (Santa Barbara System and Pampean Ranges) is restricted to the upper/middle crust (depths between 10 and 30 km). Within the Puna and the margin of the plateau, the activity is much shallower (up to 15 km depth) and more heterogeneous, with coexisting compression, trans-tension, trans-pression and extension, as indicated by the focal mechanisms (see symbols in Figure 2.5). On the basis of such evidence, together with the high topography and the lack of isostatic compensation, a number of researchers have suggested that the Puna is currently in collapse mode (Allmendinger et al., 1989; Daxberger and Riller, 2015; Montero López et al., 2014; L. Schoenbohm and Strecker, 2009).

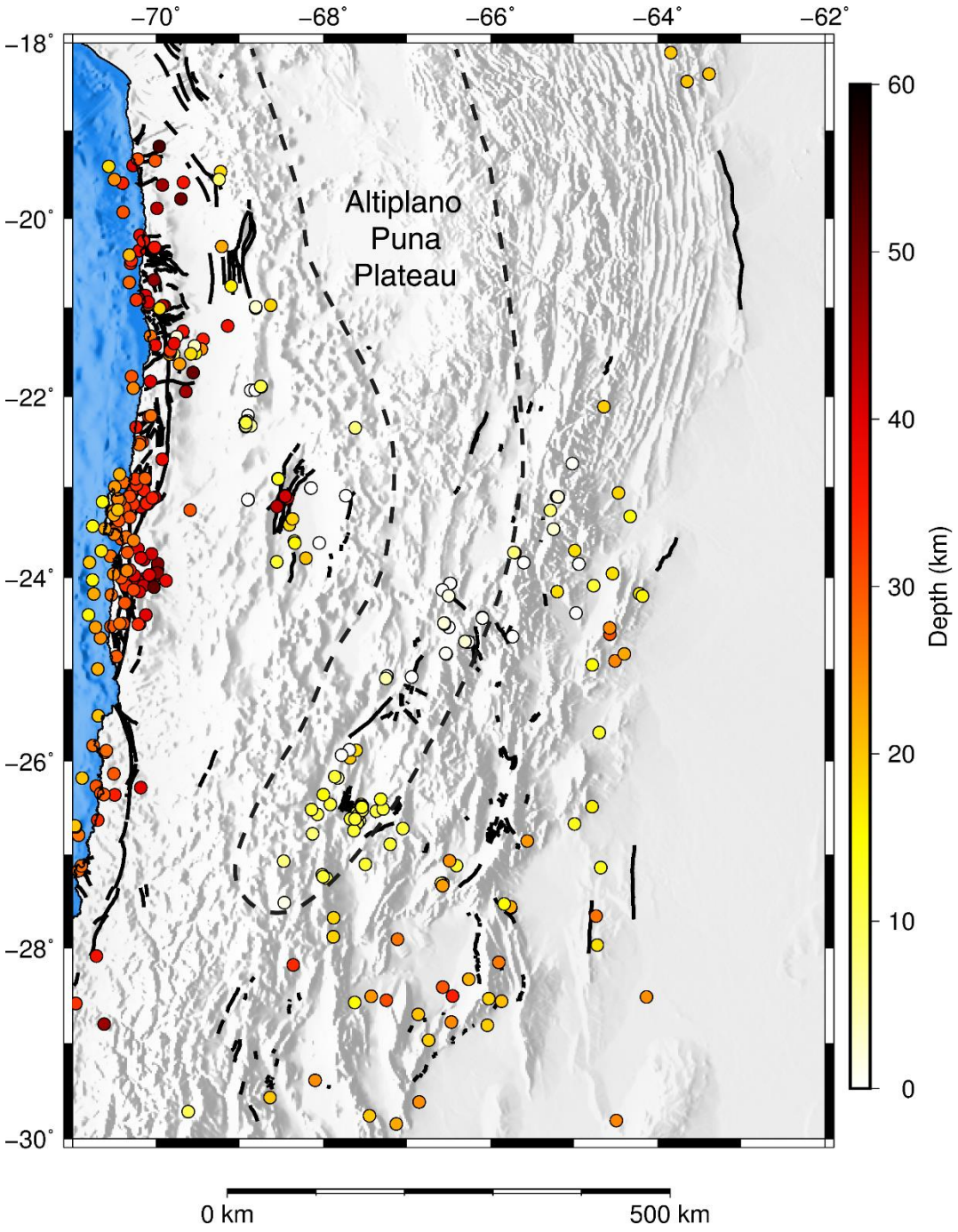

Figure 2.4: Map of the internally-drained Altiplano-Puna plateau region (dashed black line) in the Central Andes, showing the distribution of crustal hypocenters (color-coded circles – taken from the ISC-EHB Bulletin and Mulcahy et al., 2014) and neotectonic structures (solid black lines – taken from Proyecto Multinacional Andino: Geociencia para las Comunidades Andinas, 2008).

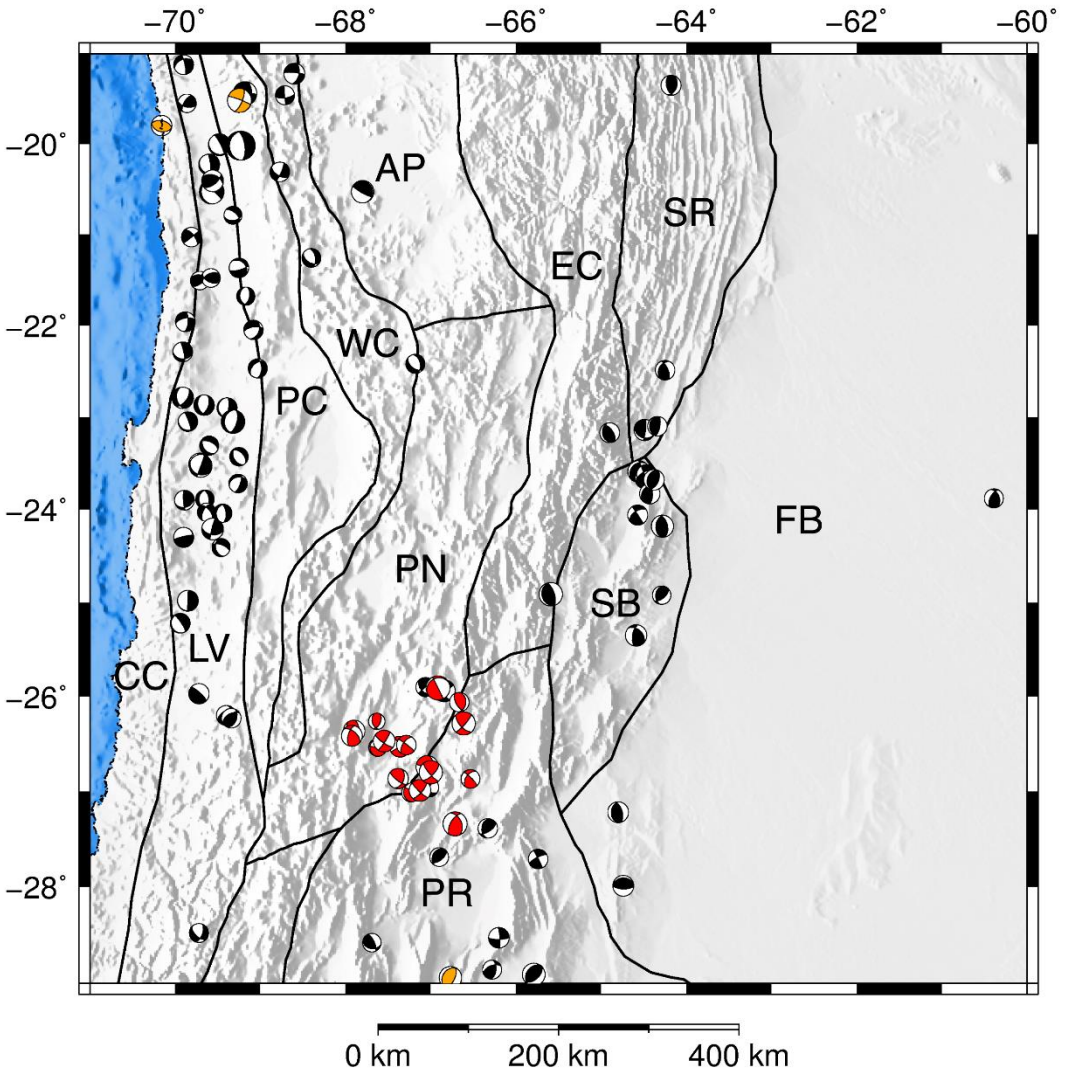

Figure 2.5: Map of the modelled region, showing the boundaries between morphotectonic units (as in Figure 2.2) and the focal mechanisms of crustal earthquakes. Focal mechanisms shown in orange, red, and black were taken from Devlin et al. (2012), Mulcahy et al. (2014), and the Glabal Centroid Moment Tensor Catalog (Dziewonski et al., 1981; Ekström et al., 2012), respectively. The sizes of the focal mechanisms correspond to the magnitude of the earthquakes, but note that the scale of the red mechanism symbols has been doubled for the sake of clarity.

Chapter 3. Three-dimensional density model of the Central Andean lithosphere

3.1. Introduction

The first step in the construction of a density model is to compile information on the near-surface and deep composition and structure of the crust and upper mantle, with the aim of reducing the ambiguity inherent to gravity modelling. Numerous geological, geochemical, and geophysical investigations have been conducted in the region providing a strong base for the model presented in this chapter. Furthermore, 2D and 3D density models covering different parts of the modelling region have been presented in previous studies.

As shown in Chapter 2, the near-surface geology of the region is divided into several morphotectonic units (Figure 2.2). The Coastal Cordillera is primarily constituted by Jurassic to Lower Cretaceous basic to andesitic volcanic and plutonic rocks that intruded a thinned continental crust (Lucassen et al., 2006; Rossel et al., 2013). To the east, the Chilean Precordillera is formed by Paleozoic igneous-metamorphic rocks, Mesozoic and Tertiary sedimentary and volcanic rocks, and it is intruded by Late Cretaceous to Paleogene plutons (Amilibia et al., 2008; Lucassen et al., 2001; Mpodozis and Ramos, 1989; Scheuber et al., 1994). The Western Cordillera constitutes the present-day volcanic arc and consists of Mesozoic sedimentary rocks and voluminous Tertiary volcanic rocks and plutons (Scheuber and Reutter, 1992).

The Andean plateau (Altiplano-Puna) is a wide intraorogenic, internally drained basin developed on Late Neoproterozoic to Paleozoic igneous and metamorphic rocks, and filled with Cretaceous and mostly Cenozoic sedimentary rocks, evaporites, and volcanics reaching thicknesses > 6 km (Alonso et al., 1991; Siks and Horton, 2011).Since the Late Miocene, local volcanic edifices and calderas have evolved within the plateau (Coira and Kay, 1993; Guzmán et al., 2014; Kay et al., 1994; Viramonte et al., 1984). The Eastern Cordillera is a thick-skinned thrust belt mainly composed of Late Neoproterozoic to Paleozoic metamorphic rocks, covered by Cretaceous and Cenozoic sediments and volcanics (Mon and Salfity, 1995).

In transition to the foreland, the Subandean Ranges are composed by Paleozoic, Mesozoic and Cenozoic sedimentary rocks (Dunn et al., 1995; Mingramm et al., 1979); the Santa Barbara System consists of Paleozoic metasedimentary rocks with overlying Cretaceous and Cenozoic sedimentary and volcanic rocks (Kley and Monaldi, 2002; Marquillas et al., 2005); and the Pampean Ranges are mainly composed by Late Proterozoic to Paleozoic metamorphic and igneous rocks (Jordan and Allmendinger, 1986; Toselli et al., 1978). In the Chaco-Paraná foreland basin, up to 7.5 km of Cenozoic sediments have been deposited over older sedimentary rocks since the Late Oligocene (Chebli et al., 1999).

With regards to the deep levels of the lithosphere, seismic refraction studies have imaged the Moho at an average depth of ~70 km beneath the plateau (~65 km in the Puna and ~75 km in the Altiplano) and ~30-35 km beneath the foreland (e.g., Beck and Zandt, 2002; Fromm et al., 2004; Heit, 2005; Heit et al., 2014, 2008, 2007; Ryan et al., 2016; Yuan et al., 2002, 2000; Figure 3.1). Moreover, based on seismic tomography, receiver functions and surface heat-flow data, some authors have identified differences in the thickness and thermal state of the lithosphere along and across strike, pointing to a thick lithosphere in the foreland and a thin lithosphere in the orogen, with a shallower lithosphere-asthenosphere boundary (LAB) beneath the Puna. (e.g., Liang et al., 2014; Springer and Förster, 1998; Whitman et al., 1996).

The seismic and electric structure of the crust has been widely investigated by magnetotelluric, seismic tomography and attenuation studies (e.g., Bianchi et al., 2013; Calixto et al., 2013; Chmielowski et al., 1999; Comeau et al., 2016, 2015; Graeber and Asch, 1999; Lessel, 1997; Schmitz and Kley, 1997; Schurr et al., 2006; Schurr and Rietbrock, 2004; Swenson et al., 2000; Ward et al., 2014, 2013; Wigger et al., 1994; Figure 3.1). Overall, the crust is characterized by high velocity and low attenuation in the forearc, low velocity and high attenuation in the orogen, and intermediate velocity in the foreland. The most prominent features are the Altiplano-Puna and Southern Puna Magma Bodies (e.g., Bianchi et al., 2013; Ward et al., 2014, 2013), and the Atacama Block (e.g., Schurr and Rietbrock, 2004), which present extremely low and high velocity, respectively. The electric structure reveals the presence of high-conductivity zones beneath the volcanic arc and the Altiplano-Puna plateau, in coincidence with the low-velocity zones, supporting the existence of partial melts in those regions (e.g., Chmielowski et al., 1999).

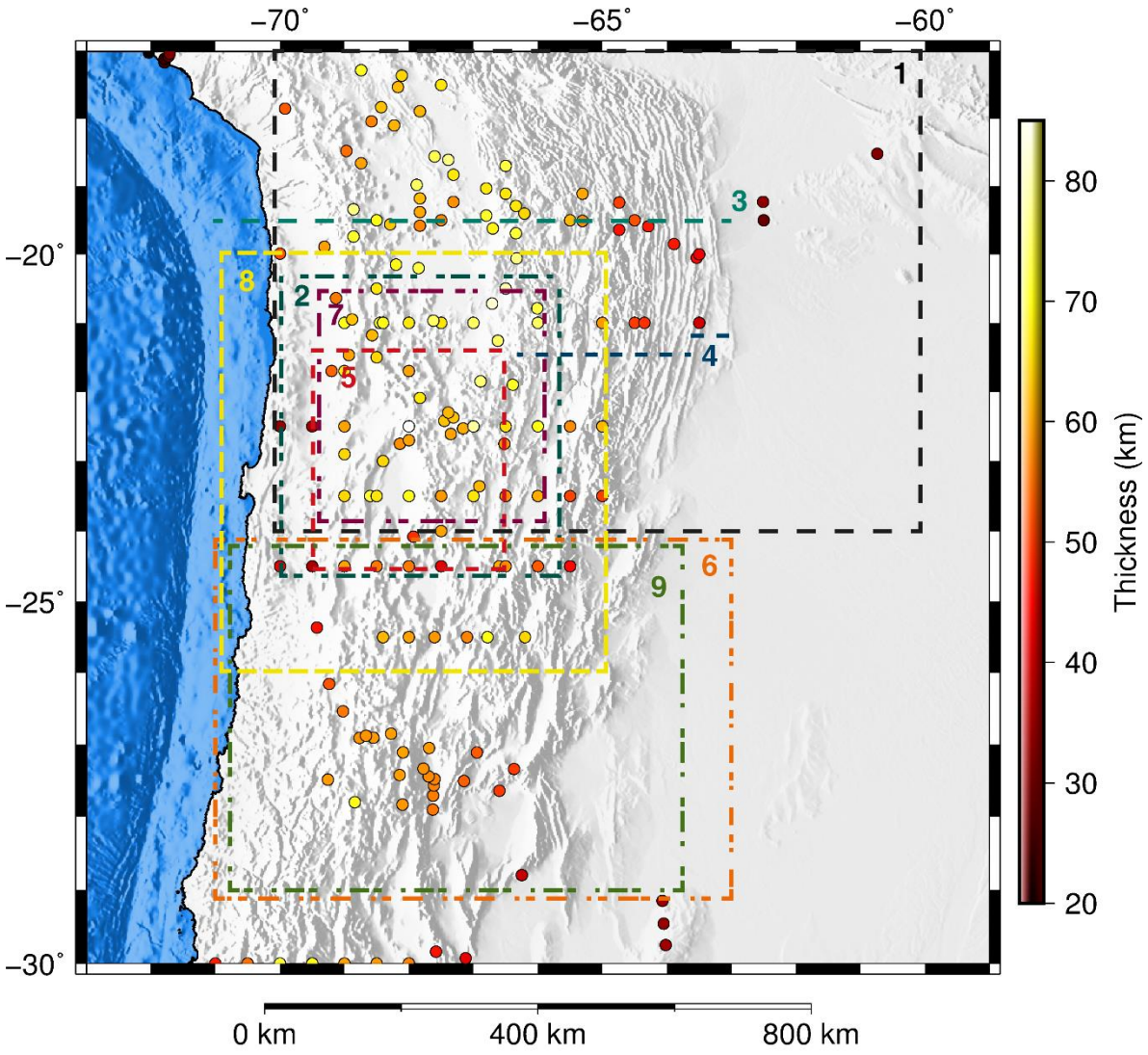

Figure 3.1: Map of the Central Andes showing crustal thickness estimates from seismic studies (color-coded dots - compilation in Assumpção et al., 2013). The colored lines and rectangles show the location of some of the seismic and magnetotelluric studies used to define the initial geometry of the model and/or analyze the results. 1 - Swenson et al. (2000); 2 - Haberland and Rietbrock (2001); 3 - Dorbath and Masson (2000); 4 - Schmitz and Kley (1997); 5 - Schurr and Rietbrock (2004); 6 - Liang et al. (2014); 7 - Ward et al. (2014); 8 - Koulakov et al. (2006); 9 - Bianchi et al. (2013).

Considering all these data and publications together with a previous model (Prezzi et al., 2009), a new and updated 3D density model of the lithosphere in the region is presented in this chapter. The modelling approach consists in the definition of units and main crustal interfaces with gravity-independent datasets (i.e. previous datasets which do not rely on gravity modelling), the determination of densities from lithology and seismic velocity, and the forward modelling of the Bouguer anomaly.

3.2. Methods and data

The key methodology of this chapter is gravity modelling. Given the non-uniqueness of the method, additional geological and geophysical constraints on the density of the units and the major interfaces (where density contrasts are larger and sharp) were incorporated in order to reduce the number of free parameters. In a first stage, an initial model was constructed on the basis of the previous investigations; then, each division in the model was assigned a density value; and finally, the initial configuration of the model was iteratively modified to fit the observed gravity anomaly.

The previous gravity model of Prezzi et al. (2009) was composed by different crustal blocks corresponding to the morphotectonic units of the Central Andes. These blocks were divided vertically into upper, middle, and lower crust, and their densities were calculated based on surface lithology and P-T conditions. Although this model was partially used as a starting model, unlike it, the density configuration presented here is mostly based on the seismic structure of the lithosphere, which provides constraints on the density distribution. Even though this new model presents fewer divisions and seems less detailed, it provides a more pragmatic representation of the crust given the recent seismic studies (e.g., Bianchi et al., 2013; Ward et al., 2013).

3.2.1. Initial model geometry

The topography and ocean bathymetry were extracted from ETOPO1 (Amante and Eakins, 2009), a 1 arc-minute global relief model. A compilation of sediment thicknesses was taken from Meeßen et al. (2018) and subtracted from the topography/bathymetry to obtain the top of the basement/crystalline crust. The interfaces dividing upper crust, middle crust, and lower crust were obtained from the previous gravity-constrained model (Prezzi et al., 2009). The bottom of the continental crust corresponds to the "Moho B2" in Assumpção et al. (2013), obtained through compilation of crustal thickness data of South America, and further interpolation using surface-wave tomography. Their preferred model "Moho B3" was not used because it includes gravity constraints (thus turning the dataset gravity-dependent). The top and bottom of the subducting oceanic crust were also obtained from the model of Prezzi et al. (2009).

The crystalline crust was differentiated into laterally juxtaposed units based on observed variations of the seismic velocity and attenuation (Vp, Vs, Qp, Qs and Vp/Vs; where Vp is P-wave velocity, Vs is S-wave velocity, Qp is attenuation of P-wave velocity, and Qs is attenuation of S-wave velocity). Taking into account published data (e.g., Bianchi et al., 2013; Calixto et al., 2013; Schurr et al., 2006; Schurr and Rietbrock, 2004; Ward et al., 2014, 2013), five different regional domains were considered (Figure 3.2).

Two regions with relatively high crustal velocity and low attenuation in the western and eastern parts of the model were delimited and named Western Domain and Eastern Domain, respectively; between them, the Central Domain presents low velocity and high attenuation (e.g., Bianchi et al., 2013; Chulick et al., 2013; Liang et al., 2014; Schurr and Rietbrock, 2004; Ward et al., 2013; Figure 3.2). The Western Domain corresponds spatially to the western part of the forearc, including the Coastal Cordillera and part of the Longitudinal Valley. The Central Domain includes the volcanic arc, the eastern part of the forearc (Chilean Precordillera and part of the Longitudinal Valley), the Altiplano-Puna plateau, the Eastern Cordillera, and part of the Subandean Ranges and Santa Barbara System. The Eastern Domain covers the foreland and parts of the Subandean Ranges, Santa Barbara System and Pampean Ranges.

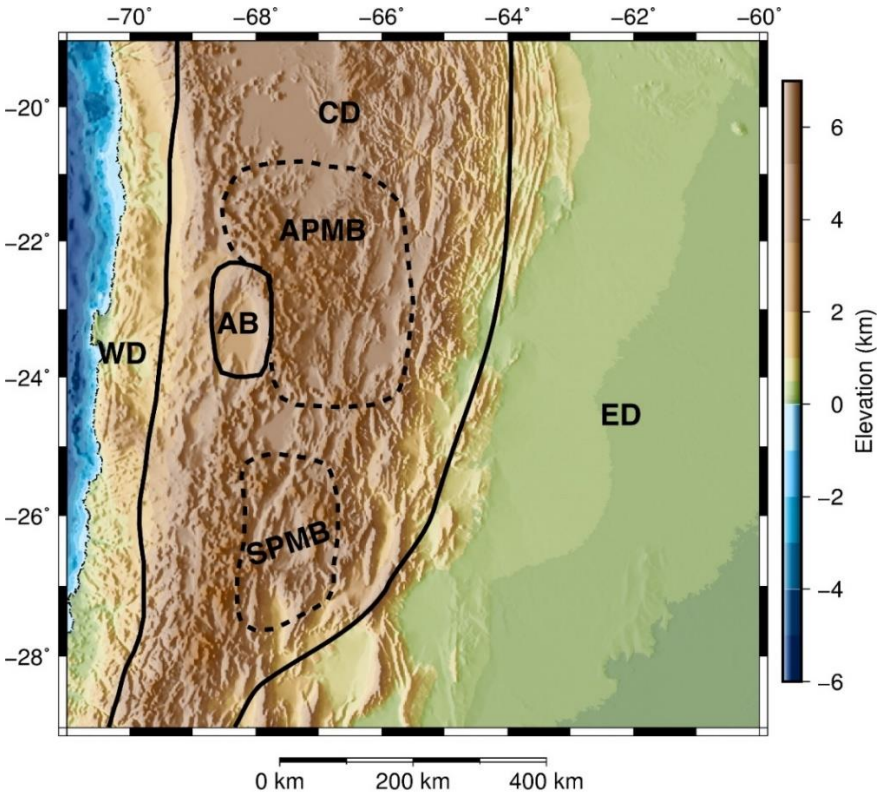

Figure 3.2: Elevation map of the modelling region displaying the boundaries of the different model domains (black lines). Dashed black lines indicate domains within the crust that do not extend throughout the entire crustal thickness. WD: Western Domain; CD: Central Domain; ED: Eastern Domain; AB: Atacama Block; APMB-SPMB: Altiplano-Puna Magma Body-Southern Puna Magma Body.

Additionally, regions with high velocity and low attenuation (e.g., Schurr and Rietbrock, 2004), and low velocity and high attenuation (Bianchi et al., 2013; Koulakov et al., 2006; Ward et al., 2014, 2013) within the Central Domain were differentiated as distinct domains; these are the Atacama Block, and the Altiplano-Puna and Southern Puna magma bodies (APMB-SPMB), respectively (Figure 3.2).

Consequently, the model consists of i) a continental crust divided into five crustal domains corresponding to the Western Domain, the Central Domain, the Eastern Domain, the Atacama Block, and the APMB-SPMB, which are vertically sub-divided into upper, middle, and lower crust; ii) a single sedimentary layer, iii) an oceanic crust, and iv) the mantle.

3.2.2. Constraints on crustal densities

The density distribution in the crust was determined from geological and geophysical constraints in addition to the densities presented in Prezzi et al. (2009). The final crustal densities implemented in the 3D gravity modelling were selected to satisfy all data sets when possible (Table 3.I).

Christensen and Mooney (1995) developed a model of the continental crust relating density to depth (pressure) along different geotherms (temperature) for 29 common rock types. Based on this model, on lithologies from outcrops and xenoliths, as well as inferred pressure-temperature conditions, the densities for the modelled units were estimated. Since metamorphic basement outcrops and xenoliths from deeper crustal levels in the Central Andes are sparse and mostly restricted to its western region, it was not possible to calculate densities for all units using this approach.

Albeit composition is poorly constrained, the seismic structure of the crust in the forearc and the orogen is well known from the extensive seismic studies in the region (e.g., Bianchi et al., 2013; Graeber and Asch, 1999; Lessel, 1997; Schmitz and Kley, 1997; Schurr and Rietbrock, 2004; Swenson et al., 2000; Ward et al., 2013; Wigger et al., 1994). Average P-wave velocities were assigned to the modelled units, and a linear relation (Christensen and Mooney, 1995) and a polynomial regression (Brocher, 2005) between density and Vp were implemented to define the density configuration of the 3D model. The linear relation is representative for crystalline rocks with Vp between 5.5 and 7.5 km/s (Eq. 3.1), while the polynomial regression is valid for all rock types (except mafic crustal and calcium-rich rocks) and a Vp range between 1.5 and 8.5 km/s (Eq. 3.2).

$$\rho(g/cm^3) = 0.541 + 0.3601V_p \quad (3.1)$$

$$\rho(g/cm^3) = 1.6612V_p - 0.4721V_p^2 + 0.0671V_p^3 - 0.0043V_p^4 + 0.000106V_p^5 \quad (3.2)$$

where ρ is the density and V_p is the P-wave velocity.

Table 3.I: Prevailing lithology, P-wave velocity and bulk density for the modelled units.

Model unit	Bulk density, $\boldsymbol{\rho}$ (kg m^{-3})	P-wave velocity, $\boldsymbol{V_p}$ (km s^{-1})	Prevailing lithology
Sediments	2450[1]	3.1-5.1	Sandstone, shale
Upper Crust Eastern Domain	2880[1]	6.1-6.4	Felsic metamorphic and igneous rocks
Lower Crust Eastern Domain	3020[3]	6.7-6.9	Felsic and mafic metamorphic and igneous rocks?
Upper Crust Central Domain	2700[1]	5.7-6.0	Ignimbrite, sandstone, schist, granite
Middle Crust Central Domain	2880[3]	6.3-6.5	Gneiss, granite, migmatite
Lower Crust Central Domain	3050[3]	6.8-7.0	Felsic granulite
Upper Crust Western Domain	2740[3]	6.1-6.4	Basalt, andesite
Middle Crust Western Domain	3040[3]	6.8-7.3	Gabbro, diorite, amphibolite
Lower Crust Western Domain	2930[3]	6.3-6.7	Serpentinized mafic rocks?
Upper Crust Atacama Block	2750[3]	6.1-6.4	Mafic rocks?
Middle Crust Atacama Block	2930[3]	6.7-7.1	Mafic rocks?
Lower Crust Atacama Block	3090[3]	7.0-7.3	Mafic rocks?
Upper Crust APMB-SPMB	2660[4]	4.5-6.0	Same as UC in the Central Domain and partial melts
Middle Crust APMB-SPMB	2830[4]	4.5-6.0	Same as MC in the Central Domain and partial melts
Oceanic Crust	2900[2]	-	Basalt, gabbro

[1]Densities calculated with Eq. 3.2 and data in Christensen and Mooney (1995); [2]densities taken from Prezzi et al. (2009); [3]densities calculated with Eq. 3.1 and data in Christensen and Mooney (1995); [4]densities calculated with Eq. 3.3.

The Western Domain is characterized by high P-wave velocity and Vp/Vs ratios typical of mafic rocks (e.g., Schurr and Rietbrock, 2004). The upper crust presents average Vp between 6.1-6.4 km/s and is composed of up to 7000-m-thick volcanic sequences with minor sedimentary intercalations and mafic intrusions; the composition is homogeneous, with prevailing basaltic andesite lava flows (e.g., Lucassen et al., 2006; Pavlenkova et al., 2009; Rossel et al., 2013; Schurr et al., 2006). The middle crust presents average Vp between 6.8-7.3 km/s and is most likely felsic in origin, but thoroughly affected by voluminous batholiths ranging in composition from gabbro to granodiorite; these areas are also affected by medium to high-temperature metamorphism (e.g., Lucassen et al., 2006; Pavlenkova et al., 2009; Rossel et al., 2013; Schurr et al., 2006). Contrary to most common characteristics of seismic structures, the lower crust presents lower P-wave velocities (6.3-6.7 km/s), furthermore, Vp/Vs ratios are characteristic of hydrated rocks (most likely serpentinites; Graeber and Asch, 1999; Schurr et al., 2006). As reported in other subduction systems, fluids ascending from the subducted slab would change the mineralogy of the lower crust and mantle in the forearc (e.g., Hyndman and Peacock, 2003; Peacock, 1996).

The Central Domain is characterized by an overall low-velocity crust; several studies have been conducted in this domain pointing to a lack of mafic lower crust based on low P-wave velocity and Vp/Vs ratios characteristic of felsic and intermediate rocks (e.g., Beck and Zandt, 2002; Swenson et al., 2000). There is a progressive regional increase of P-wave velocity from 5.7-6.0 km/s in the upper crust to 6.3-6.5 km/s in the middle crust and 6.8-7.0 km/s in the lower crust (Graeber and Asch, 1999; Wigger et al., 1994).This domain is composed of an overall felsic crust; the upper crust consists of low to medium-grade metamorphic rocks (from sedimentary and igneous protoliths), granitoids, sedimentary rocks and extensive volcanic fields (ignimbrites); the middle crust is mainly composed of medium-grade metamorphic rocks (orthogneisses, paragneisses and minor amphibolites), migmatites and granitoids (diorites, granites); and the lower crust consists of high-grade metamorphic rocks (felsic granulites, minor mafic granulites and pyroxenites) (Lucassen et al., 2001, 1999; McLeod et al., 2013; Wörner et al., 2000).

The Eastern Domain presents a simpler seismic structure; it consists of an upper crust with average P-wave velocities between 6.1-6.4 km/s and a lower crust with Vp between 6.7-6.9 km/s (Schmitz and Kley, 1997; Wigger et al., 1994). The domain is widely covered by the Andean foreland basin, with metamorphic and igneous basement rocks outcropping only in the Pampean Ranges (in the southern part of the modelling region). In the domain of the Atacama Block, P-wave velocities range between 6.2-7.5 km/s, suggesting that the crust is mafic beneath the thick sediments of the Atacama basin (Lessel, 1997; Schurr and Rietbrock, 2004).

The domain of the APMB-SPMB presents Vp between 4.5 km/s and 6.0 km/s at depths of 10-15 km and 40-45 km, respectively (Wigger et al., 1994). Due to active melting processes in this domain (see Schilling et al., 2006 for a summary) it was not suitable to use the relations between Vp and density; in turn, the densities were calculated considering the unit as a two-phase material (Eq. 3.3) formed by the same rocks as the Central Domain and a melt fraction. Based on the general felsic composition and the pressure conditions, densities of 2450 kg/cm³ and 2550 kg/cm³ were considered for the melts in the upper crust and the middle crust, respectively (Lesher and Spera, 2015). A melt fraction of 15 % was selected, which is the minimum fraction required to account for the resistivity anomalies in the region (Comeau et al., 2016).

$$\rho_b = (1 - \theta)\rho_s + \theta\rho_m \tag{3.3}$$

where ρ_b is bulk density, ρ_s is the density of the solid phase, ρ_m is the density of the melt and θ is the melt fraction.

3.2.3. Constraints on mantle density

It has been shown that compressional and shear wave velocities can be used to derive the density distribution in the mantle; given that shear waves are more sensitive to temperature variations, which have ultimately an impact on density (Goes et al., 2000), a global shear-wave tomography model was used to calculate the mantle density configuration. The tomography of Schaeffer and Lebedev (2013) was selected because of its higher resolution compared to other available models (0.5° in latitude and longitude, and 25 km in the z direction).

The method used to performed the conversion (Meeßen, 2017) is a modified version of the approach developed by Goes et al. (2000) to convert seismic velocities into temperature and densities for a given rock composition, taking into account the effects of anharmonicity and anelasticity. The information on mantle composition required to perform the calculations was taken from recorded compositions of mantle xenoliths of Cretaceous-Cenozoic age from within the region (Lucassen et al., 2005) (For a detailed description of the calculations see Appendix A). The derived densities were interpolated to a regular grid of 50 km and 10 km of horizontal and vertical resolution, respectively, covering the mantle domain of the density model, i.e. depths from the Moho down to 220 km.

3.2.4. Gravity modelling

The interactive gravity modelling software IGMAS+ (Interactive Geophysical Modelling ASsistant; Schmidt et al., 2011) was used to forward model the Bouguer anomaly. In order to compare the results of the model with the results of Prezzi et al. (2009) as a function of the new data incorporated into the model, the same Bouguer anomaly as presented in that earlier study was used in this dissertation (Figure 3.3a). For that model, the “offshore” Bouguer anomaly was calculated using the global free-air anomaly data base 2001 KMS (Andersen and Knudsen, 1998), considering the bathymetry from the model GEBCO_08 Grid (The GEBCO_08 Grid, version 20100927,

http://www.gebco.net), and assigning a density of 2670 kg/m^3 to the water. The "onshore" gravity data corresponded to measurements made and compiled by the researchers in the Collaborative Research Centre SBF 267 "Deformation Processes in the Andes" (for which a detailed explanation can be found in Götze et al., 1990). In order to warrant comparability between the calculated gravity anomaly of the model (Figure 3.3b) and the observed Bouguer anomaly (Figure 3.3a), the model was cropped to sea level in the onshore domain.

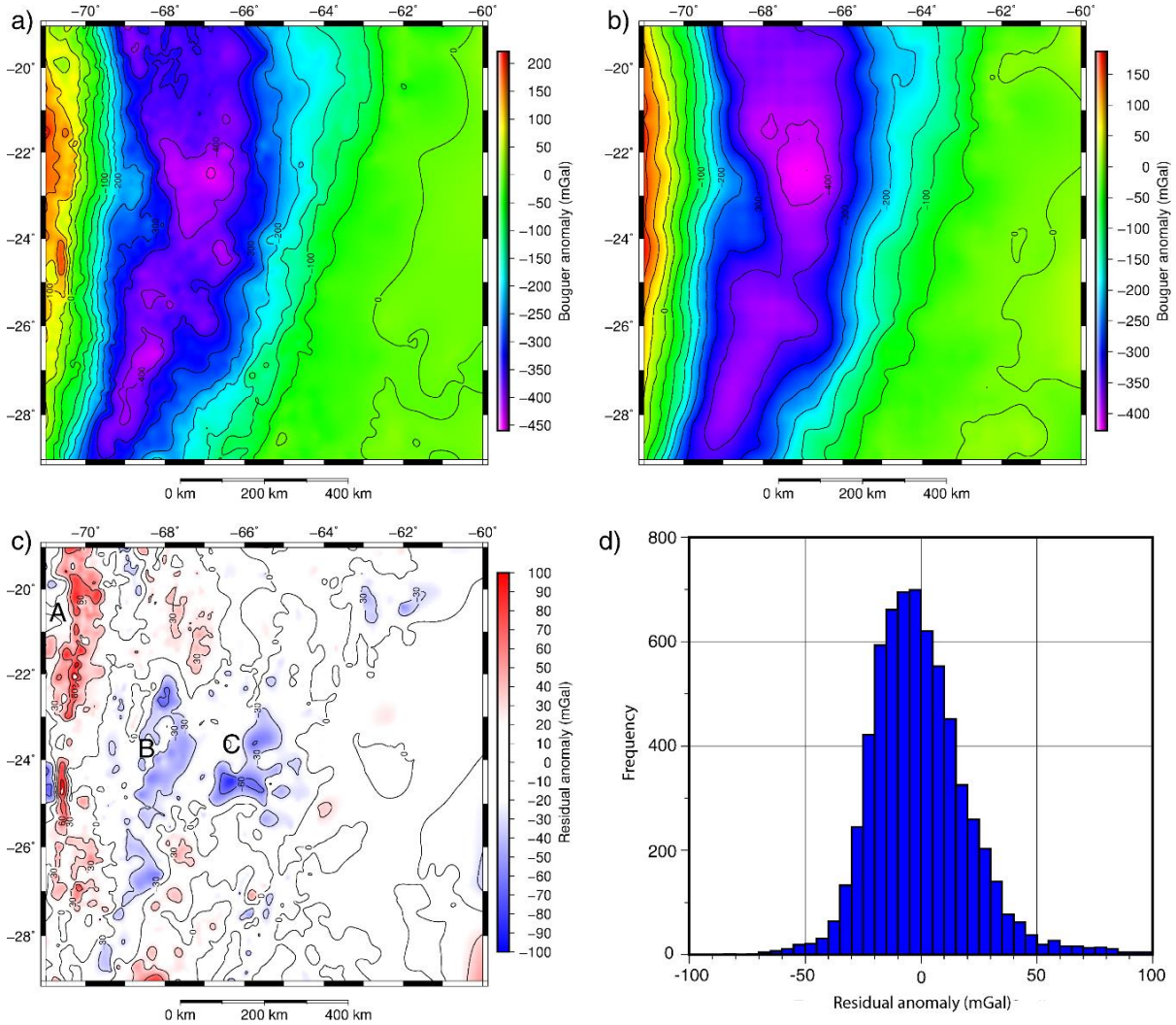

Figure 3.3: Observed (a) and calculated (b) Bouguer anomaly of the modelled region; (c) residual anomaly. A, B, and C indicate anomalies referred to in the text; (d) histogram of the residual anomaly.

The initial 3D density model was set up in IGMAS+ by introducing the interfaces dividing the different model units, which were previously interpolated and extrapolated into regular grids with a horizontal resolution of 50 km x 50 km. The resulting structure was vertically layered within the different domains, in a way that each layer represented a discrete density unit for the gravity modelling. Each crustal layer was then assigned its corresponding constant density (Table 3.I). In the mantle, from the Moho to the base of the model (at 220 km), the interpolated regular grid of densities derived from the shear-wave tomography model was implemented as a voxel cube (50 km horizontal resolution and 10 km vertical resolution).

After setting up the model and assigning densities, the Bouguer anomaly of the density model was calculated. Since the main density heterogeneities strike in N-S direction, E-W striking 2D working planes were generated to forward model the gravity anomaly. Given that the model extends over 1100 km in the N-S direction, and the horizontal resolution is 50 km, 23 vertical sections were created. To reduce uncertainty and ambiguity inherent to the methodology, most parameters were kept constant during the forward-modelling procedure. Calculated densities as well as interfaces taken from gravity-independent datasets (i.e. Moho and basement top) were not changed. The upper limit of the lower crust was used as free parameter because it is the only surface not constrained by gravity-independent data covering the entire modelling region.

On the basis of the greater differences between calculated and observed Bouguer anomalies, the original X-Y-Z grids corresponding to the upper limit of the lower crust were modified to reduce misfits. The new set of grids were uploaded in the software, and the gravity anomaly was calculated and compared to the Bouguer anomaly again. The process was repeated iteratively to fit the gravity anomaly.

3.3. Results

The final 3D density structure as obtained from integrated forward gravity modelling reproduces the gravity anomalies fairly well (Figure 3.3). Less than 10% of the modelled region shows absolute residual anomalies greater than 30 mGal (Figure 3.3, c & d). These anomalies are of short wavelength and do not generally present a systematic arrangement. Considering that the mode of the residual anomaly is -4.57 mGal (Figure 3.3d), with a standard deviation of 21.52 mGal, and the short wavelength of the residual anomalies, it can be concluded that the model reproduces the long wavelength (regional, large-scale) density configuration of the Central Andes.

The modelled thickness of the upper-middle crust (Figure 3.4a) is uniform in the Eastern Domain (~22 km) and increases to the west. Within the Central Domain, the upper-middle crust presents maximum thicknesses beneath the Western Cordillera and the northern Puna (~45 km). To the south and north, beneath the southern Puna and the Altiplano, the thickness decreases, reaching a minimum of ~36 km in the Altiplano. In the Western Domain, the thickness decreases progressively towards the trench in the west.

The modelled lower crust (Figure 3.4b) is thin in the Eastern Domain (~5-15 km). Its thickness increases to the west, in some parts of the Central Domain, reaching ~20-30 km beneath the Puna and ~35-40 km beneath the Altiplano. The Puna exhibits an irregular pattern, with semi-circular areas characterized by different thicknesses; particularly between 24-25°S and 66-68°W, there is a region with reduced thickness (~15 km). In the Western Domain the lower crust is thin as in the Eastern Domain, but it is more irregular and presents a broader range.

The major differences compared to the model of Prezzi et al. (2009) are located in the orogen, particularly in the Altiplano. The results of this model show a 5 to 10 km thicker upper-middle crust in the Puna, and a 15 to 18 km thicker lower crust in the Altiplano. Although the thickness distribution in the foreland and forearc differs from that of Prezzi et al. (2009), the range in both models is the same. The observed differences are primarily due to the different data used for the definition of the Moho and the different densities considered in the mantle.

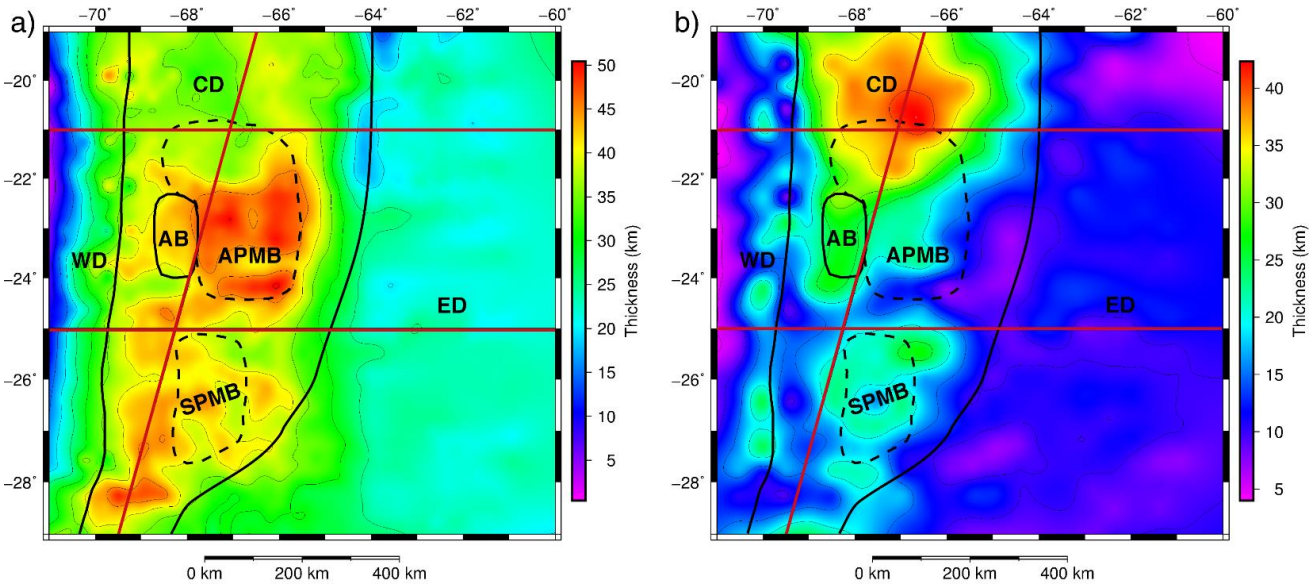

Figure 3.4:. Thickness distribution of (a) upper and middle crust; (b) lower crust. Solid and dashed black lines represent boundaries between crustal domains used in this study (WD: Western Domain; CD: Central Domain; ED: Eastern Domain; AB: Atacama Block; APMB-SPMB: Altiplano-Puna Magma Body-Southern Puna Magma Body). Solid red lines show the location of cross-sections presented in Figure 3.5.

Figure 3.5 shows two cross-sections perpendicular to the orogen across the model at 21°S (Altiplano; Figure 3.5a) and 25°S (Puna; Figure 3.5b), and a NNE-SSW striking cross-section through the orogen from 67°W in the north to 69°W in the south (Figure 3.5c). The cross-sections show the distribution in depth of the domains through the model. Comparing the cross-sections in the north and south (Figure 3.5, a & b), it is possible to observe the same crustal-thickness trends that in the thickness maps (Figure 3.4). The sediment thickness in the foreland and the thickness of the lower crust in the orogen are greater to the north, in the Subandean Ranges and the Altiplano, respectively. Additionally, the cross-sections provide a better insight on the position of the low-velocity anomalies (APMB and SPMB) within the crust. Figure 3.5c clearly shows the increasing depth of the Moho from south to north, the thicker lower crust beneath the Altiplano plateau, and the thicker upper-middle crust beneath the Puna plateau.

Given the complex structure of the model (horizontal and vertical sub-divisions) and the lack of constraints on the intra-crustal interfaces, the average density for the total crystalline crust (from basement top to the Moho) for each X-Y position is presented in Figure 3.6. The average density provides a more direct and independent insight into the system and allows conclusions to be drawn regarding the general composition of the crust. Three main sectors can be recognized in the map; a low-density region in the center bounded by two high-density zones to the west and east (partially consistent with the model domains). The low-density zone presents an average density of 2860 kg/m^3 and spatially coincides with the Central Domain. It is narrow in the southwest and widens to the north, where density is higher and a less pronounced transition to the high densities in the west and east occurs. The western part of the model presents the highest average densities (around 2945 kg/m^3), corresponding to the Western Domain and the Atacama Block. To the east, within the Eastern Domain, the average crustal density is high as well, but smaller than the one in the Western Domain (2915 kg/m^3).

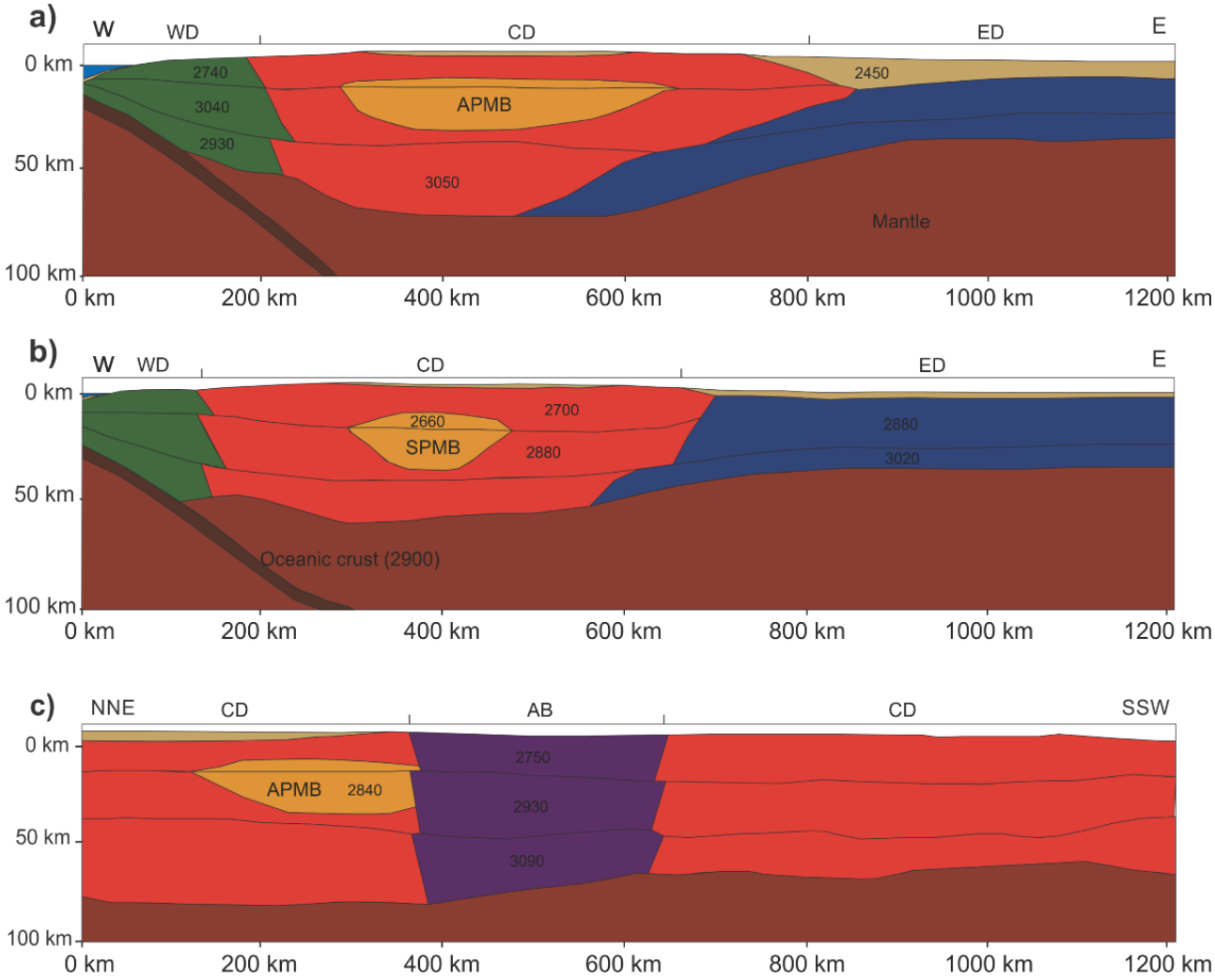

Figure 3.5:. Cross-sections through the density model, locations are depicted in Figure 3.4. WD: Western Domain; CD: Central Domain; ED: Eastern Domain; AB: Atacama Block; APMB: Altiplano-Puna Magma Body; SPMB: Southern Puna Magma Body. Densities are in kg/m3. (a) Structure perpendicular to the orogen along the Altiplano transect (21°S); (b) structure perpendicular to the orogen along the Puna transect (25°S); (c) structure parallel to the orogen.

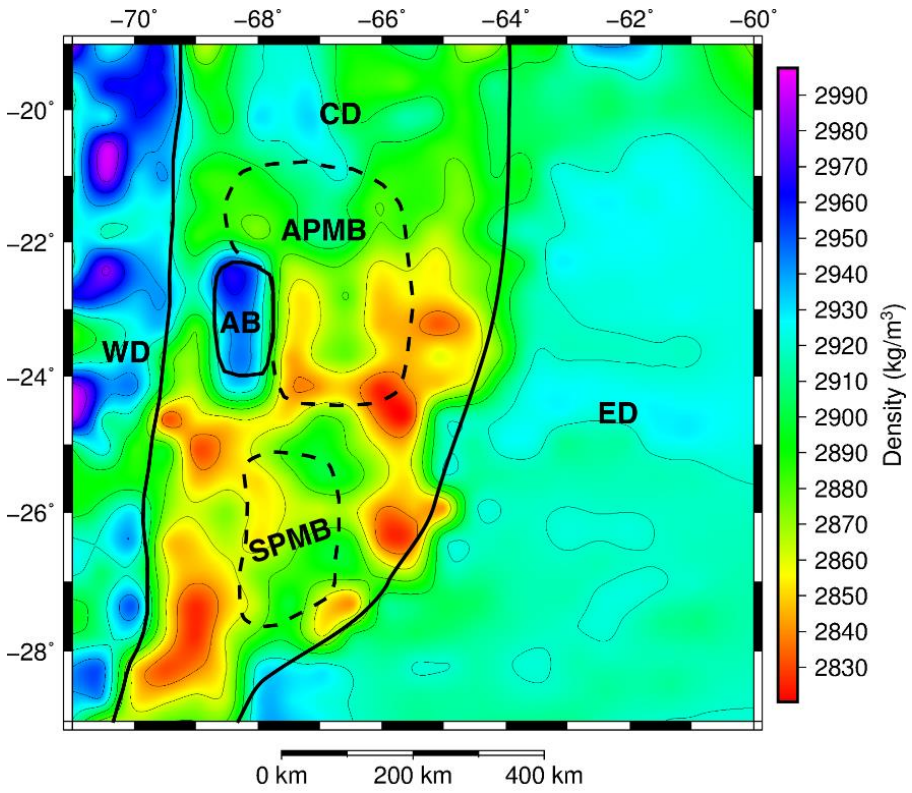

Figure 3.6:. Average density of the continental crystalline crust (no sediments included). Solid and dashed black lines are boundaries between crustal domains used in this study (WD: Western Domain; CD: Central Domain; ED: Eastern Domain; AB: Atacama Block; APMB-SPMB: Altiplano-Puna Magma Body-Southern Puna Magma Body).

The density distribution in the mantle shows similar trends at different depth levels (Figure 3.7). There is a high-density region striking in N-S direction in the western part of the model, with decreasing densities to the west and east. At 100 km depth (Figure 3.7a) the high-density region is close to the western boundary of the model and widens from north to south, presenting densities of 3322-3324 kg/m^3. At larger depths, the high-density region is displaced to the east and loses continuity to the south, presenting densities of 3372-3380 kg/m^3 at 150 km depth, and 3408-3416 kg/m^3 at 200 km depth (Figure 3.7, b & c).

The observed density distribution is consistent with the subduction geometry of the Nazca plate beneath the South American plate; the depth slices cut through different positions of the cold subducting slab, which is characterized by higher densities than the surrounding mantle. The southward widening of the slab-related high-density anomaly at 100 km depth agrees well with the development of a flat-slab geometry south of 27°S, as reported by previous studies (e.g., Barazangi and Isacks, 1976; Ramos et al., 2002).

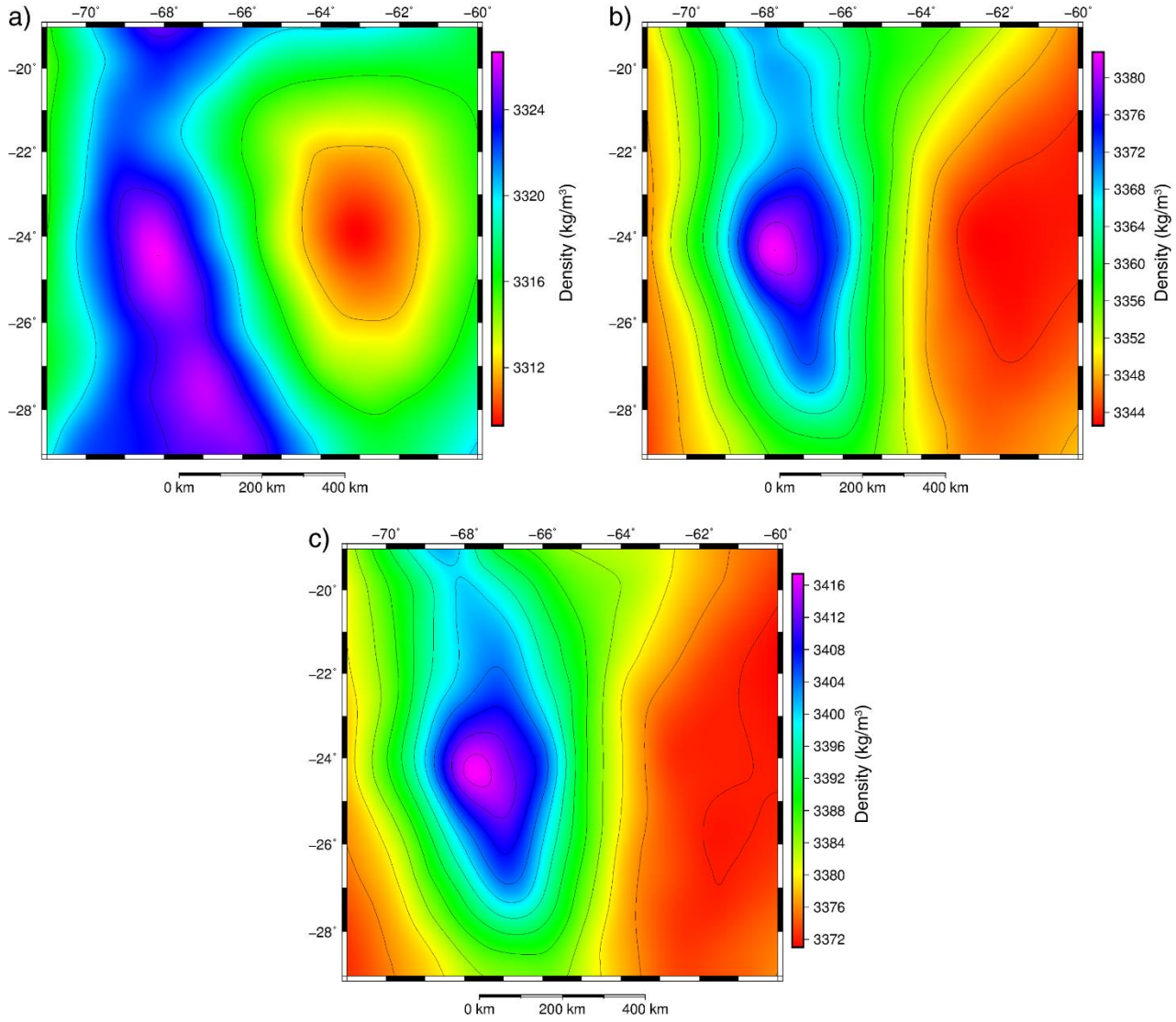

Figure 3.7: Density distribution in the mantle derived from the shear-wave tomographic model at (a) 100 km depth; (b) 150 km depth; (c) 200 km depth.

3.4. Discussion

The observed Bouguer anomaly was successfully reproduced assuming a felsic composition for the model units in the orogen (Figure 3.3c). Consequently, this model supports observations pointing to the absence of volumetrically important underplated dense mafic lower crust (e.g., Beck and Zandt, 2002; Lucassen et al., 2001).

Little is known about crustal composition in the foreland. Xenoliths found in the Salta rift basalts and basement outcrops in the Pampean Ranges provide the only lithological information, indicating that felsic metamorphic and igneous rocks prevail, with only a small proportion of mafic rocks (Lucassen et al., 2005, 1999). The overall seismic structure of the crust shows, however, that velocities are faster in the foreland than in the orogen, suggesting that the foreland crust is more mafic than the orogenic crust (Schmitz and Kley, 1997; Wigger et al., 1994). Likewise, the results of the density model show that the average density of the crystalline crust (Figure 3.6) beneath the orogen is low (2860 kg/m^3) when compared to that in the foreland (2915 kg/m^3). These results suggest as well that there should be a compositional difference between both regions, with more mafic rocks in the foreland, given that the crust in that region is significantly thinner than in the orogen and high-density rocks associated with high pressures are not expected.

Considering that most outcrops in the Central Andes consist of rocks younger than 600 m.y. and that Nd model ages present a peak at 1.8-2.0 Ga with a shoulder towards 1.3 Ga, consistent with the age of old basement remnants, Lucassen and Franz (2005) suggested that this part of the Central Andes evolved as a mobile belt, in which most of the crust formed in the Paleoproterozoic and was later recycled through a number of orogenic events since the early Paleozoic. The recycling of the crust involves shortening through stacking of upper crust, metamorphism, large-scale melting, differentiation and homogenization of the crust, and potential removal of dense roots through delamination (DeCelles et al., 2009; Lucassen and Franz, 2005). Moreover, Hacker et al. (2011) introduced the term relamination to refer to the re-incorporation of relatively evolved crustal material to the crust via subduction-related processes such as sediment

subduction, arc subduction and subduction erosion. Several authors have proposed that some of these processes involved in crustal recycling took place during the Phanerozoic evolution of the Central Andes (e.g., Escayola et al., 2011; Lucassen and Franz, 2005; Maloney et al., 2013; Ramos, 2008; von Hillebrandt et al., 2000; Wörner et al., 2000). Following these considerations, it is possible that the crust in the orogen and foreland was originally relatively uniform, and that subduction-related processes since the early Paleozoic (potentially through relamination, extensive magmatic activity, crustal thickening and delamination), differentiated the magmatic and/or orogenic region from the rest of the crust. Through these processes, the orogenic crust became more felsic and thus less dense than the foreland.

In the orogen interior, the Altiplano displays higher average crustal densities than those in the Puna (2885 kg/m^3 and 2850 kg/m^3 respectively; Figure 3.6) and a thicker lower crust (Figure 3.4b). Although the crust is thicker in the Altiplano, large differences in rock density due to mineral and rock packing are not expected, suggesting a compositional difference between the two regions. Previous investigations have proposed foreland crust underthrusting beneath the Altiplano and lower crustal flow as mechanisms for plateau formation (e.g., DeCelles et al., 2015; Eichelberger et al., 2015; Isacks, 1988; McQuarrie et al., 2005). The occurrence of such processes over the last million years would have produced an increase in the thickness of the lower crust as well as in the average density of the crust beneath the Altiplano compared to the rest of the plateau, possibly explaining the observed heterogeneities.

Furthermore, joint interpretations of geological, geophysical and geochemical studies of the Andean plateau have suggested delamination as an important process in the Neogene evolution of the region (e.g., Kay et al., 1994). The style of delamination processes could play an important role on the observed crustal configuration along the plateau; partial piecemeal delamination of the crust in the Altiplano (Beck and Zandt, 2002) against recent delamination of large blocks beneath the Puna (Beck et al., 2015; Calixto et al., 2013) could contribute to the modelled thicker lower crust (Figure 3.4b) and higher crustal densities (Figure 3.6) in the Altiplano when compared to the Puna.

The negative anomalies B and C within the plateau in the residual anomaly map (Figure 3.3c) indicate that there is an excess of mass in the model. Taking into consideration the location of the anomalies with respect to the volcanic arc and the Altiplano-Puna and Southern Puna magma bodies, it is likely that these discrepancies are related to the presence of melts in the crust. In this line, anomaly B would result from the presence of magma chambers in the volcanic arc that are not included in the density model because they are beyond the scale and scope of this dissertation. Anomaly C would most likely be associated with the modelled regions undergoing partial melting within the crust (APMB and SPMB), which probably extend irregularly further east than indicated by velocity anomalies.

In the Western Domain, the results indicate that the crust beneath the Coastal Cordillera is characterized by high densities (Figure 3.6), which are consistent with the extensive formation of juvenile mafic crust during the Jurassic under an extensional subduction cycle (Lucassen et al., 2002; Rossel et al., 2013). The eastward extension of the high densities beneath some parts of the Longitudinal Valley suggests that mafic rocks cropping out in the Coastal Cordillera could be present in the subsurface further east, indicating a broader region for the Jurassic extension. The positive residual anomaly A in this domain (Figure 3.3c) represents a deficit of mass that could be related to the presence of relatively shallow mafic intrusions not resolved in the density model.

Beneath the Atacama basin, densities are similar to those in the Western Domain (Figure 3.6), however, there are only few outcrops providing information on the nature of the crust in the region. Based on the geology of the surroundings, as well as investigations on the gravity field and seismic velocity anomalies (Götze and Krause, 2002; Schurr and Rietbrock, 2004), it has been proposed that the region underwent different magmatic and extensional pulses through time, such as the Salta Rift, that added mafic material to the crust (Reutter et al., 2006). The presence of mafic rocks within the crust would explain gravity and velocity anomalies as well as the modelled high density in the region.

With respects to the history of accretion and the distribution of terranes, there is not a clear correlation between the average density of the crust (Figure 3.6) and the position of terrane boundaries proposed for the region (Figure 2.3). If these boundaries were indeed present, it is likely that the composition of the individual terranes was similar or became uniform after crustal recycling. In this regard, the MARA craton, as proposed in Casquet et al. (2012), would be more consistent with the results of the model. Nonetheless, a more detailed analysis is required to come to a robust final conclusion; including for example, a higher resolution model and the additional constraint of gravity gradients, which could help to identify such boundaries if present.

3.5. Summary and conclusions

A new model of the density distribution in the Central Andean lithosphere and the adjacent foreland was constructed by integrating data from previous models and new studies. The density configuration of the crust was derived from lithology constraints and/or P-wave velocities, while the densities of the mantle were converted from a shear-wave tomographic model. The model was refined and validated through forward modelling of the Bouguer anomaly. The main outcomes are:

1. the average density of the crystalline crust is significantly lower in the orogen (2850-2860 kg/m^3) than in the foreland (2915 kg/m^3), forearc (2945 kg/m^3) and Atacama Block (2945 kg/m^3). The density distribution reflects compositional heterogeneities within the crust most likely caused by different tectonic histories;
2. the high densities in the forearc and the Atacama Block are consistent with the presence of mafic magmatic rocks in the crust associated with extensional events. The regional character of the high-density zones suggests that crustal extension and mafic magmatic activity involved a wider region than indicated by surface outcrops;

3. the significantly low density of the thick orogenic crust could be the result of crustal differentiation due to a long-lived history of shortening events, accompanied by delamination and relamination processes;
4. within the Andean plateau, the average crustal density and thickness of the lower crust are higher in the Altiplano than in the Puna, suggesting a more mafic composition of the former. The partial piecemeal delamination of the lower crust in the Altiplano compared to the delamination of large blocks in the Puna, and the underthrusting of the foreland lower crust beneath the Altiplano could be at the origin of the observed differences;
5. there is no spatial correlation between the models of terrane configuration and the density of the crust, suggesting that any existing heterogeneities were overprinted by crustal recycling during the subsequent tectonic events.

Chapter 4. Thermal state of the Central Andean lithosphere

4.1. Introduction

As presented in Chapter 3, a large number of previous investigations have revealed important across-strike heterogeneities within the lithosphere, consistent with the results of the density model (e.g., Lucassen et al., 2001; Meeßen et al., 2018; Prezzi et al., 2009). Most of the forearc is characterized by a relatively thin mafic crust that thickens towards the east, presenting high density, high seismic velocity, and low attenuation (e.g., Assumpção et al., 2013; Rossel et al., 2013; Schurr and Rietbrock, 2004). In contrast, the adjacent volcanic arc (Western Cordillera) and the orogenic backarc are characterized by a thick felsic crust with low density, low seismic velocity, and a thin lithospheric mantle (e.g., Beck and Zandt, 2002; Koulakov et al., 2006; Yuan et al., 2002). Further east, the foreland is characterized by a thinner crust with a felsic upper layer, a possibly mafic lower crust, and slightly higher seismic velocity than within the orogen (e.g., Feng et al., 2007; Rosa et al., 2016).

The surface heat-flow distribution (Figure 4.1) correlates fairly well with the aforementioned heterogeneities, with low to intermediate heat-flow in the forearc (20-30 mW m-2) and foreland (50-70 mW m-2) areas, and increased heat-flow values within the orogen (over 100 mW m-2) (Hamza and Muñoz, 1996; Henry and Pollack, 1988; Springer and Förster, 1998), indicating east-west variations in the thermal field (e.g., Springer, 1999). Previous investigations have also identified along strike differences in the surface heat-flow and the depth of the lithosphere-asthenosphere boundary (LAB) beneath the Altiplano-Puna plateau, reflecting potential variations in the thermal state of the lithosphere, with the Puna having an increased thermal gradient (e.g., Liang et al., 2014; Prezzi et al., 2014; Springer and Förster, 1998; Whitman et al., 1996).

The existence of thermal anomalies in the crust and mantle beneath the plateau has been established by a wide variety of independent geological, geochemical and geophysical investigations (e.g., Bianchi et al., 2013; Koulakov et al., 2006; Schurr et al., 2003; Whitman et al., 1996). The region is characterized by the presence of large ignimbritic deposits with major crustal magmatic contribution, and isolated, volumetrically

small, mantle-derived basaltic rocks that have erupted since Oligo-Miocene times (e.g., Guzmán et al., 2014; Kay et al., 1994; Risse et al., 2013; Figure 4.1). Based on the widespread distribution of such deposits, several authors have proposed that an ignimbrite "flare-up" occurred during the Miocene (e.g., Coira and Kay, 1993; Viramonte et al., 1984).

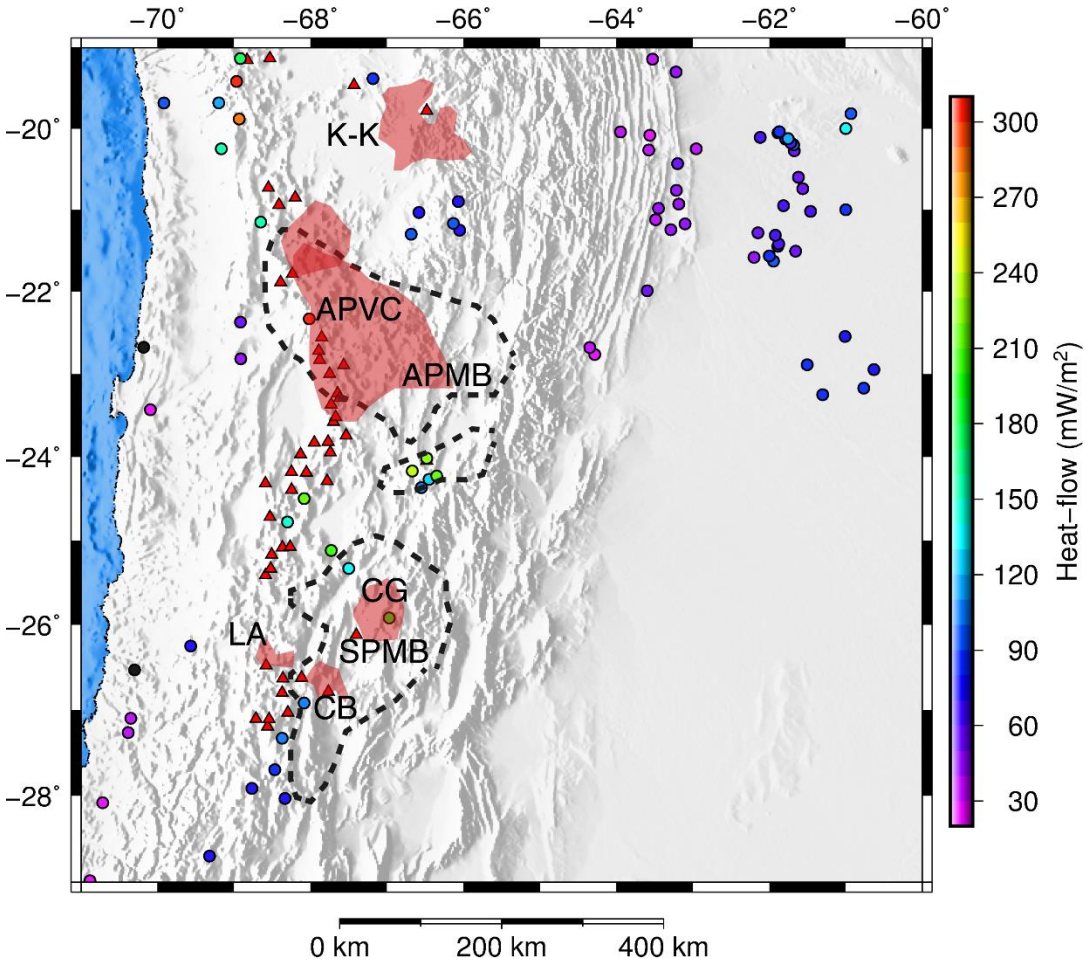

Figure 4.1: Distribution of measured surface heat-flow data (color-coded dots), active volcanoes (red triangles – from the Global-Volcanism-Program, 2013), large calderas and volcanic provinces (red patches – compiled from Burns et al., 2015; Guzmán et al., 2014; Kay et al., 2010), and regions with anomalous low crustal velocity and resistivity throughout the modelling region (dashed black lines – compiled from Beck et al., 2015; Bianchi et al., 2013). K-K: Kari-Kari Los Frailes; CG: Cerro Galan; CB: Cerro Blanco; LA: Laguna Amarga; APVC: Altiplano-Puna Volcanic Complex; APMB: Altiplano-Puna Magma Body; SPMB: Southern Puna Magma Body.

The largest concentration of ignimbrites is located between 21°S and 24°S; in the region known as the Altiplano-Puna Volcanic Complex (APVC; de Silva, 1989), extending approximately over 60000 km^2 with an estimated volume of >15000 km^3 (Figure 4.1; Burns et al., 2015; Guzmán et al., 2014). The largest center north of 21°S is the Kari-Kari-Los Frailes ignimbrite complex; south of 24°S, Cerro Galán, Laguna Amarga and Cerro Blanco complexes represent the largest outcropping ignimbrites (Figure 4.1; Kay et al., 2010). The location of most of these large deposits spatially coincides with regions of the subsurface characterized by abnormally low seismic velocity, high seismic attenuation, and high electric conductivity (e.g., Bianchi et al., 2013; Chmielowski et al., 1999; Wölbern et al., 2009; Yuan et al., 2000; Figure 4.1).

Two main geophysical anomalies have been identified within the crust, which are commonly referred to in the literature as low velocity zones (LVZ) or high conductivity zones (HCZ). These anomalies correspond to the already mentioned Altiplano-Puna Magma Body (APMB) and Southern Puna Magma Body (SPMB) (Bianchi et al., 2013; Chmielowski et al., 1999). The APMB, which lies between 15 and 40 km beneath the plateau area and between 20°S and 23°S, was the first to be defined; it is characterized by low resistivity, low seismic velocity, a high Vp/Vs ratio, and high attenuation. This anomaly is interpreted to represent a region that is undergoing metamorphism and partial melting (e.g., Beck and Zandt, 2002; Comeau et al., 2016, 2015; Díaz et al., 2012; Zandt et al., 2003). The full extent and 3D geometry of the anomaly was determined by means of joint inversion of surface waves and receiver functions (Ward et al., 2014, 2013; Figure 4.1). The SPMB has recently been defined by Bianchi et al. (2013), who detected a low velocity zone in the southern Puna crust between 26°S and 27.5°S (using P-wave tomography), which they suggested could be due to another mid-crustal region with active partial melting.

Interestingly, surface heat-flow throughout the plateau area is anomalous, with documented measurements of up to 320 mW m^{-2} in the volcanic arc and the Puna (e.g., Hamza and Muñoz, 1996; Henry and Pollack, 1988; Springer and Förster, 1998; Figure 4.1). Even though reliable data are sparse and scattered, it is still clear that surface heat-flow in

the plateau is higher than in the surroundings. It has been shown that heat conduction alone is not sufficient to account for these observations unless extreme surface heat-flow values are neglected (> 120 mW/m^2). Otherwise, additional convective and/or advective processes need to be considered (Chapman, 1986; Furlong and Chapman, 2013).

Although the extent of the thermal anomalies has been largely constrained, there are only few estimates on the temperature distribution with depth. Kay et al. (2010) determined the pre-eruptive conditions for some of the younger ignimbritic deposits in the Puna plateau (less than 2.5 m.y. old), obtaining temperatures between 770-840°C at 4-8 km depths. Burns et al. (2015) obtained similar temperatures (790-890°C) at the same depth range (4-8 km) for the young Purico-Chascón volcanic complex (~1 Ma) within the APVC. In the same volcanic complex, Schmitt et al. (2001) determined pre-eruptive temperatures of up to 965°C at ~17-20 km. On the basis of numerical models, Babeyko et al. (2002) suggested that temperatures of at least 700-800°C in the middle crust are required to account for magma production.

The determination of the temperature distribution beneath the surface is important because temperature plays a key role in several lithospheric processes such as isostasy, deformation and resource generation. Therefore, the impact of the Central Andean lithospheric structure on its thermal field is addressed in this chapter. In that respect, a three-dimensional lithology-derived model of the present-day steady-state conductive thermal field is presented. The model builds upon the 3D data-driven density model of the region, after parametrization of thermal properties on the basis of published average values for representative lithologies. In addition, the model is complemented with the determination of the depth to the bottom of the magnetic layer (interpreted as the Curie isotherm) in the Altiplano-Puna plateau from the spectral analysis of the magnetic anomaly.

4.2. Methods and data

4.2.1. Modelling of the steady-state conductive thermal field

The temperature distribution in the Central Andean lithosphere was derived through the calculation of the conductive thermal field for steady-state conditions, based on the assumption that conduction is the dominant mechanism for heat transport in the lithosphere. The conductive heat equation, also known as Fourier's law, for steady-state conditions is as follows:

$$\nabla \cdot (\lambda_b \nabla T) = -S \quad (4.1)$$

where ∇ is the Nabla operator, S is the radiogenic heat production, T is the absolute temperature, and λ_b is the bulk thermal conductivity.

Calculations were performed on the basis of the 3D data-derived density model (Figure 4.2), in order to account for the lateral and vertical variations in radiogenic heat production and thermal conductivity of the crust, which have not been included before in previous estimates of the thermal field for the region.

To solve the equation in 3D for a thermally equilibrated system the MOOSE-based application GOLEM was used (Jacquey and Cacace, 2017). GOLEM is a numerical simulator for modelling coupled thermo-hydro-mechanical processes (for further information on the mathematical and computational aspects see Cacace and Jacquey, 2017). The simulation requires the assignment of thermal properties (thermal conductivity and radiogenic heat production) to every division or unit in the density model, as well as the definition of upper and lower thermal boundary conditions.

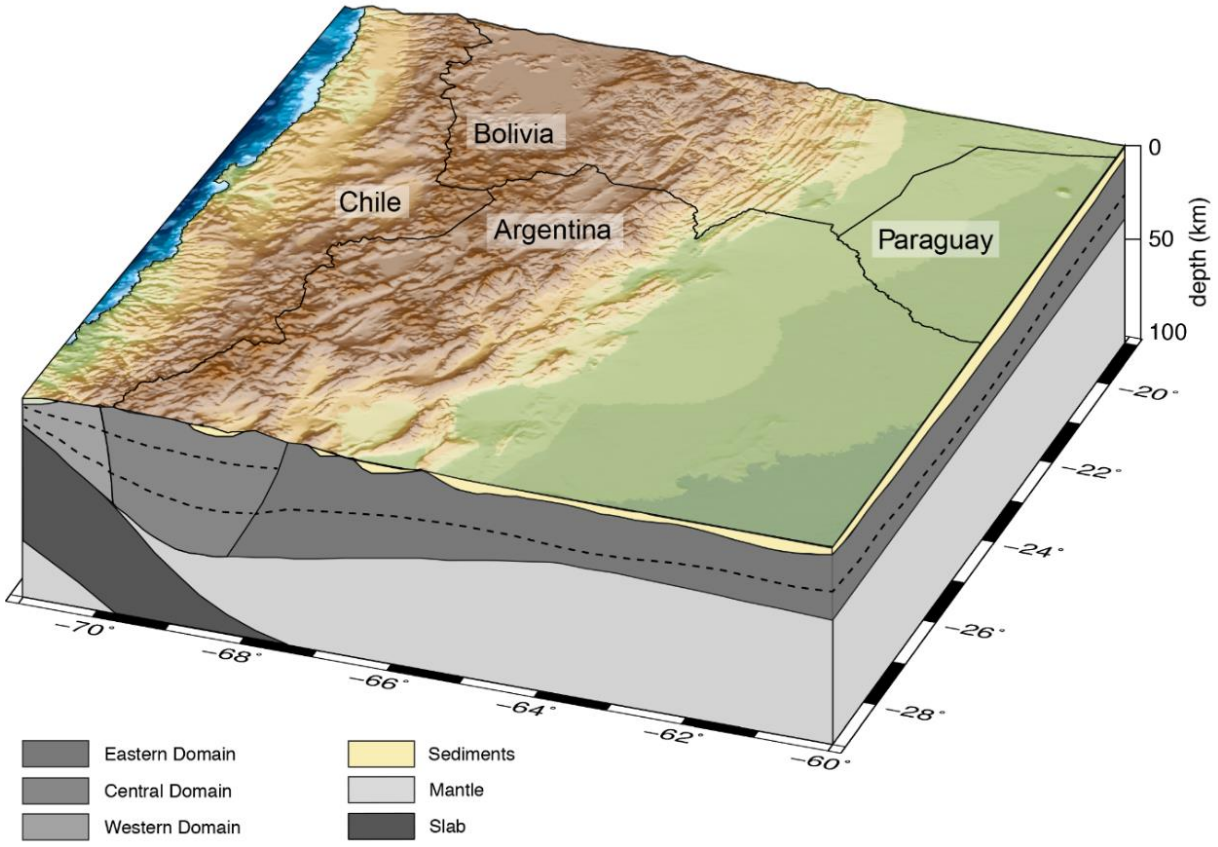

Figure 4.2: Scheme of the 3D density model cropped to 100 km depth showing the different domains within the crust. The domains of the Atacama Block and the APMB-SPMB are not visible because of their restricted geographical extension. Dashed black lines represent boundaries between upper, middle, and lower crust. Black lines on top of digital elevation model denote political borders for reference.

Each unit was assigned fixed bulk thermal conductivity and radiogenic heat production values on the basis of its prevailing lithology and published laboratory measurements of rock samples with comparable lithologies (Table 4.I; Čermák and Rybach, 1982; Vilà et al., 2010). The annual mean surface temperature distribution derived from global climatological models was set as the upper boundary condition (Banzon et al., 2016; New et al., 2002; Reynolds et al., 2007; Figure 4.3), and the temperature distribution at 100 km depth within the mantle as the lower boundary condition (Figure 4.3).

The selection of this particular depth as the base of the thermal model guarantees that it includes only the lithospheric part of the mantle, in which the initial assumption of conduction as the main mechanism for heat transport was likely to be valid. The decision for this particular depth is based on receiver function studies across the region that imaged the lithosphere-asthenosphere boundary as shallow as 100 km (Heit et al., 2008, 2007a). In order to maintain coherence between the density and thermal models, the temperature distribution was taken from the conversion of seismic velocities into density and temperature presented in Chapter 3. For further details about the method see Appendix A.

Table 4.I: Thermal properties of the model units.

Model unit	Thermal conductivity, $\boldsymbol{\lambda}$ (W m^{-1} K^{-1})[1]	Radiogenic heat production, $\boldsymbol{S}$ (μW m^{-3})[2]
Sediments	2.40	0.8
Upper Crust Eastern Domain	2.90	1.2
Lower Crust Eastern Domain	2.60	0.6
Upper Crust Central Domain	2.90	1.8
Middle Crust Central Domain	2.90	1.6
Lower Crust Central Domain	2.70	0.8
Upper Crust Western Domain	2.50	0.7
Middle Crust Western Domain	2.65	0.7
Lower Crust Western Domain	3.90	0.2
Upper Crust Atacama Block	2.60	1.2
Middle Crust Atacama Block	2.60	1.0
Lower Crust Atacama Block	2.30	0.5
Upper Crust APMB-SPMB	2.60	1.8
Middle Crust APMB-SPMB	2.60	1.6
Oceanic Crust	2.30	0.4
Lithospheric mantle	2.90	0.02

[1] Čermák and Rybach (1982); [2] Vilà et al. (2010).

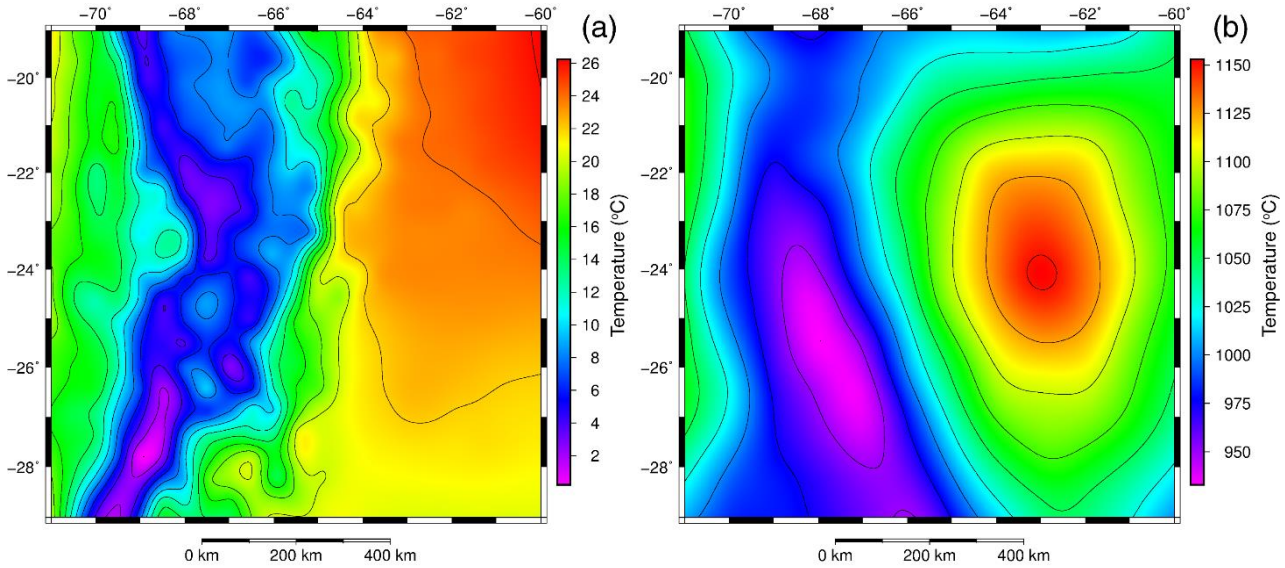

Figure 4.3: Temperature distribution in (a) the upper boundary condition (at the Earth surface), and (b) the lower boundary condition (at 100 km depth).

4.2.2. Calculation of depth to the bottom of the magnetic layer

The magnetic field of the lithosphere results from contrasts in rock magnetization; which reflect the difference in composition and properties of rocks within the crust (Thebault and Vervelidou, 2015). It is considered that the bottom of the magnetic layer represents the surface where the transition between magnetic rocks and non-magnetic rocks occurs, either due to a compositional change or a modification of the magnetic properties of minerals when Curie temperature is reached. Magnetite is the most common magnetic mineral in the lithosphere, however, it is mainly concentrated in the crust and sparse to absent in the mantle; accordingly, the Moho has been proposed as a magnetic boundary (Wasilewski et al., 1979).

The modification of magnetic properties as a function of temperature has been largely investigated since the early studies of Pierre Curie in the XIX century. Weiss and Foex (1911) defined the Curie point (also called Curie temperature) as the temperature at which materials lose their ferromagnetic properties. The Curie temperature of magnetite is ~575-585°C (Hunt et al., 2013); given than the typical geothermal gradient for

continental regions is ~25°C/km (Lowell et al., 2014), and Moho depths are commonly greater than 25 km, the Curie temperature of magnetite is reached within the crust and consequently, the Curie point depth (CPD) is generally the bottom of the magnetic layer.

The method used in this chapter to estimate the depth to the bottom of the magnetic layer (Z_b) relies on the spectral analysis of magnetic anomalies. It follows the approach of Tanaka et al. (1999), based on the formulations of Okubo et al. (1985) to integrate the centroid method of Bhattacharyya and Leu (1977) and the spectral analysis method of Spector and Grant (1970). The centroid method recognizes that there is no wavelength in which the signal of the bottom of a magnetic body dominates the signal of its top, and proposes an alternative approach for the calculation of Z_b, consisting on the determination of the depths to the top (Z_t) and the centroid (Z_0) of the body (Bhattacharyya and Leu, 1977; Okubo et al., 1985). Since Bhattacharyya and Leu (1977) formulated their method for isolated magnetic anomalies, the integration of the spectral analysis of Spector and Grant (1970) that examines patterns of magnetic anomalies makes it more suitable for regional studies (Tanaka et al., 1999). The method assumes that the sources of the anomalies are rectangular vertical prisms with random magnetization and no remnant component.

A key point of the methodology is the determination of the window size for the calculation of the spectrum, because it controls the trade-off between maximum investigation depth and horizontal resolution. Blakely (1996) suggests using windows between 50 and 160 km to cover the whole range of possible depths, however, more recent studies and model simulations suggest an optimal dimension of about 10 times the investigation depth (Chiozzi et al., 2005). Additionally, the application of the "moving window" technique with superposition of windows between consecutive steps prevents the isolation of the signal in each window, working as a low-pass filter that reduces the effect of peaks (Chiozzi et al., 2005).

The magnetic anomaly of the region of interest was extracted from the global model EMAG2 v2 (Earth Magnetic Anomaly Grid), compiled from satellite, marine, aeromagnetic and field measurements (Figure 4.4; Maus et al., 2009). Given the lack of data for the entire extension of the density model, the estimates of depth to the bottom of the magnetic layer are restricted between 64°W and 69°W. The selected window size was 200 km by 200 km with a superposition of 50% in both, N-S and E-W directions, resulting in a total number of 64 windows. The spectrum within each window was calculated with the software Oasis Montaj. The depth from the surface to the top (Z_t), centroid (Z_0), and bottom (Z_b) of the magnetic source, considered as a semi-infinite horizontal layer, were calculated using the following equations:

$$\ln\left[\left[P_{(s)}\right]^{1/2}\right] = B - 2\pi|s|Z_t \tag{4.2}$$

$$\ln\left[\frac{\left[P_{(s)}\right]^{1/2}}{|s|}\right] = \ln D - 2\pi|s|Z_0 \tag{4.3}$$

$$Z_b = 2Z_0 - Z_t = CPD \tag{4.4}$$

where $P_{(s)}$ is the radially averaged power spectrum of the anomaly, s is wavenumber (in cycles/km), and B and D are constants (Bhattacharyya and Leu, 1977; Okubo et al., 1985; Spector and Grant, 1970).

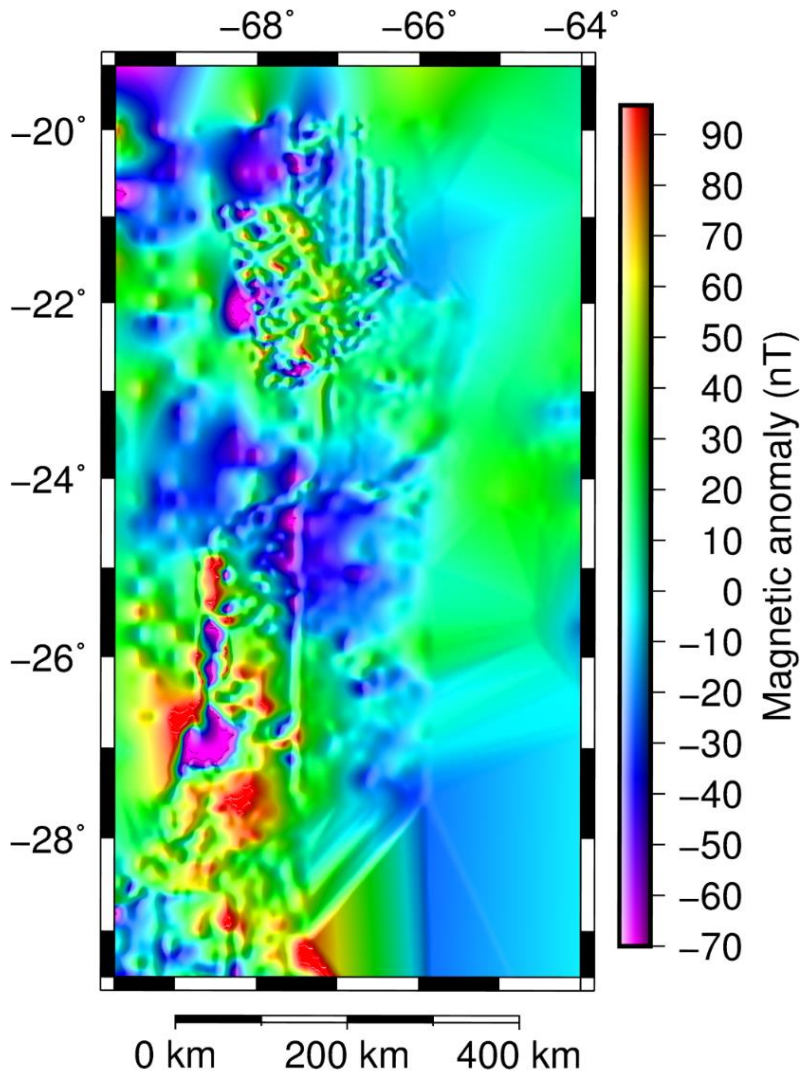

Figure 4.4: Magnetic anomaly of the region at 4 km altitude extracted from the global model EMAG2 v2.

4.2.3. Calculation of surface heat-flow from the bottom of the magnetic layer

Following the previous section, the definition of the depth to the bottom of the magnetic sources, interpreted as the depth to the Curie isotherm, provides information on the thermal state of the lithosphere and allows for an estimation of surface heat-flow. The geothermal gradient (GG) associated with each CDP, assuming that heat is transferred solely by conduction, was calculated as follows:

$$GG = \frac{T_2 - T_1}{Z_2 - Z_1} \tag{4.5}$$

where T_2 is Curie temperature (585°C), T_1 is mean annual surface temperature (10°C), Z_2 is Curie point depth, and Z_1 is the reference level (0 m).

Assuming a constant thermal conductivity (λ) of 2.5 W/mK (Jaupart and Mareschal, 2011) between the Curie point depth and the surface, the heat-flow (Q) at the surface was calculated with the formula:

$$Q = GG \cdot \lambda \tag{4.6}$$

4.3. Results

4.3.1. 3D steady-state conductive thermal field

Depth slices from the model are presented in Figure 4.5. The same general trend can be seen at all depths, with the orogen being generally hotter than the adjacent domains. Since the plotted temperature maps correspond to depth below the surface, topographic effects can be excluded from the interpretations. Temperatures increase from the Eastern Domain towards the Central Domain and then decrease again to the Western Domain (towards the trench). There are high temperatures throughout the Western Cordillera and the Altiplano-Puna plateau, particularly beneath the southern Puna (spatially correlated with the SPMB), and beneath the boundary area between the Altiplano and the northern Puna (spatially correlated with the APMB). The high temperature anomalies become more conspicuous with depth towards the middle crust, but then become progressively less well defined within the lower crust. The southern temperature anomaly covers a smaller area than the northern one, as well as being less distinct and more irregular.

At depths of 5 to 10 km in the upper crust the temperature range of the anomalies corresponding to the APMB and the SPMB is 325-475°C, compared to average temperatures in the Central Domain of 275°C to 400°C (Figure 4.5, a & b). In the middle crust, at depths of 25 km to 40 km, the average temperature for the same region is between 675°C to 875°C, with the anomalies reaching up to 780°C to 960°C (Figure 4.5, c & d). The average temperature in the lower crust of the Central Domain is close to 1000°C at 60 km depth (Figure 4.5e). The average temperatures in the upper crust (5-10 km) decrease towards the Western and Eastern Domains to 160-260°C (Figure 4.5, a & b). In the Western Domain, temperatures increase with depth to up to 450°C in the middle crust and 600°C in the lower crust (Figure 4.5, c & d), while in the Eastern Domain, there is a progressive increase in average temperature with depth , reaching 600°C at the Moho (Figure 4.5f).

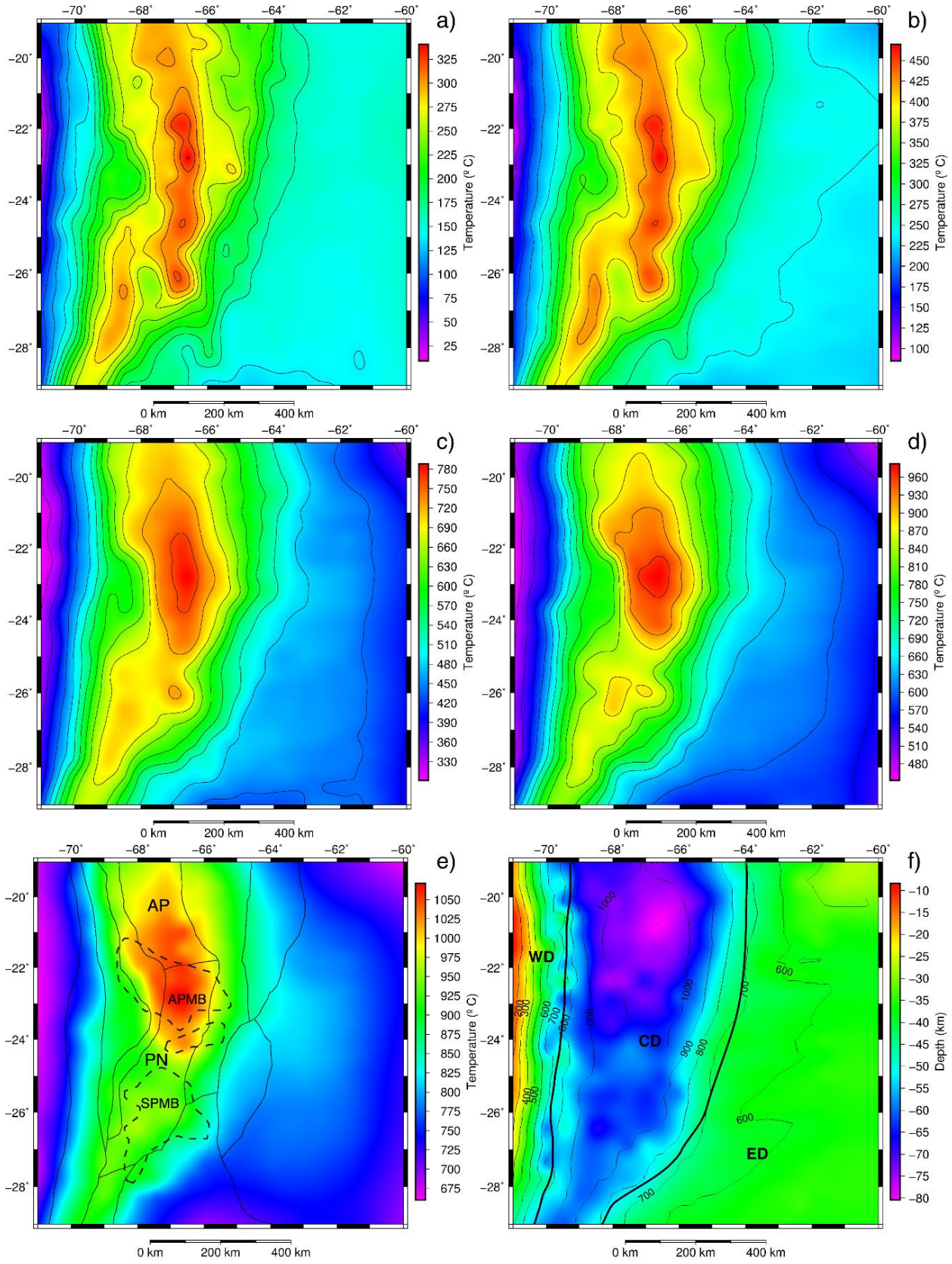
a)
b)
c)
d)
e)
f)
−70˚ −68˚ −66˚ −64˚ −62˚ −60˚
−20˚ −22˚ −24˚ −26˚ −28˚
0 km 200 km 400 km
Temperature (º C)
Depth (km)
AP
APMB
PN
SPMB
WD
CD
ED

Figure 4.5: Depth slices of the thermal model below the surface at (a) 5 km, (b) 10 km, (c) 25 km, (d) 40 km, and (e) 60 km. Solid and dashed black lines in (e) delineate the morphotectonic units and the location of the APMB and the SPMB, respectively. (f) Moho depth with contour lines of temperature distribution, thick solid black lines outline the three main model domains. WD: Western Domain; CD: Central Domain; ED: Eastern Domain; AP: Altiplano; PN: Puna.

Although surface heat-flow is a parameter that is difficult to compare (Hamza and Muñoz, 1996; Scheck-Wenderoth and Maystrenko, 2013), it does provide information on the general trend of the thermal field throughout the region. A comparison of surface heat-flow derived from the model with that measured in the field (Hamza and Muñoz, 1996; Henry and Pollack, 1988; Springer and Förster, 1998; Figure 4.6) shows that the general trend is well reproduced; surface heat-flow is high in the Central Domain and reduces towards the Western Domain and Eastern Domain. The highest modelled values are found in the volcanic arc, the Eastern Cordillera, and the northern Puna, in agreement with measurements obtained within the volcanic arc. Unfortunately, there is no data in the Puna and the Eastern Cordillera.

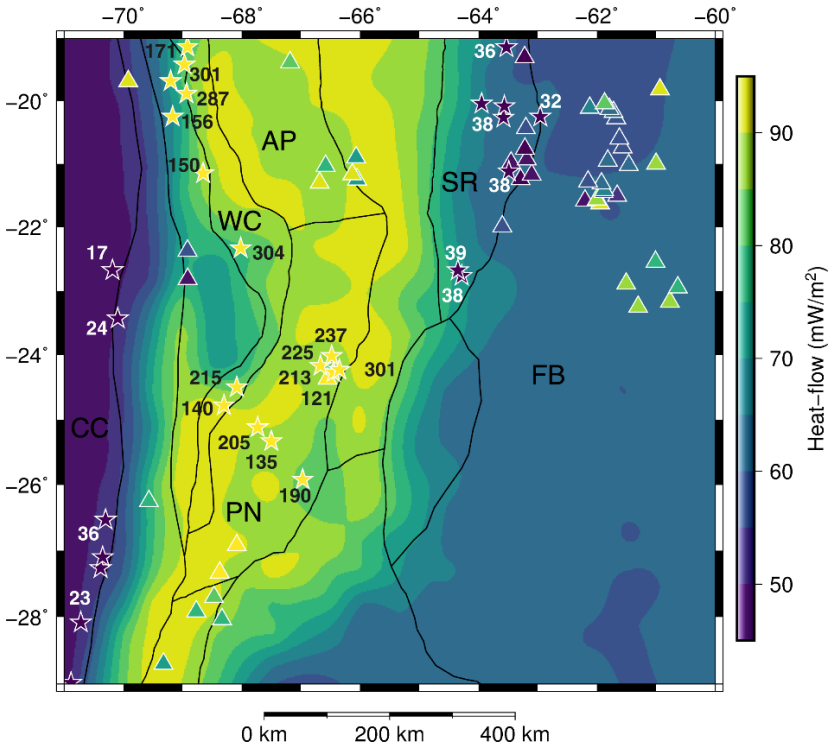

Figure 4.6: Modelled surface heat-flow map and single point surface heat-flow measurements (triangles and stars). Measured data is represented with the same color scale as modelled heat-flow. Stars indicate data points outside the range of the scale, for which the corresponding value is presented. Solid black lines outline the morphotectonic units. CC: Coastal Cordillera; WC: Western Cordillera; AP: Altiplano; PN: Puna; SR: Subandean Ranges; FB: Foreland Basin.

4.3.2. Depth to the Curie isotherm and associated surface heat-flow

Figure 4.7a shows the calculated depth to the bottom of the magnetic layer, interpreted as the Curie isotherm, which is relatively shallow throughout the whole region (~5-24 km). An area with depths shallower than 13 km is recognized in the Western Cordillera and Puna plateau, where the active volcanic arc (Western Cordillera), the APMB, and the SPMB are located. In the same morphotectonic units, between 23°S and 25.5°S, there is a region showing particularly shallow depth to the isotherm, with an average depth of ~7 km. Towards the Altiplano (north of 21°S), the Pampean Ranges (south of 27°S) and the Eastern Cordillera (east of 66°W), the isotherm deepens to ~16-23 km. Additionally, the depth appears to increase to the west in the Chilean Precordillera, reaching up to ~15 km between 21°S and 23.5°S.

As expected, the calculated surface heat-flow (Figure 4.7b) shows a close correlation with the depth to the Curie isotherm (Figure 4.7a). Regions with high surface heat-flow coincide with shallow depths to the Curie isotherm and vice versa. In the volcanic arc (Western Cordillera) and the Puna plateau, surface heat-flow is higher than 100 mW/m^2, with extreme values higher than 150 mW/m^2 and up to 260 mW/m^2 in most of the volcanic arc and northern Puna between 23°S and 25.5°S. In the Altiplano, Pampean Ranges and Eastern Cordillera, surface heat-flow is reduced to 80-95 mW/m^2, which still represents a high surface heat-flow.

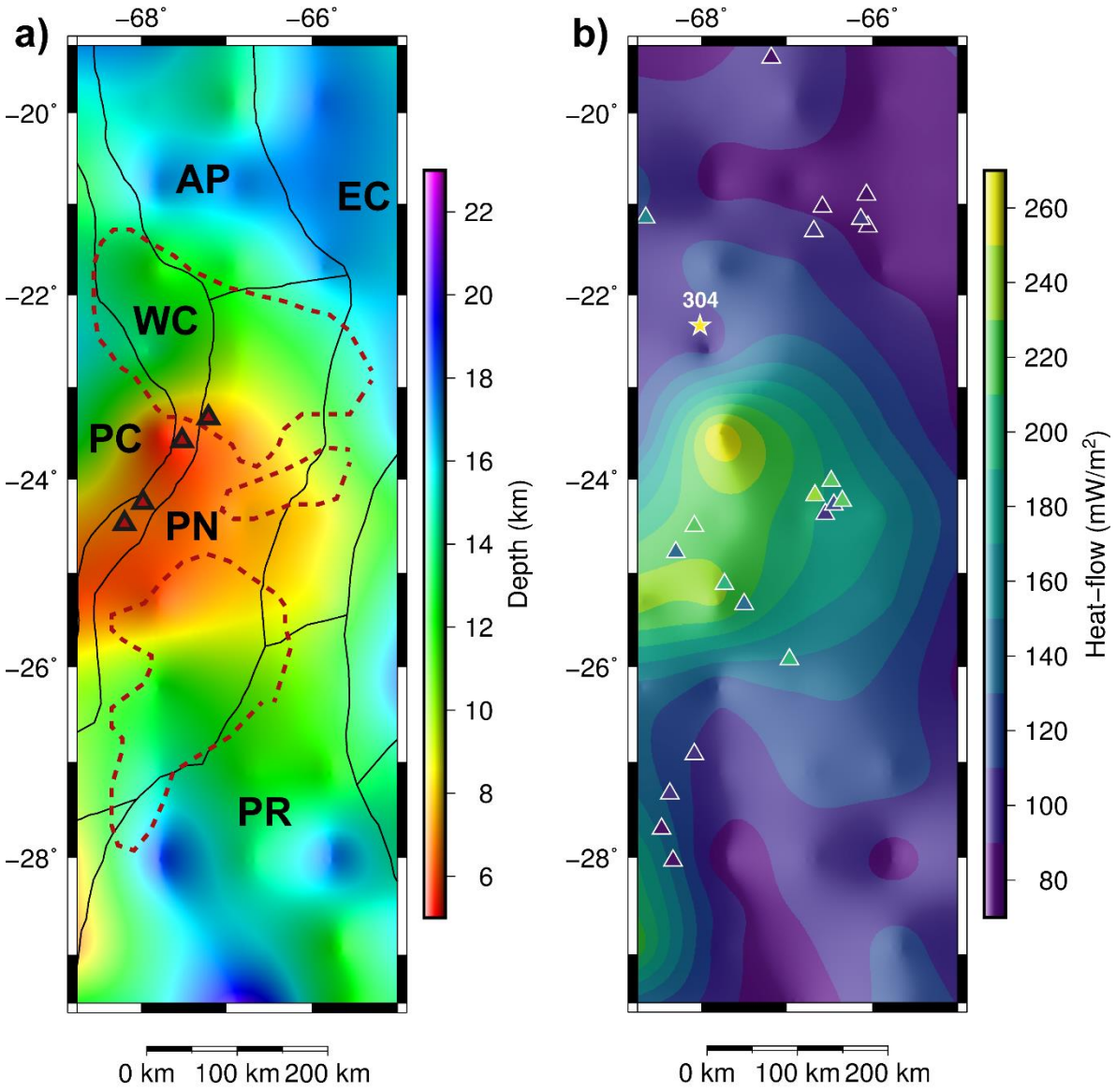

Figure 4.7: (a) Depth from the surface to the Curie isotherm. Solid black lines outline the morphotectonic units, red dashed lines delineate the Altiplano-Puna and Southern Puna magma bodies, and red triangles mark the location of the most active volcanoes in the arc (Socompa, Láscar, Llullaillaco, La Pacana). (b) Calculated surface heat-flow map and single point surface heat-flow measurements (triangles and stars). Measured data is represented with the same color scale as calculated heat-flow. Stars indicate data points outside the range of the scale, for which the corresponding value is presented. AP: Altiplano; PN: Puna; WC: Western Cordillera; PC: Precordillera; EC: Eastern Cordillera; PR: Pampean Ranges.

4.4. Discussion

4.4.1. Validation of the 3D thermal field

The modelled thermal state of the lithosphere presented in this chapter is based on the assumptions that heat is transported solely by conduction and that the system is in thermal equilibrium. Published research has demonstrated that heat conduction is the prevailing mechanism for heat transport within the lithosphere (e.g., Jaupart and Mareschal, 2007; McKenzie et al., 2005), and that steady-state conditions are valid for subduction systems that are old enough for the thermal structure in the mantle to have equilibrated (i.e. at least 200 m.y. old), which is the case for the Andes (e.g., Allmendinger et al., 1997; Hall, 2012; Isacks, 1988). However, the crust also exerts some control over the thermal field and the Andean crust is known to have thickened over the past 40 m.y. (e.g., Lamb, 2015; Lamb and Davis, 2003; Quade et al., 2015; Russo and Silver, 1996; Somoza, 1988), a period that may be too short for thermal equilibrium to have been achieved. There has also been extensive magmatic activity in the arc as well as in the backarc (particularly during the past 15 m.y.; Kay et al., 2010; Kay and Coira, 2009; Trumbull et al., 2006), associated with hydrothermal activity and exceptionally high surface heat-flow, reflecting mechanisms of advective/convective heat transport in the uppermost crustal levels (Hamza and Muñoz, 1996; Henry and Pollack, 1988; Springer and Förster, 1998).

The advection of cooler crustal material to deeper levels through crustal stacking would initially reduce the temperature at those levels. However, an increase in temperature would be expected with time in response to high radiogenic heat production from the stacked upper crustal units and progressive thermal equilibration through heat conduction. The steady-state model would therefore overestimate temperatures in the middle crust of the Central Domain if thermal equilibrium has yet to be achieved in the region. Nonetheless, the results obtained from geothermobarometric investigations (Burns et al., 2015; Kay et al., 2010; Schmitt et al., 2001) are in agreement with the temperatures modelled for the middle crust of the Central Domain. Geothermobarometry relies on different chemical equilibria in minerals to estimate the depth and temperature

at which the magma from which the rocks derived was last in equilibrium. Crustal temperatures calculated for recent eruptive deposits (less than 2.5 m.y. old) on the Altiplano-Puna plateau indicate the presence of a deep magma reservoir at 17-20 km depth, with temperatures up to 965°C (Schmitt et al., 2001). Since these estimates and the low resistivity and seismic velocity reported for the middle crust (e.g., Bianchi et al., 2013; Chmielowski et al., 1999; Ward et al., 2013, 2014) are consistent with the presence of partial melts (such as the APMB and the SPMB), I suggest that the model does not in fact overestimates the temperatures at this depth in the Central Domain, which it would be expected to do if the system was far from thermal equilibrium.

For the shallow upper crust, the same geothermobarometric calculations indicate a shallow magma reservoir at 4-8 km depth with temperatures of 770-890°C (Burns et al., 2015; Kay et al., 2010), suggesting that the model may underestimate the local temperature by as much as 450°C. The modelled values for surface heat-flow within the Central Domain rarely exceed 90 mW m-2, providing a good fit in the Altiplano, but not in the Puna and the volcanic arc, where most measurements are higher (up to 320 mW m-2; Figure 4.6). In these regions, anomalously high surface heat-flow has been reported for those locations with active volcanism and hydrothermal activity; associated convective and advective processes could therefore explain the large discrepancies between the measured and the modelled temperatures and surface heat-flow for this part of the Central Domain.

In the Western Domain there are only surface heat-flow measurements available for comparison with the model. Although the general trend is reproduced and the lowest surface heat-flow values are modelled in this domain, the heat-flow modelled for the Coastal Cordillera (60 mW m-2) is not as low as the available measured data, which can be as low as 20 mW m-2 (Figure 4.6). Low temperatures and surface heat-flow in this domain are consistent with the mafic nature of the crust and the progressive crustal thinning towards the trench, which increases the thickness of the mantle within the model space. Crustal mafic rocks and mantle rocks are characterized by low and extremely low radiogenic heat production, respectively (Table 4.I), and the radiogenic contribution to the

heat budget is therefore greatly reduced compared to that in the Central Domain. The presence of basaltic rocks in the upper crust of the Coastal Cordillera that are fractured and permeable allows infiltration and gravity-driven groundwater flow from the continent to the ocean (Burns et al., 2016; Flóvenz and Saemundsson, 1993), which would reduce the temperatures at shallow depths, and may explain the differences between modelled and measured surface heat-flows.

The temperatures and surface heat-flow in the Eastern Domain are intermediate to those in the Central and Western Domains. Although the crust is as thick as in the Western Domain, the rocks are more felsic and produce more radiogenic heat (Table 4.I), thus increasing the heat input into the system. The model predictions agree with bottom-hole temperatures recorded from depths ranging between 1300 and 3800 m (Collo et al., 2018) to within 8.2°C on average, with modelled temperatures in most cases cooler than those measured in the wells (Figure 4.8). The best fit of the surface heat-flow data is achieved in this domain, although there is a local opposing trend between modelled and measured heat-flow, with modelled heat-flow decreasing towards the east but measured heat-flow increasing in the same direction (Figure 4.6). As in the Western Domain, convective processes in the form of groundwater flow could explain small differences between modelling results and observations. The Subandean Ranges are an area of recharge in which infiltration of cold meteoric water occurs, which would reduce shallow subsurface temperatures. As it infiltrates, the meteoric water is heated and, due to the high elevation and active thrusting in the ranges, it flows driven by pressure and gravity towards the foreland, possibly increasing the temperature of the foreland aquifers (Husson and Moretti, 2002). As these aspects of coupled heat and fluid transport are not taken into account in the model, it may tend to overestimate temperatures in the shallow subsurface of the Subandean Ranges and underestimate temperatures in the foreland.

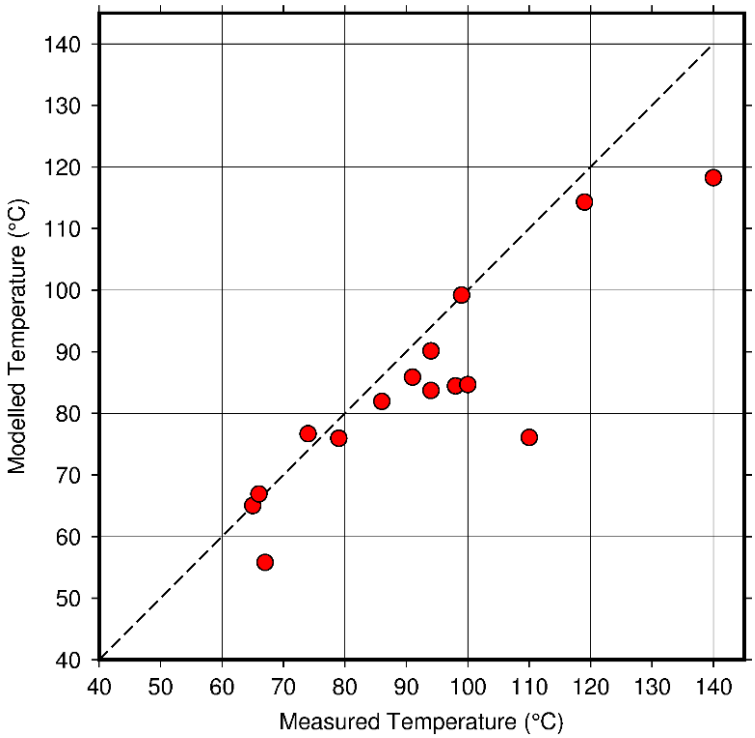

Figure 4.8: Modelled temperature plotted against bottom-hole temperature measurements (red circles). The dashed black line represents a 1:1 relation between X and Y axes.

Although a stronger validation of the model would require better and larger datasets of temperature and surface heat-flow distribution, the results show that in general, shallow temperatures and surface heat-flow data are better reproduced in those regions where advective processes are less pronounced. Improving the model further would require better data (which is currently not available) to increase the structural resolution and simulate coupled heat and fluid transport. Being aware of the limitations of the thermal modelling approach, and keeping in mind that the scope of the dissertation is to evaluate how the variations in the thermal field, as controlled by the well-constrained geological structure, impact on the rheological state of the lithosphere, the presented 3D conductive thermal model is considered as an adequate approximation of the thermal state of the region.

4.4.2. The role of the crust

There is ongoing debate regarding the timing and relative importance of radiogenic heat production in the evolution of orogens, in plateau formation, and in crustal melting. Some authors have ruled out radioactivity as an important heat source because of the long time required to reach thermal equilibrium (e.g., Hyndman et al., 2005). In this line, Babeyko et al. (2002) suggested on the basis of 2D geodynamic models that the radiogenic heat generated in the Central Andes is insufficient to produce elevated temperatures and partial melting in the middle crust without any contribution from an additional heat source, and that advection of hot material from an anomalously hot mantle or lower crust is therefore necessary to explain the observed effects.

These conclusions have, however, recently been indirectly challenged by Chen et al. (2019). These authors have demonstrated on the basis of 3D geodynamic modelling for the Tibetan Plateau that thickening a crust with high radiogenic heat production results in a marked increase in temperature after 30-40 m.y., accompanied by the generation of partial melts within the middle crust. The Andes are currently in a similar time window of their evolution, which means that more than 40 m.y. of shortening and crustal stacking could explain the observed geophysical anomalies consistent with partial melting and the widespread felsic volcanism throughout the plateau (e.g., Bianchi et al., 2013; Chmielowski et al., 1999; Ward et al., 2013).

Furthermore, on a general modelling perspective, Vanderhaeghe (2012) proposed a generic model of the thermo-mechanical evolution of orogenic belts. In this model, the transition from low geothermal gradient and wedge geometry to high geothermal gradient and orogenic plateau is associated with the increased heat production of the thickened crust, melt production and rheologic weakening. The required condition for a significant temperature increment in the models is incubation of the thick crust for 10-20 m.y. in a stable region away from the deformation front, a scenario compatible with the present-day structural configuration and the evolution of the Altiplano-Puna plateau.

Although the steady-state model presented here is unable to discriminate between the alternative hypotheses of thermal evolution (crust vs mantle controlled), its results are in agreement with those of Chen et al. (2019) and Vanderhaeghe (2012) with regard to the significance of the large amount of radiogenic heat produced by thickened crust. The results of the model show that the increased thickness of the crust and consequent elevated production of radiogenic heat have a major influence on the thermal field in the Central Domain and explain the high temperatures compared to the Eastern and Western Domains. Moreover, our model predicts positive thermal anomalies in those domains where crustal melts are inferred from seismic velocity and electric conductivity (e.g., Bianchi et al., 2013; Chmielowski et al., 1999; Ward et al., 2013, 2014).

4.4.3. Depth to the bottom of the magnetic layer and thermal field

The depth to the bottom of the magnetic layer, interpreted as the Curie isotherm, and the surface heat-flow calculated on its basis present a heterogenous pattern throughout the plateau (Figure 4.7). The results show that the Altiplano exhibits a deeper Curie isotherm than the Puna, suggesting a difference in the shallow thermal field between both regions, as evidenced by the measured surface heat-flow (Hamza and Muñoz, 1996; Henry and Pollack, 1988; Springer and Förster, 1998). Moreover, the isotherm is particularly shallow beneath the volcanic arc (Western Cordillera) and the northern Puna, in coincidence with the location of the most active volcanoes in the region (Láscar, Socompa, Llullaillaco, La Pacana caldera; Stern, 2004), and overlapping partially with the APMB and the SPMB. In the same locations, the magnetotelluric and deep geomagnetic studies of Schwarz et al. (1994) and the attenuation tomography of Schurr et al. (2003) have shown the highest electric conductivities and seismic attenuation, leading the authors to suggest the presence of pathways for fluid and melt transport within the crust. It is therefore likely that the enhanced transport of heat by convective and advective processes in those pathways through time resulted in an increment of temperatures beneath the volcanic arc and the northern Puna compared to those in the Altiplano.

A comparison between the depth to the Curie isotherm and the temperature estimates based on geothermobarometers (e.g., Burns et al., 2015; Kay et al., 2010) reveals an underestimation of approximately 200°C at 4-8 km, which is high but reduced when compared to the discrepancies between those estimates and the conductive 3D model. The horizontal resolution of the depth to the Curie isotherm (100 km), imposed by the limitation of the methodology to provide high resolution when exploring deep sources, has to be considered as an important uncertainty source. Additionally, it has been shown that the method employed here works as a low-pass filter, depending on the window size, smoothing the variability of the thermal field and masking local thermal anomalies (Chiozzi et al., 2005). On the other hand, the temperatures calculated with geothermometers usually provide absolute uncertainties of 50°C.

With respect to surface heat-flow, the quality of the compiled data is highly variable; some values were obtained through conventional methods while others are estimations based on geochemical methods (for a detailed description of the data see Hamza and Muñoz 1996, and Hamza et al. 2005). The limitations imposed by the sparse and scattered available data are obvious; besides, it is difficult to assess the range of uncertainty in the measurements. Nevertheless, there is a good correlation between measurements and surface heat-flow calculated from the Curie isotherm. In the Altiplano, calculated surface heat-flow varies between 80-95 mW/m^2, which is consistent with measurements of 70 mW/m^2 to 94 mW/m^2. In the southern Puna, both measured and calculated heat-flow are larger than in the Altiplano, with values between 90-237 mW/m^2 and 110-250 mW/m^2, respectively (Figure 4.7b).

Even though advective/convective processes and radiogenic heat production are not taken into account in the calculation of surface heat-flow from the Curie isotherm, the method is capable of reproducing the heterogeneities of the plateau and the anomalous high surface heat-flow values. This suggests that the distribution of the magnetic anomalies, and the derived depth to the Curie isotherm, indeed carry a signal of the present-day thermal field resulting from conductive, convective, and advective processes. Previous studies in other regions have also shown a good correlation between calculated

and measured heat-flow (reproducing high values), as well as shallow Curie depths in volcanic areas or hot springs (e.g., Aydin et al., 2005; Hsieh et al., 2014; Nwankwo and Shehu, 2015). It can be concluded that, in spite of the limitations of the method, the assessment of the depth to the Curie isotherm represents a fairly good tool to provide lower boundary conditions for the determination of the shallow temperature distribution of the crust.

4.5. Summary and conclusions

The steady-state conductive 3D thermal field for the Central Andes was modelled on the basis of the data-derived density model. Furthermore, the shallow subsurface (upper crustal) temperature distribution beneath the Altiplano-Puna plateau and surrounding regions was constrained by calculating the depth to the Curie isotherm from the magnetic anomalies in frequency domain. The main outcomes are:

1. the deep temperature distribution is primarily controlled by the thickness and composition of the crust. The thick and felsic crust with high radiogenic heat production in the orogen presents higher temperatures than the forearc and foreland, despite these two areas having higher temperatures at the lower boundary condition;
2. although convective/advective processes are active in some parts of the Central Andes and thermal equilibrium has probably not yet been attained, the 3D thermal model reproduces measured surface heat-flow and shallow crustal temperature reasonably well in those regions where advective processes are less pronounced;
3. the conductive thermal model predicts positive thermal anomalies spatially coincident with regions in the subsurface characterized by low resistivity and seismic velocity, consistent with the presence of crustal melts in the Altiplano-Puna Magma Body and the Southern Puna Magma Body;

4. the Altiplano and the Puna do not show conspicuous surface heat-flow and temperature differences in the 3D conductive model. However, there is a segmentation of the plateau with respect to the depth to the Curie isotherm and its associated surface heat-flow, in agreement with other observations. The Altiplano exhibits Curie depths between 16-23 km and surface heat-flow values between 80-95 mW/m^2, whereas beneath the Puna, the Curie isotherm is shallower than 13 km, and surface heat-flow values range between 110-250 mW/m^2;
5. the shallowest depths to the Curie isotherm (< 7 km) are located between 23°S and 25.5°S, beneath the volcanic arc and the northern Puna, in spatial coincidence with the most active volcanoes of the region and the highest reported electric conductivities and seismic attenuations, suggesting that convective and/or advective processes in the form of magma and fluids ascending through the crust have enhanced the transport of heat;
6. extremely high surface heat-flow values were reproduced even though convective/advective processes and radiogenic heat production were not taken into account for the calculation of surface heat-flow from the Curie isotherm, suggesting that the latter carries the signal of the present-day thermal field resulting from conductive, convective, and advective processes.

Chapter 5. Rheological state of the Central Andean lithosphere

5.1. Introduction

One possible approach to evaluate the rheological state of the region is to determine the strength distribution within the lithosphere. Goetze and Evans (1979) were the firsts to introduce the concept of the yield strength envelope to describe the strength of the lithosphere (Figure 5.1). The yield strength of rocks is defined as the maximum differential stress ($\Delta\sigma_{max}$) they can resist without experiencing permanent deformation (either brittle or ductile), and is highly dependent on temperature and pressure conditions as well as on the rock composition (Ranalli, 1997):

$$\Delta\sigma_{max} = \sigma_1 - \sigma_3 \tag{5.1}$$

where σ_3 and σ_1 are the minimum and maximum principal stresses, respectively.

When the imposed differential stress is below the yield strength, rocks deform elastically. In the opposite case and as a general rule, rocks in the lithosphere experience brittle deformation at shallow depths and ductile deformation at greater depths, controlled mainly by the temperature distribution. The prevailing mechanism of deformation will be the one that requires the least differential stress at a given depth (Goetze and Evans, 1979).

Brittle behavior is governed by the Coulomb-Navier failure criterion, described by an empirically determined temperature-independent law (Byerlee, 1968), that is usually referred to as Byerlee's law and can be expressed as (Ranalli,1997):

$$\Delta\sigma_b = f_f \rho_b g z \left(1 - f_p\right) \tag{5.2}$$

where $\Delta\sigma_b$ is the brittle yield strength, ρ_b is the bulk density, g is the acceleration due to gravity (g = 9.81 m s^{-2}), z is the depth below topography, f_p is the pore fluid factor (ratio of pore fluid pressure to lithostatic pressure; a typical hydrostatic value is $f_p = 0.36$; Ranalli, 1995), and f_f is a coefficient that depends on the friction coefficient of rocks and the fault type.

Ductile deformation is controlled by solid-state creep mechanisms (dislocation, diffusion and glide). In the crust and upper mantle, dislocation creep is the dominant deformation mechanism (described by the power law in Eq. 5.3). However, when differential stresses of dislocation creep in the mantle are greater than 200 MPa, Dorn's law describing dislocation glide for olivine (Eq. 5.4) yields a better approximation for deformation of mantle rocks (Goetze, 1978; Kirby and Kronenberg, 1987):

$$\Delta\sigma_d = \left(\frac{\dot{\varepsilon}}{A_p}\right)^{\frac{1}{n}} exp\left(\frac{Q_p}{nRT}\right) \tag{5.3}$$

$$\Delta\sigma_d = \sigma_D \left(1 - \left[-\frac{RT}{Q_D} ln \frac{\dot{\varepsilon}}{A_D}\right]^{\frac{1}{2}}\right) \tag{5.4}$$

where $\Delta\sigma_d$ is the ductile yield strength, $\dot{\varepsilon}$ is the reference strain rate, A_p is the pre-exponential scaling factor, n is the power-law exponent, Q_p is the power-law activation energy, σ_D is the Dorn's law stress (σ_D = 8.5E9 Pa), Q_D is the Dorn's law activation energy (Q_D = 535 kJ mol^{-1}), A_D is the Dorn's law strain rate (A_D = 5.7E11 s^{-1}), R is the universal gas constant (R = 8.314 J K^{-1} mol^{-1}) and T is the absolute temperature.

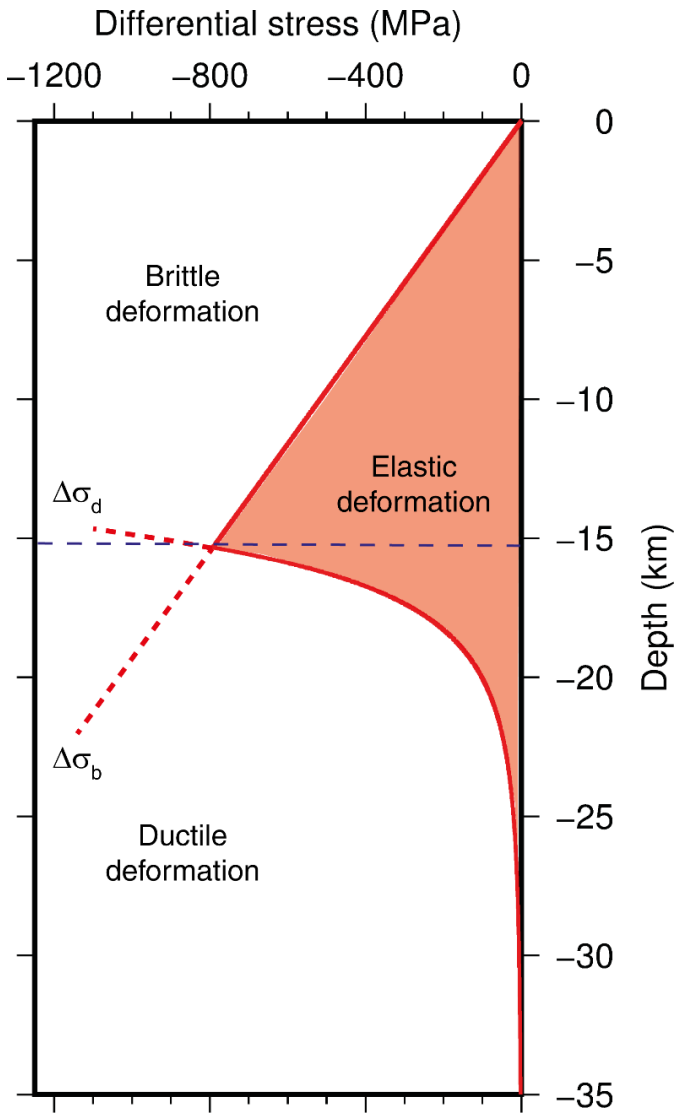

Figure 5.1: General scheme of yield strength envelope construction. Lines corresponding to $\Delta\sigma_b$ y $\Delta\sigma_d$ (straight and curved red lines, respectively) represent the variation of brittle and ductile yield strengths of a rock with depth, respectively. The intersection point between both lines constitutes a brittle-ductile transition (dashed blue line). The full extension in depth of the solid red line, determined by the smallest of the yield strengths at each depth, constitutes the yield strength envelope of the rock. The brittle-ductile transition and the yield strength envelope define the deformation fields of the rock; when, at a given depth, the imposed differential stress is smaller than the yield strength envelope, elastic deformation prevails (red shaded region of the diagram). In the opposite case, plastic deformation occurs (white region of the diagram), as brittle deformation above the brittle-ductile transition, and ductile deformation at greater depths.

Summing up, the yield strength ($\Delta\sigma_{max}$) of a rock at a given pressure-temperature condition within the lithosphere is defined by the minimum of the strengths $\Delta\sigma_b$ and $\Delta\sigma_d$ (Goetze and Evans, 1979; Eq. 5.5). If $\Delta\sigma_d$ is greater than $\Delta\sigma_b$ and the imposed differential stress is sufficiently large, the lithosphere will experience brittle deformation; in the opposite case, ductile deformation will prevail. In this sense, the yield strength envelopes characterize the distribution of yield strength in depth, indicate the prevailing deformation mechanism, and show the position of brittle-ductile transitions (Figure 5.1).

$$\Delta\sigma_{max} = min(\Delta\sigma_b, \Delta\sigma_d) \quad (5.5)$$

Another commonly used indicator of the rheological state of the lithosphere is the effective elastic thickness. The elastic thin plate model has been widely used to describe the response of the lithosphere to internal and external loads (Figure 5.2). According to this model, the lithosphere maintains gravitational equilibrium over long geological time scales by bending over the asthenosphere (Burov and Diament, 1995). The following is a simple formulation of the problem relating flexure and topographic loads:

$$D\nabla^4 w(x,y) + (\rho_m - \rho_c)gw(x,y) = \rho_t g h(x,y) \quad (5.6)$$

where w is deflection, h is topography, g is acceleration of gravity (g = 9.81 m s^{-2}), D is flexural rigidity of the lithosphere, ρ_t is density of the topographic load, ρ_m is density of the mantle and ρ_c is density of the crust.

The flexural rigidity of a lithospheric plate characterizes its resistance to bending moments and depends on the effective elastic thickness of the plate (T_e), the Young modulus (E) and the Poisson ratio (ν):

$$D = \frac{ET_e^3}{12(1-\nu^2)} \quad (5.7)$$

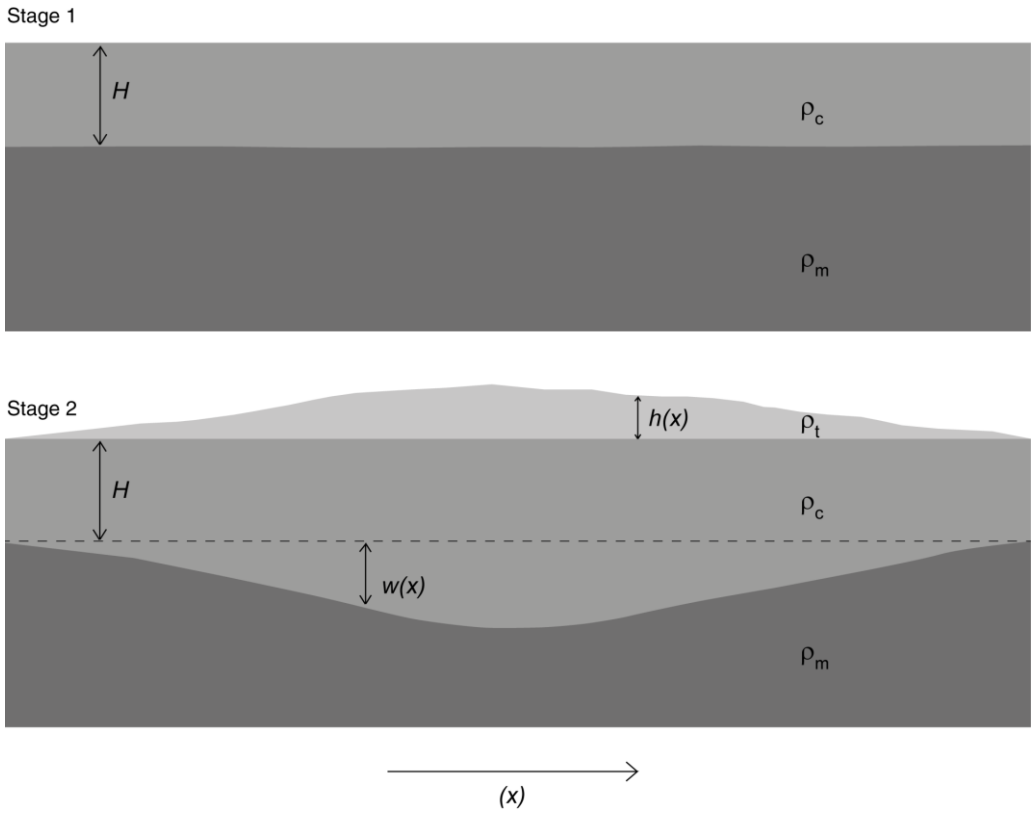

Figure 5.2: Scheme of the elastic thin plate model applied to the continental lithosphere. A crust of density ρ_c in isostatic equilibrium with the mantle (Stage 1) responds elastically to the generation of a topographic load h(x) of density ρ_t, by producing a deflection w(x) over a mantle of density ρ_m (Stage 2). H represents the thickness of the reference crustal column.

As the Young modulus and the Poisson ratio are usually assumed constant in flexural models, the effective elastic thickness is used to describe the rigidity of plates. Even though the effective elastic thickness is commonly used to make inferences on the thermal state and strength of the lithosphere, it is important to note that the concept of T_e is theoretical, and that it represents the equivalent thickness of a plate with homogeneous elastic properties (E, ν); there is no physical representation of this layer in the lithosphere (Stüwe, 2007). Moreover, Burov and Diament (1995) have shown that the relation between T_e and the thermal state of a plate is not straightforward and other parameters should be considered to make inferences. That said, interpretations of T_e should be made carefully.

At present, there are no estimates of strength distribution in the Central Andes except for global models (e.g., Tesauro et al., 2013) showing low strength in the orogen that increases to the adjacent foreland and cratonic regions. On the contrary, estimations of the effective elastic thickness are numerous; several authors have investigated the subject following different methods (e.g., García et al., 2017; Tassara and Yáñez, 2003; Watts et al., 1995). Most of the studies show low T_e values in the orogen that increase towards cratonic regions, and a general inverse correlation between T_e and surface heat-flow.

In this chapter, a 3D model of strength distribution in the Central Andes based on the lithospheric configuration of the 3D density model and the modelled conductive thermal field is presented. The cumulative character of the modelling approach is particularly useful to evaluate how the lithospheric structure determines the present-day rheological state of the region. Estimations of the effective elastic thickness of the lithosphere from different methods are presented as well, in order to test the relation between strength, T_e, and the existing models of rheological stratification of the lithosphere. Furthermore, a geodynamic simulation performed in cooperation with Dr. Sibiao Liu is included to address the dynamic behavior of the system.

5.2. Methods and data

5.2.1. Rheological modelling of strength distribution

The methodology consists in the calculation of maximum differential stresses for both brittle and ductile deformation mechanisms throughout the modelling region. The code of Cacace and Scheck-Wenderoth (2016) was used to compute the 3D strength distribution, which requires the previous definition of the 3D temperature distribution, the structural interfaces delimiting different rock units in the lithosphere, and lithology-dependent mechanical properties for each unit. The calculations build on the density and thermal models presented in Chapters 3 and 4, given that all the required input parameters were taken from and assigned in accordance to those models.

The code calculates the maximum differential stress for brittle and ductile behavior at each X-Y-Z position (Eqs. 5.2, 5.3, and 5.4), and defines the lowest of these as the yield strength at that particular point (Eq. 5.5). Since the Andean tectonic regime is compressive, a f_f representative of thrust faulting and a general friction coefficient of 0.75 was chosen for the calculation of brittle yield strength ($f_f = 3.00$; Ranalli, 1995). The average reference strain rate was extracted from a global model of geodetic plate motion and strain rate based on GPS measurements ($\dot{\varepsilon} \cong$ 6.00E-15 s^{-1} at the Andean margin; Kreemer et al., 2014).

The rheological properties of the model units were taken from published laboratory measurements on common rock types, corresponding to the prevailing lithology of each unit (Table 5.I; Afonso and Ranalli, 2004; Goetze and Evans, 1979; Ranalli and Murphy, 1987; Wilks and Carter, 1990). Since the properties reported for similar lithologies by different authors are not always consistent, the secondary creep parameters were carefully selected to ensure that felsic units are weaker than mafic ones. To achieve this, strength-depth profiles for the different rock types were plotted using a uniform strain rate and a reference geotherm. A detailed description of the selection criteria can be found in Appendix B.

The integration of the yield strength over depth at each X-Y position for the entire lithosphere and the entire crust provides the integrated lithospheric strength and the integrated crustal strength, respectively:

$$\sigma_I = \int_0^z (\sigma_1 - \sigma_3) \times dz \tag{5.8}$$

where σ_I is the integrated strength.

Table 5.I: Densities and rheological properties of the model units.

Model unit	Bulk density, ρ (kg m^{-3})	Rock-type rheology	Power-law activation energy, Q_p (kJ mol^{-1})	Pre-exponential scaling factor, A_p (Pa^{-n} s^{-1})	Power-law exponent, n
Upper Crust Eastern Domain	2880	Quartz diorite, dry[1]	219	5.02E-18	2.4
Lower Crust Eastern Domain	3020	Mafic granulite, dry[2]	445	8.83E-22	4.2
Upper Crust Central Domain	2700	Granite, dry[1]	123	7.93E-29	3.2
Middle Crust Central Domain	2880	Quartz diorite, dry[1]	219	5.02E-18	2.4
Lower Crust Central Domain	3050	Felsic granulite, dry[2]	243	2.01E-21	3.1
Upper Crust Western Domain	2740	Diabase, wet[3]	260	7.96E-25	3.4
Middle Crust Western Domain	3040	Diabase, dry[3]	485	5.05E-28	4.7
Lower Crust Western Domain	2930	Diabase, wet[3]	260	7.96E-25	3.4
Upper Crust Atacama Block	2750	Quartz diorite, dry[1]	219	5.02E-18	2.4
Middle Crust Atacama Block	2930	Diabase, dry[3]	485	5.05E-28	4.7
Lower Crust Atacama Block	3090	Diabase, dry[3]	485	5.05E-28	4.7
Upper Crust APMB-SPMB	2660	Granite, dry[1]	123	7.93E-29	3.2
Middle Crust APMB-SPMB	2830	Quartz diorite, dry[1]	219	5.02E-18	2.4
Oceanic Crust	2900	Diabase, dry[3]	485	5.05E-28	4.7
Lithospheric mantle	3340	Olivine, dry[4]	510	7.00E-14	3.0

[1] Ranalli and Murphy (1987); [2] Wilks and Carter (1990); [3] Afonso and Ranalli (2004); [4] Goetze and Evans (1979). Brittle behavior was imposed on the sediments.

5.2.2. Forward modelling of the effective elastic thickness

The Python code of Soler (2015), which is based on the spectral methods developed by Garcia et al. (2014), was used to calculate the effective elastic thickness. Equations 5.6 and 5.7 provide a good approximation of the method; if the deflection $w(x, y)$, topography $h(x, y)$, densities (ρ_t, ρ_m, ρ_c) and elastic properties (E, ν) are known, then the effective elastic thickness can be calculated. The densities of the topographic load, crust and mantle were defined in accordance with the 3D density model as 2670 kg/m^3, 2850 kg/m^3, and 3330 kg/m^3, respectively. Average values of 100 GPa for the Young modulus (Tesauro et al., 2015) and 0.25 for the Poisson ratio (Zandt and Ammon, 1995) were considered for the elastic properties of the lithosphere.

The Python code requires the Bouguer anomaly as input to calculate the Moho depth through the inversion of gravity and obtain the deflection by subtracting a reference crustal thickness. This deflection together with the input topography is then transformed into the frequency domain and used to calculate the effective elastic thickness. Given the highly heterogeneous nature of the crust beneath the plateau (e.g., Beck and Zandt, 2002; Bianchi et al., 2013; Prezzi et al., 2009; Schurr et al., 2003), using a unique average density for the crust to invert the Bouguer anomaly for the Moho and calculate T_e would result in an oversimplification of the problem. Thus, instead of inverting gravity, the Moho of the density model was used, which is taken from the crustal thickness model for South America of Assumpção et al. (2013).

Furthermore, in order to include the effect of the internal loads that arise from the heterogeneous distribution of density in the crust, a pseudo-topography was calculated from the 3D density model (Eq. 5.9; Ebbing, 2002), and used as input for the code instead of the topography. First, the internal load (L) of each unit in the model was calculated as the difference between its density and the density of the reference crust (ρ_c), multiplied by its thickness at every X-Y position. Then, the total L of each crustal column (i.e. the sum of the L of all units at each X-Y position) was divided by the density of the topographic load (ρ_t) to obtain the thickness of a topographic column with an equivalent load. Finally, this thickness was added to the topography to obtain the pseudo-topography:

$$h_{pt} = h + \frac{\sum_{i=N} h_i(\rho_i - \rho_c)}{\rho_t} \tag{5.9}$$

where h_{pt} is the pseudo-topography, h is the topography, and h_i and ρ_i are the thickness and density of each layer in the density model, respectively.

In order to account for the variations of T_e throughout the region, the code works with square windows assuming that T_e is constant within its interior. Several "try-out deflections" are calculated for a given range of T_e in each window, which are then compared against the input deflection (in this case, obtained from the seismic Moho). The final T_e of each window will be the one that minimizes the standard deviation between the calculated and input deflections.

5.2.3. Determination of the effective elastic thickness from strength distribution

The effective elastic thickness of the lithosphere can also be computed from the strength distribution in the modelling region. According to Burov and Diament (1995), the effective elastic thickness (T_e) of a rheologically stratified lithosphere is calculated as the sum of the mechanical thickness of each layer Δh_i (Eqs. 5.10 and 5.11). The mechanical thickness of a layer (also called mechanically competent layer) is measured from its top to the depth where either the differential stress is less than 1-5 % of the lithostatic pressure, or where it is below 10-20 MPa. For a lithosphere with n coupled competent layers (i.e. competent layers are continuous in depth), T_e is computed as:

$$T_e = \sum_{i=1}^{n} \Delta h_i \tag{5.10}$$

In the case that competent layers are decoupled, T_e is computed using

$$T_e = \left(\sum_{i=1}^{n} \Delta h_i^3 \right)^{\frac{1}{3}} \tag{5.11}$$

When a stratified lithosphere presents multiple coupled and decoupled layers, the thickness of the coupled layers is summed first with Eq. 5.10. Then, the effective elastic thickness is obtained by summing decoupled layers with Eq. 5.11. The calculations were made with the Python tool pyGMS (Meeßen, 2019), using 5 % of the lithostatic pressure to define the base of each mechanically competent layer, and an absolute lower limit of 20 MPa. Consequently, the calculated effective elastic thickness represents the lower limit of possible results (the upper limit is defined by 1 % of the lithostatic pressure and 10 MPa).

5.2.4. Geodynamic modelling of the orogen-foreland system

In cooperation with Dr. Sibiao Liu, a 3D geodynamic model for intraplate compression of the orogen-foreland system was developed, using the crustal structure of the density model as initial configuration. The aim of the model is to assess the dynamic response of the data-constrained crustal configuration to the present-day Andean compression.

The highly scalable advanced geodynamic code LaMEM (Lithosphere and Mantle Evolution Model; Kaus et al., 2016) was used to perform the thermo-mechanical calculations (details on the governing equations are presented in Appendix C). The model domain is restricted to the orogen (Central Domain) and the foreland (Eastern Domain) in the backarc region of the density model between 60°W and 68°W, and 19°S and 29°S (Figure 5.3). The small domains corresponding to the Atacama Block and APMB-SPMB were not considered in order to reduce computational time and facilitate the convergence of the model.

The lithosphere-asthenosphere boundary (LAB) defining the lithospheric mantle in the model was interpolated from the global model of Koptev and Ershov (2011), using the Moho as an upper boundary. The resolution of the model in the latitude and longitude directions is 7 km and 6 km, respectively. A dense grid with 1.2 km of vertical resolution covering the lithosphere down to 200 km depth was implemented to track deformation in the vertical direction of thin units within the crust. For depths between 200 and 400 km, the vertical resolution is 7 km.

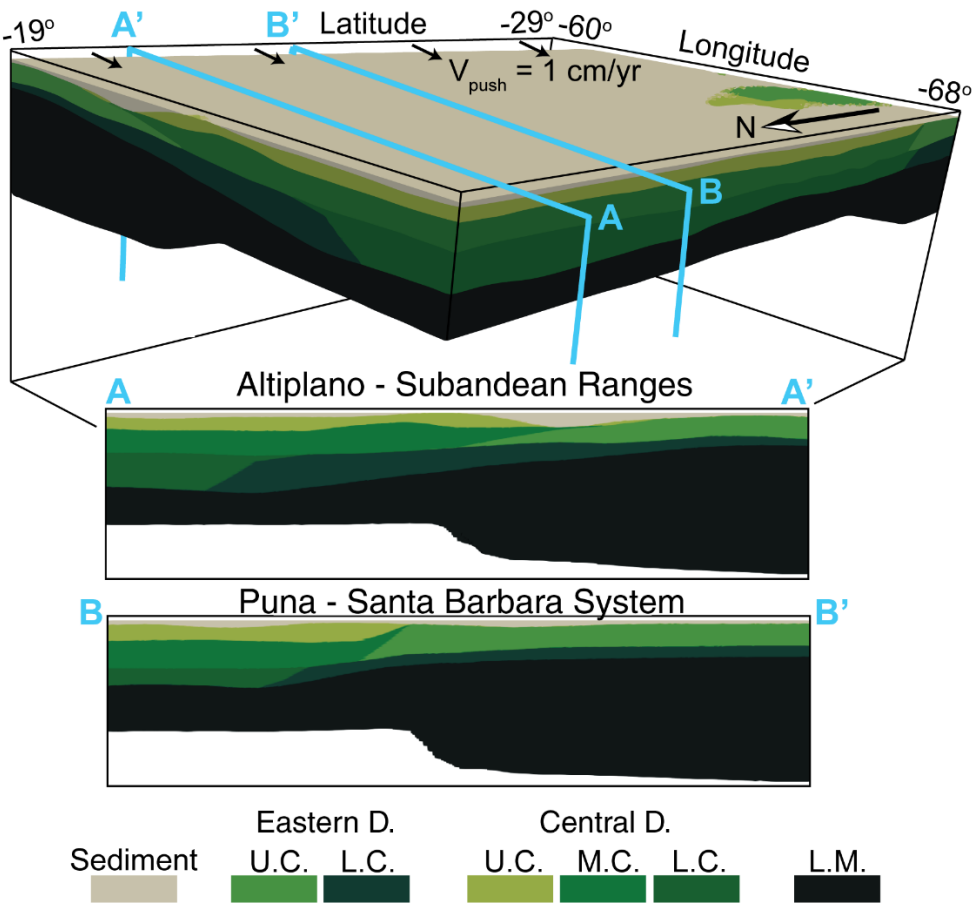

Figure 5.3: Initial setup of the geodynamic model. The structure of the crust is configured from the density model. U.C., M.C., L.C. and L.M. are upper crust, middle crust, lower crust and lithospheric mantle, respectively.

Table 5.II: Mechanical properties of the sediments and mantle used in the geodynamic model

Model unit	Rock-type rheology	Power-law activation energy, $\boldsymbol{Q}$ (kJ mol^{-1})	Pre-exponential scaling factor, $\boldsymbol{A}$ (Pa^{-n}s^{-1})	Power-law exponent, $\boldsymbol{n}$
Sediments	Wet quartzite[1]	154	4.00E-18	2.3
Lithospheric mantle	Dry olivine[2]	375/530/ 540	1.50E03/1.10E-16/6.85E-67	1/3.5/-
Sublithospheric mantle	Wet olivine[2] (Constant C_{OH})	335/480/ 540	1.00/9.00E-20/6.85E-67	1/3.5/-

[1] Ranalli and Murphy, 1987; [2] Hirth and Kohlstedt, 2003.

The geodynamic model was parametrized with the same thermal and rheological properties as in the 3D thermal and rheological models (Table 4.I and Table 5.I), except for the sediments and the mantle. A fully visco-elasto-plastic rheology was considered for all materials, and the mechanisms of ductile deformation in the mantle included diffusion, dislocation, and Peierls creep regimes.

With the purpose of reproducing the first-order trends of the modelled 3D conductive thermal field, the initial thermal structure of the geodynamic model in the crust was defined by a linear gradient of ~14.3°C/km between the surface at 0°C and the Moho. The temperature at the LAB is a function of its depth, defined as the sum of 1300°C and the contribution of a mantle adiabatic gradient of 0.4°C/km. Subsequently, the thermal structure of the lithospheric mantle was defined by a linear gradient between the temperature at the Moho and the LAB. In the sublithospheric mantle, the temperature distribution is governed by the adiabatic gradient of 0.4°C/km, with a resulting bottom temperature of 1460°C. The thermal gradient at the lateral boundaries was set to zero, which means no horizontal heat flux there.

The mechanical boundary conditions included a stress-free surface boundary, and a closed free-slip basal boundary. The amount of intraplate shortening was imposed through a velocity of 1 cm/yr (e.g., Brooks et al., 2011; Oncken et al., 2006) on the right-hand (East) side boundary. Mass balance was maintained using a uniform outflow through the left-hand (West) lateral boundary below the lithosphere of the Andes.

5.3. Results

5.3.1. Rheological model of strength distribution

The modelled integrated strength for the lithosphere and crust are presented in Figure 5.4, together with the percentage of the crustal contribution to the integrated lithospheric strength. Both strength maps show the same pattern, with a relatively low integrated strength in the Central Domain increasing towards the Western Domain and the Eastern Domain. The lowest integrated strengths for both the lithosphere and the crust lie beneath the Altiplano-Puna plateau, where most of the strength resides in the crust, as shown by the high proportion of crustal strength (more than 80 %, Figure 5.4c). The highest integrated lithospheric strength occurs in the Eastern Domain, while the highest integrated crustal strength is in the Western Domain.

Integrated strength maps are useful to analyze horizontal variations in rheology, in turn, yield strength envelopes allow evaluating vertical heterogeneities. In Figure 5.5, yield strength envelopes are plotted for certain locations that are structurally representative of the morphotectonic units within the modelled area (see Figure 5.4c for the location). In the Eastern Domain the mantle is relatively strong, accounting for an important part of the total strength and conforming to the *jelly sandwich* model for the lithosphere (Figure 5.5, a, b & c). In the Subandean Ranges and the Santa Barbara System, the lower crust is rather weak and decoupled from the mantle (Figure 5.5, a & b), in contrast to the Pampean Ranges where the lower crust is strong and coupled to the mantle (Figure 5.5c). The yield strength envelope for the Puna plateau reveals that the strength there resides mainly in the upper crust, conforming to the *crème brûlée* model for the lithosphere (Figure 5.5d). The Atacama Block presents a strong upper crust, a very strong middle crust, and weak lower crust and mantle, conforming as well to the *crème brûlée* model (Figure 5.5e).

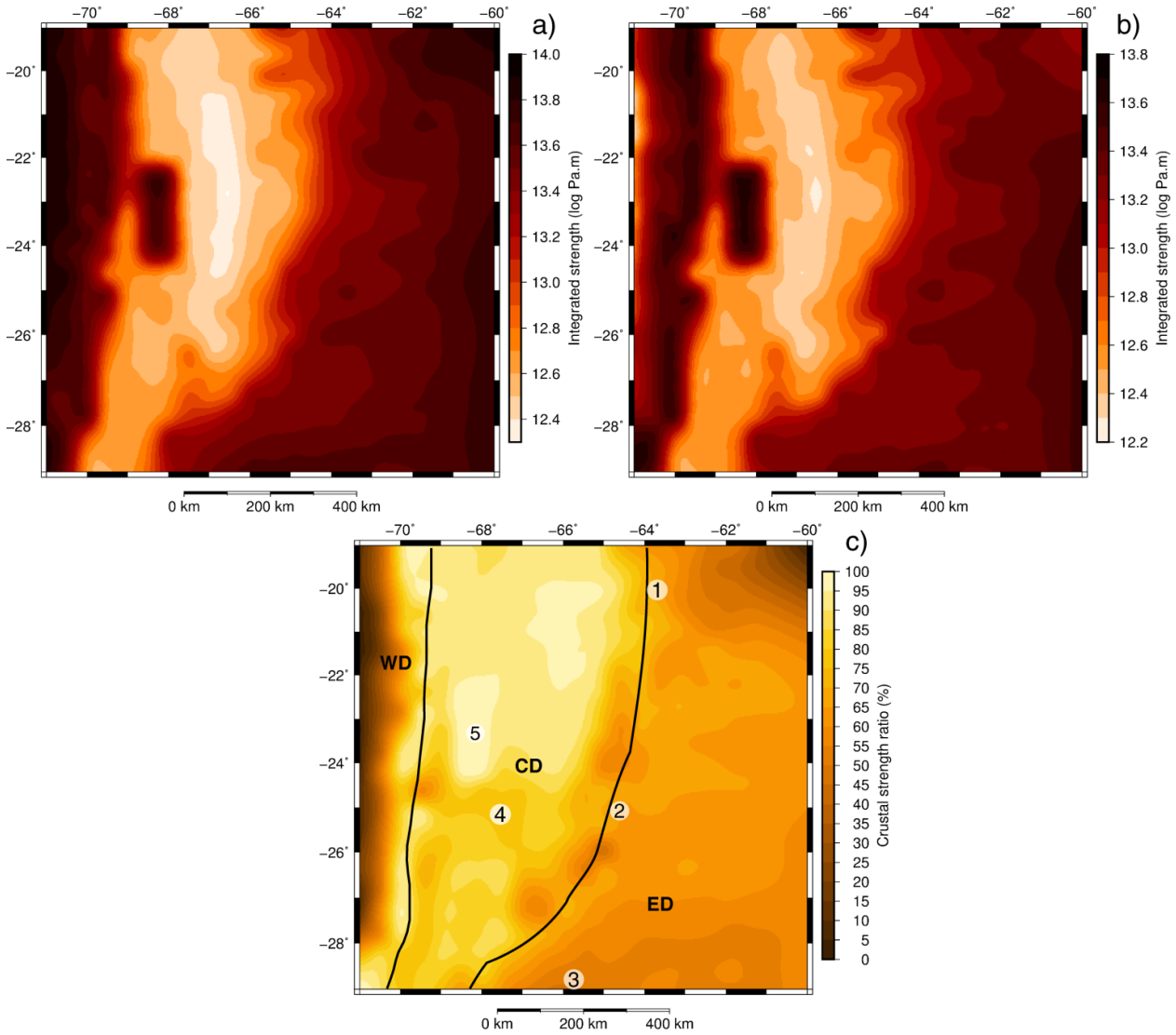

Figure 5.4: (a) Integrated lithospheric strength; (b) integrated crustal strength; (c) ratio of crustal strength to total lithosphere strength. Solid black lines in (c) outline the three main model domains and numbers 1 to 5 mark the position of the yield strength envelopes shown in Figure 5.5.

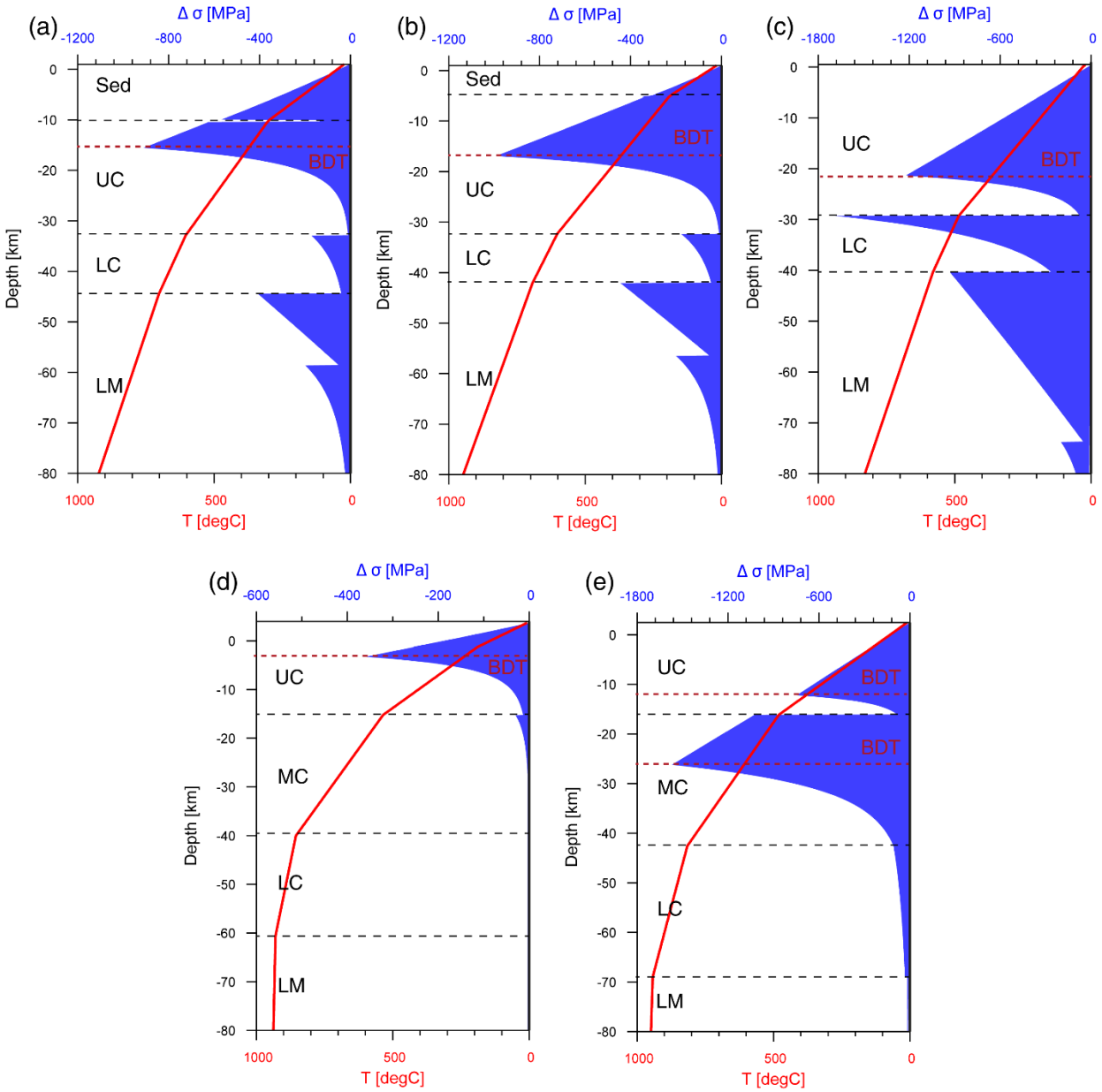

Figure 5.5: Yield strength envelopes for (a) the Subandean Ranges, (b) the Santa Barbara System, (c) the Pampean Ranges, (d) the Puna, and (e) the Atacama Block. Solid red lines show the temperature distribution with depth; dashed black lines correspond to the interface between the different units; and dashed red lines mark the brittle-ductile transition levels. Sed: sediments; UC: upper crust; MC: middle crust; LC: lower crust; LM: lithospheric mantle; BDT: brittle-ductile transition. The geographical location of the YSEs presented in (a), (b), (c), (d), and (e) is shown in Figure 5.4c with numbers 1, 2, 3, 4, and 5, respectively.

Model sensitivity was examined with respect to rock-type rheology. Different rock types were considered for the least constrained unit (lower crust in the Eastern Domain), obtaining the same trends in the crustal and lithospheric integrated strengths. With respect to the vertical distribution of strength, an increase in the strength of the lower crust from felsic granulites to mafic granulites and dry diabase is observed (See Appendix D).

5.3.2. Effective elastic thickness

Figure 5.6 shows the calculated effective elastic thickness from the 3D strength distribution in the rheological model and from the analysis of flexure in the frequency domain considering internal loads. The first observation is that T_e calculated from strength presents higher values ($\sim$15-70 km) than T_e calculated from flexure ($\sim$5-45 km). Both maps show a similar first-order trend in which the orogen is characterized by low T_e values that increase towards the foreland; however, some discrepancies arise particularly in the deformed foreland provinces and the Atacama Basin.

The T_e calculated from strength (Figure 5.6a) presents values between 10-20 km throughout the entire Altiplano-Puna plateau and most of the Western Cordillera and Eastern Cordillera. To the east, T_e increases from 20 to 30 km in the Subandean Ranges, and from 20 to 45 km in the Santa Barbara System and Pampean Ranges. Although the range of T_e in the foreland basin is broad (30-70 km), the region is characterized by T_e values between 40-55 km. In the west, there is a region beneath the Atacama Basin with high T_e values of 30-50 km.

The T_e calculated from flexure (Figure 5.6b) is very low throughout most of the region. The Chilean Precordillera, Western Cordillera, Altiplano-Puna plateau, Eastern Cordillera, and Pampean Ranges present T_e values between 3 and 20 km. The lowest T_e values (3-10 km) are located in the volcanic arc (Western Cordillera), the Chilean Precordillera, the Eastern Cordillera, and part of the southern Puna plateau. Towards east, in the Subandean Ranges, T_e rapidly increases from 15 to 40 km. In the Santa Barbara System T_e is lower, showing an average value of $\sim$15 km that increases up to 30 km in the east. The foreland basin is characterized by T_e values between 35 and 45 km.

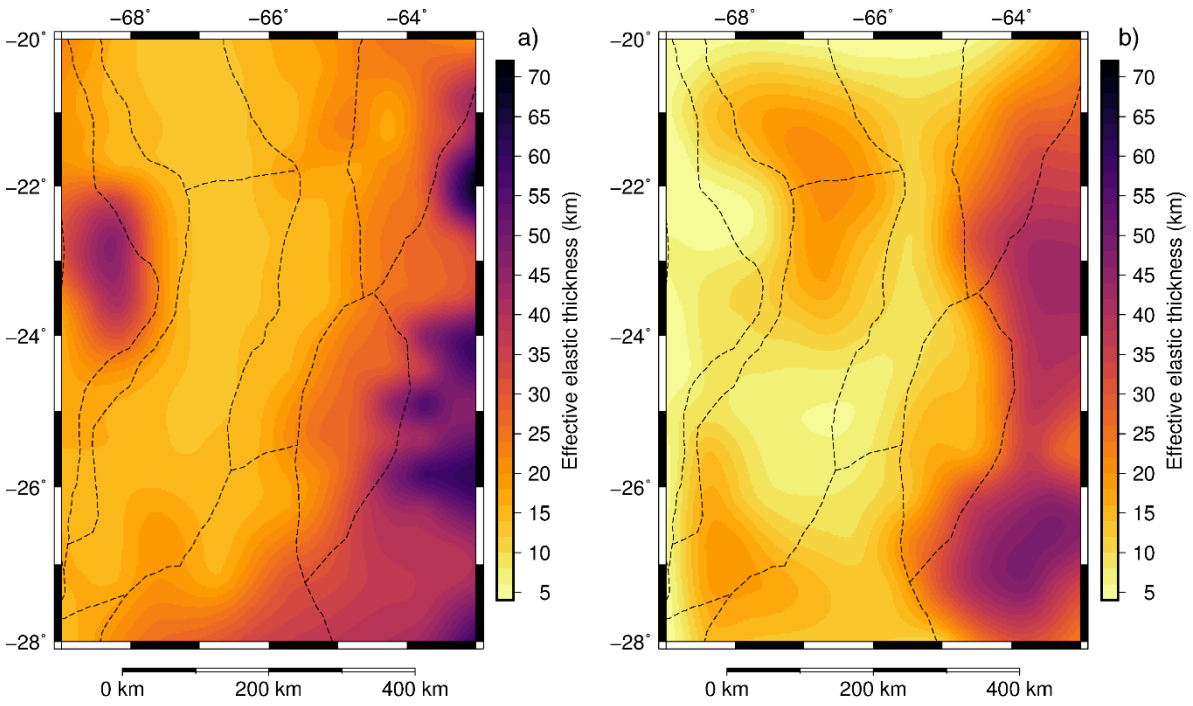

Figure 5.6: Effective elastic thickness calculated from (a) the strength distribution, and (b) the spectral analysis of flexure. Dashed black lines delineate the different morphotectonic units. Both estmations are presented for the same geographical extension using the same color scale to provide a better visual comparison.

5.2.3. Geodynamic model of the orogen-foreland system

Since the aim of the simulation was to analyze the dynamic response of the density model to present-day compression, the results presented in this section correspond to a shortening of 3.3 km (0.33 m.y. elapsed model time (emt); most closed time after 0.1-0.2 m.y.-emt). Figure 5.7 shows the distribution of the second invariant of the deviatoric strain rate, which characterizes the dynamics of changes in the internal deformation during compression. The near surface strain rate second invariant indicates that deformation is mainly localized at the eastern limit of the Subandean Ranges, the transition from the Eastern Cordillera to the Santa Barbara System, and the Pampean Ranges (Figure 5.7a).

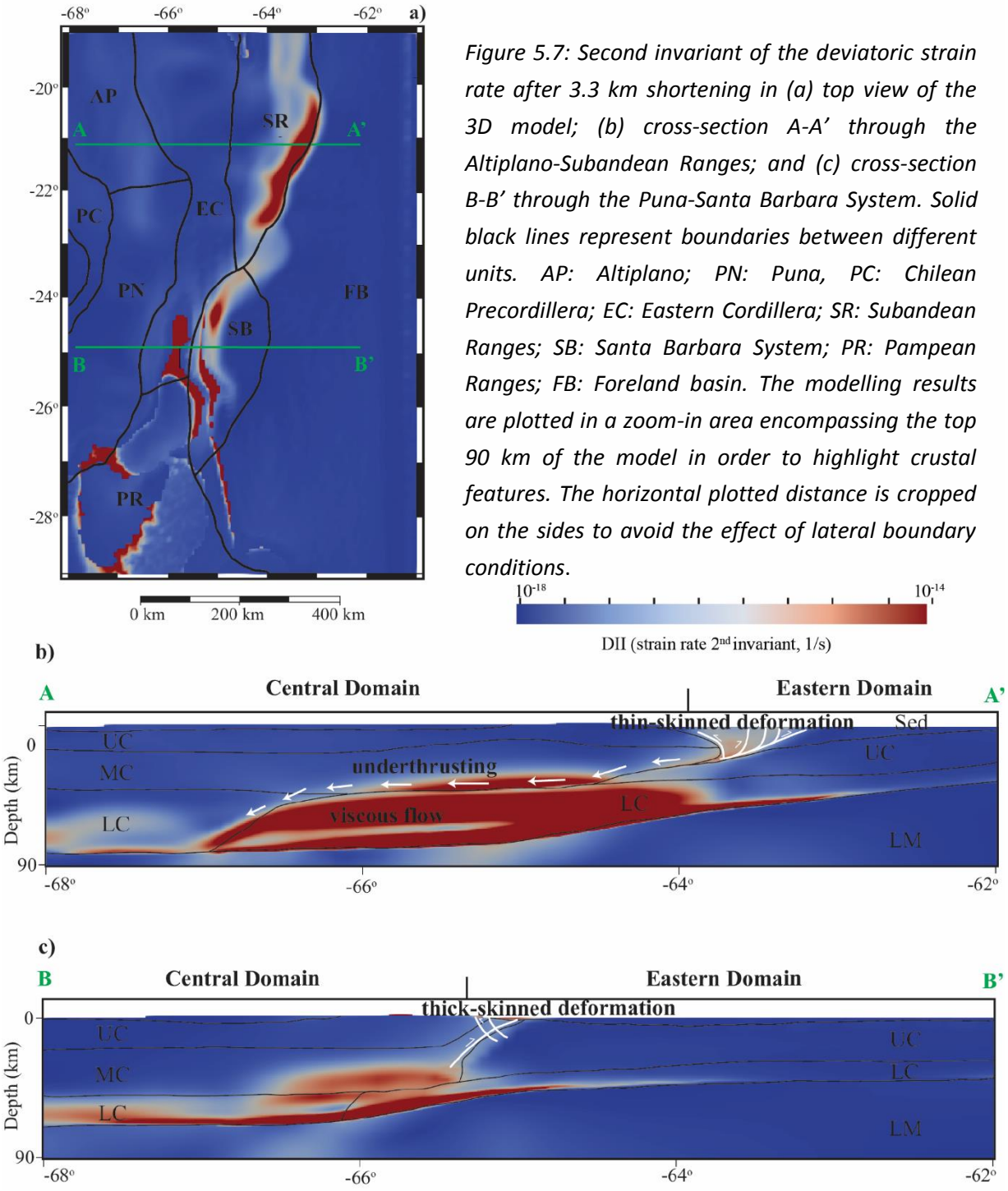

Figure 5.7: Second invariant of the deviatoric strain rate after 3.3 km shortening in (a) top view of the 3D model; (b) cross-section A-A' through the Altiplano-Subandean Ranges; and (c) cross-section B-B' through the Puna-Santa Barbara System. Solid black lines represent boundaries between different units. AP: Altiplano; PN: Puna, PC: Chilean Precordillera; EC: Eastern Cordillera; SR: Subandean Ranges; SB: Santa Barbara System; PR: Pampean Ranges; FB: Foreland basin. The modelling results are plotted in a zoom-in area encompassing the top 90 km of the model in order to highlight crustal features. The horizontal plotted distance is cropped on the sides to avoid the effect of lateral boundary conditions.

The two cross-sections through the Altiplano and the Puna (Figure 5.7, b & c) show that with depth, deformation is displaced to the west, in the lower crust of the Eastern Cordillera and the eastern margin of the plateau. Deviatoric strain rate second invariants are larger in the Altiplano cross-section, with a broader deformation zone in the lower crust, and deformation of the sedimentary cover. Interestingly, in both cross-sections the crustal thickening due to the tectonic shortening occurs along the eastern edge of the plateau rather than inside the weak plateau crust.

5.4. Discussion

The strength configuration of the lithosphere strongly depends on the temperature distribution whose validity was discussed in the previous chapter. The other controlling parameters are the background strain rate and the lithology-dependent mechanical rock properties. A uniform strain rate was considered for the entire modelling region although observations suggest a reduction of the present-day strain rate from north to south, and strain localization along the edges of the orogen (Gerbault et al., 2003; Schemmann, 2007). Since one of the main goals of the dissertation is to assess the long-term strength variations resulting from thermal and compositional heterogeneity, the application of a spatially invariant strain rate allows to isolate the effect of those heterogeneities on the lithospheric strength distribution. In that respect, the implementation of different mechanical rock properties on the basis of the prevailing lithology of the model units permitted to incorporate the effect of compositional heterogeneities into the results.

The low integrated strength levels in the crust and lithosphere of the Central Domain (Figure 5.4, a & b) and the vertical distribution of the yield strength beneath the plateau (Figure 5.5d) suggest a significantly weakened lithosphere within the orogen, particularly beneath the Altiplano-Puna plateau, where the upper crust is the only strong layer. In the Eastern Domain, the Western Domains, and the Atacama Block the integrated strength is larger and the yield strength envelopes indicate a stronger lower crust and/or mantle (Figure 5.4, a & b, and Figure 5.5, a, b, c & e). These results suggest a clear first-order spatial correlation between thermal field and rheology: regions with high temperatures coincide with regions of low integrated strengths.

The effect of rock-type rheology on strength is less evident but is still discernable. Figures 4.5, 5.4 and 5.5 illustrate that although the crust in the Atacama Block presents higher temperatures than the foreland (Figure 4.5), the crustal integrated strength is higher in the former than in the latter (Figure 5.4b). The yield strength envelopes also show a considerably stronger crust in the Atacama Block (Figure 5.5e) than in any of the morphotectonic units in the deformed foreland (Figure 5.5, a, b & c). This lack of correlation between thermal field and crustal integrated strength can be explained by the different rock-type rheology of the units and the different crustal thicknesses. The mafic rocks in the Atacama Block are stronger than the rocks in the foreland (as shown in Appendix B), and have a high yield strengths even at high temperatures (Figure 5.5e).

The relevance of temperature in strength models and the second-order effect of composition have been shown by other authors. For example, the global models of Tesauro et al. (2013) show that the distribution of integrated strength correlates with the distribution of temperature at the lower boundary condition and that the modification of rock properties does not largely alter this correlation. Afonso and Ranalli (2004) explored this interactions more deeply by analyzing the ratio of lower crustal to mantle strength in synthetic models with varying crustal thickness, heat-flow, and composition. Their results indicated that strength resides in the crust for high heat-flow values, and in the mantle for low heat-flow values, irrespective of composition and crustal thickness. These two parameters had a stronger effect for intermediate heat-flow.

In view of the observed clear dependence of strength on temperature and the strong control of crustal thickness and radiogenic heat production on the thermal field (Chapter 4), it is suggested here that, in the Central Andes, the crust (its thickness and composition) exerts a first-order control on the thermal field, and consequently also on the strength distribution. This is to some extent in agreement with the results obtained by McKenzie et al. (2005), who modelled the thermal structure of oceanic and continental lithospheres and suggested that Moho temperatures beneath the continents are primarily dependent on the thickness of the crust and its radiogenic heat production.

With regards to the distribution of second invariants of the deviatoric strain rate in the model (Figure 5.7), the concentration of high values in the lower crust beneath the Eastern Cordillera and the eastern margin of the plateau, particularly in the transect across the Altiplano and the Subandean Ranges, is consistent with previous 2D and 3D models suggesting underthrusting of the strong mafic foreland beneath the weak orogenic crust and viscous flow of lower crustal material (Hindle et al., 2005; Sobolev and Babeyko, 2005; Sobolev et al., 2006; Yang and Liu, 2003). However, the most interesting observation is that regions with high modelled second invariants of the deviatoric strain rate in the shallow crust are spatially coincident with the location of high horizontal gradients of modelled strength (Figure 5.8). Considering that the results of the rheological model indicate a strong control of crustal heterogeneities in the Central Andes on the variations of strength, it is likely that the predicted strong strain localization may also be governed by the presence of lateral heterogeneities. A similar finding is that of Cacace et al. (2008), who used a finite element viscous thin sheet model to investigate the influence of contrasting rheological structures on deformation and stresses in the Central European Basin System. Their results showed strong strain localization and deviations in the direction of the principal stress axes along lateral heterogeneities.

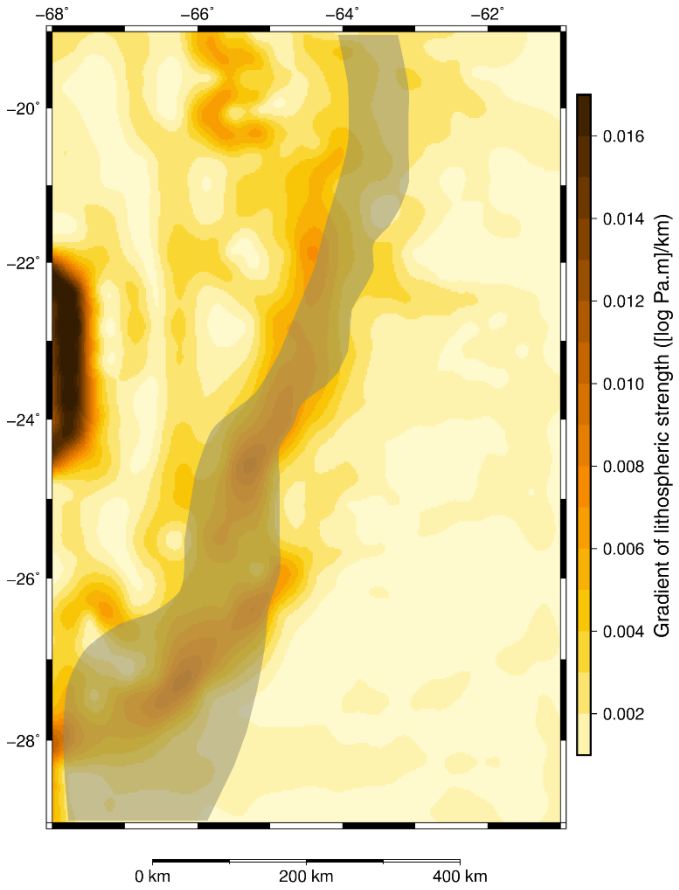

Figure 5.8: Total horizontal gradient of the modelled integrated lithospheric strenth for the orogen-foreland system. The grey shaded area shows the location of the highest modelled second invariants of the deviatoric strain rate near the surface of the geodynamic model (Figure 5.7a).

With respects to the vertical distribution of strength, the yield strength envelopes in Figure 5.5 indicate significant heterogeneities, not only between the orogen and the foreland, but also within the latter. The most characteristic feature is that the orogen and foreland present *crème brûlée* and *jelly sandwich* types of lithosphere, respectively, with brittle-ductile transitions deepening from the orogen towards the foreland. The results suggest that the rheological stratification of the lithosphere in the Central Andes is governed by the temperature distribution; *jelly sandwich* lithospheric profiles are associated with lower temperatures than *crème brûlée* lithospheric profiles (Figures 5.3 and 4.5). Even though generally *crème brûlée* profiles are representative of weak lithosphere, in the Atacama Block this type of profile is correlated with high integrated strengths because of the strong mafic rocks present in the crust.

Although the presented YSEs are representative of each morphotectonic unit, it is worth mentioning that they vary laterally, particularly in the Subandean Ranges, the Santa Barbara System, and the Pampean Ranges where large gradients of temperature occur (Figure 4.5). Since ductile strength is strongly controlled by temperature and in these morphotectonic units temperature increases from east to west, the strength in the lower crust and mantle is progressively reduced towards the orogen, and the brittle-ductile transitions in the upper crust deepen towards east. It has been suggested that the variations in the yield strength profiles and the depth to the brittle-ductile transitions have an effect on the depth distribution of seismic activity (e.g., Doser and Kanamori, 1986; Lamontagne and Ranalli, 1996), however this topic will be discussed in the next chapter.

There is disagreement among the literature on how representative these two types of rheological profiles are of the physical state of the lithosphere. Jackson (2002) claimed that the *crème brûlée* model represents better the behavior of all lithospheres because no intraplate seismicity is observed in the upper mantle, suggesting that the latter is in fact ductile and weak. Burov (2010) challenged this view stressing that a ductile mantle can be strong, and that the occurrence of seismicity is controlled not only by the strength of the rocks, but also by the stress state. Furthermore, this author suggested that *crème brûlée* profiles of the lithosphere are dynamically unstable, particularly in orogenic regions, where a collapse of the system takes place after a few m.y. in geodynamic simulations.

The results of the models presented in this chapter agree with Burov (2010) in his observation that the mantle can be strong and ductile at the same time, presenting a *jelly sandwich* lithospheric profile (as in the foreland); however, with respect to the requirement of a strong mantle for large orogenic regions to be stable, recent research has shown that this is not necessarily true. Li et al. (2016) carried out a systematic numerical study on orogens to analyze the conditions for the initiation of lithosphere delamination, finding that lithospheres with weak upper mantle and lower crust (*crème brûlée* profile) are prone to delamination processes and development of stable wide plateaus. This result is a good approximation to the Central Andes, where geochemical, geophysical, and geological studies point to the occurrence of delamination processes over the past 10-20 m.y., coetaneous with the formation of the Altiplano-Puna plateau

(e.g., Beck and Zandt, 2002; DeCelles et al., 2015; Kay et al., 1994). Furthermore, recent 2D and 3D geodynamic models for the Altiplano-Puna plateau have shown that the presence of laterally varying strength profiles, with a weak mantle in the orogen and a strong mantle in the foreland, is an important factor driving plateau formation and development of heterogeneous deformation systems as observed in the field (Liu, 2020).

The effective elastic thickness calculated from strength (Figure 5.6a) correlates with the integrated strength configuration (Figure 5.4, a & b), as expected. The orogen presents the lowest T_e values, associated with a weak and hot lithosphere whose strength resides in the upper crust (Figure 5.5d). The largest T_e values in the foreland (up to 70 km), consistent with a high integrated strength and low temperature, indicate that in those regions the crust is coupled to the mantle as in the southern Pampean Ranges (Figure 5.5c). Low T_e values generally correspond to *crème brûlée* lithospheric profiles, while high T_e values correspond to *jelly sandwich* profiles, however, the Atacama Block represents an exception, exhibiting high T_e and a *crème brûlée* lithospheric profile.

A similar trend is observed in the effective elastic thickness calculated from flexure, although some differences arise. Within the plateau, T_e is very low in the southern Puna and the volcanic arc, increasing towards the northern Puna and the Altiplano. Since T_e estimates have been usually correlated to the thermal state of the lithosphere (e.g., Hyndman et al., 2009), this heterogeneity could be interpreted as a difference in the thermal field of the plateau. In this regard, a partial spatial coincidence is observed between the low T_e anomalies in the plateau and the shallow depths to the Curie isotherm (Figure 4.7a). However, T_e increases towards the northern end of the southern Puna, in disagreement with the isotherm and the surface heat-flow (Figure 4.7). This lack of correlation may be due to a shift in the position of the windows used to calculate T_e and the depth to the bottom of the magnetic layer. Furthermore, considering that the region in the northern Puna and the Altiplano presented the largest misfits between the observed and modelled deflections during T_e calculation, any interpretation should be taken carefully.

Towards the deformed foreland, the Santa Barbara System presents low T_e compared to the Subandean Ranges. The temperature distribution (Figure 4.5) does not show any significant variations between both morphotectonic units suggesting that the thermal state is not in the origin of the observed heterogeneity. One possible scenario is that the reduced T_e of the Santa Barbara System is actually inherited. Previous studies have suggested that given the long time scales at which the lithosphere is effectively elastic, the T_e acquired in the last tectonic event slowly changes with time, so that foreland basins developed on stretched crust would present low T_e values (Desegaulx et al., 1991; Lin and Watts, 2002; Watts, 1988; Watts and Burov, 2003). The Santa Barbara System is an inverted Late Cretaceous-Paleocene rift system (e.g., Kley et al., 2005), thus, it is likely that the present-day low T_e values were acquired during the rift stage. The low effective elastic thickness in the Atacama Block could have a similar origin, however, it is most likely that the large window size of the model (160 km) hinders the isolation of the signal of the block.

After comparing the distribution of effective elastic thickness calculated with both methods against the modelled thermal field, it can be concluded that the T_e calculated from strength distribution keeps a close correlation with temperature, however, the T_e calculated from flexure only correlates with the first-order trends of the thermal field. Considering the lack of consistency between both methods, the distribution of T_e will not be used here to make further inferences on the strength of the Central Andes and its relation to active deformation processes.

5.5. Summary and conclusions

The 3D strength distribution of the Central Andes was modelled on the basis of the 3D data-derived density model and the 3D conductive thermal field. The effective elastic thickness was calculated from the modelled strength and the analysis of flexure in the frequency domain considering the internal loads of the density model. Furthermore, a geodynamic simulation for intraplate compression of the orogen-foreland system was performed using the density model as initial geometry, the same mechanical properties as the rheological model, and an initial thermal state representative of the conductive thermal model. The main outcomes are:

1. the integrated strength of the Andean lithosphere is mainly controlled by its temperature distribution, with the hot orogenic lithosphere having a lower integrated strength than the cooler forearc and foreland areas;
2. rock composition exerts a second-order control on the modelled strength in the Central Andes, explaining the lack of correlation between thermal field and strength in regions like the Atacama Block;
3. regions with high modelled second invariants of the deviatoric strain rate in the shallow crust correlate with the location of high horizontal gradients of modelled strength. Given that the variations in the thickness and composition of the crust govern the temperature distribution, which in turns controls the strength of the lithosphere, the results suggest that the heterogeneous nature of the Central Andean crust may be at the origin of the predicted strong strain localization;
4. the rheological stratification of the lithosphere is governed by its thermal state because of the strong dependence of ductile creep on temperature. Consequently, the orogen and foreland are characterized by *crème brûlée* and *jelly sandwich* lithospheric profiles, respectively;

5. despite the differences in the effective elastic thickness calculated with different methods, there is agreement on a general trend of low T_e in the orogen and high T_e in the foreland. Even though there is a first-order correlation between effective elastic thickness and thermal field, deviations suggest that other parameters need to be explored for further interpretations.

Chapter 6. Discussion. The thermo-rheological state of the Central Andes and its relationship to seismicity and active deformation

In this chapter, a final discussion is presented that integrates the results of the previous sections and analyzes their relation to active deformation processes in the Central Andes. For that, data on crustal seismic activity and neotectonic structures was compiled from the EHB-ISC Bulletin (Engdahl et al., 1998; International Seismological Centre, 2020; Weston et al., 2018), data publications of the local temporary seismic network PUDEL (Heit et al., 2007; Mulcahy et al., 2014), and the results of an international project focused on active deformation in South America (Proyecto Multinacional Andino: Geociencia para las Comunidades Andinas, 2008).

Figure 6.1 shows the horizontal gradient of the integrated lithospheric strength together with the epicenters of crustal seismicity and the neotectonic structures in the region. Most of the recorded seismicity and active structures are preferentially located in areas with high modelled strength gradients, i.e. in the transitions zones between weak and strong domains. Such transitions zones correspond to the Eastern Cordillera, the Subandean Ranges, the Pampean Ranges and the Santa Barbara System in the east, and to the Chilean Precordillera in the west, where several investigations have been conducted (e.g., Arnous et al., 2020; Costa et al., 2018; García et al., 2019; Hilley & Strecker, 2005; Meigs & Nabelek, 2010; Santibáñez et al., 2019; Siame et al., 2015; Strecker et al., 1989; Weiss et al., 2015). This suggests that the strength of the crust/lithosphere may influence the location of active deformation processes, at least of those representative of brittle behavior.

Since the modelled strength distribution in the Central Andes is controlled by the heterogeneities of the crust, the high gradients of strength and the active brittle deformation processes coincide spatially with transitions in the density and seismic velocity structure of the crust. Moreover, local studies show that in the same regions the thickness of the lithosphere diminishes from the foreland to the orogen (e.g., Koptev and

Ershov, 2011; Prezzi et al., 2009; Tassara et al., 2006). Previous investigations have also reported concentrations of seismicity and active deformation in transition zones and zones of weakness: Fernández-Ibáñez and Soto (2008) investigated the crustal rheology and earthquake distribution in the Gibraltar Arc and found that most of the crustal seismicity in the region occurred in domains of medium to high strength; Ito (1990) determined the regional variations of the seismic-aseismic boundary and the brittle-ductile transition zone in a region of Japan and noted that earthquakes appeared to nucleate where there were abrupt changes in the seismic-aseismic boundary, associated with variations in the thermal field; Sloan et al. (2011) analyzed earthquake depth distributions in Central Asia with respect to lithospheric thickness and suggested that crustal seismicity, and in particular seismicity in the lower crust, was focused on the transition zone from a cold, thick lithosphere to a hot, thin lithosphere. Similar global and regional research by Mooney et al. (2012) and Assumpçao et al. (2004) found that intraplate seismic activity concentrated around steep lateral gradients in lithospheric thickness, and in lithospheric thin spots. More recently, Magrin and Rossi (2020) found that most of the seismic events in the northern tip of the Adria microplate occur in the front of the Southern Alps facing south, where there is a sharp transition from high to low values of seismic velocity, density, rigidity and Young's modulus.

These observations are consistent with the results of the previous chapter that suggested a possible control of lateral rheological heterogeneities on the strong strain localization in the shallow crust. Moreover, the predicted high second invariants of the deviatoric strain rate in the shallow upper crust correlate with the location of observed brittle deformation in the form of recorded seismicity and mapped active structures, supporting the hypothesis of the relevance of crustal heterogeneities in the Central Andes. It is interesting to note that the location of deformation does not correlate with the proposed terrane boundaries as would be expected if large scale shear zones due to inter-terrane movements were present.

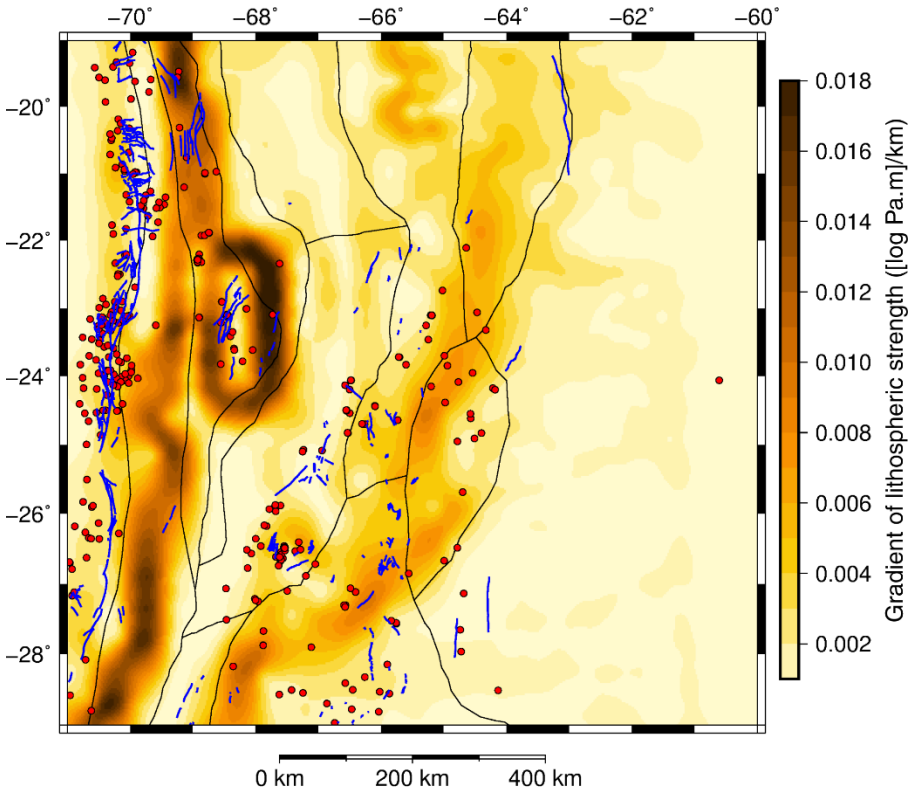

Figure 6.1: Horizontal gradient of the integrated lithospheric strength, together with the location of active faults (solid blue lines) and epicenters of crustal seismic events (red circles). Solid black lines outline the morphotectonic units.

The observed localization of active deformation could also be related to lateral variations of gravitational potential energy (GPE) as suggested for other regions (e.g., Fernández-Ibáñez and Soto, 2008). The GPE of a mountain range grows with the square of both its average elevation and the thickness of its crustal root (Stüwe, 2007). As a result, the forces required to produce further vertical growth increase exponentially, preventing any internal deformation (e.g., Molnar and Lyon-Caen, 1988). Regions with high GPE exert a net force on those with low GPE, imposing a compressional stress field on the transition zone (e.g., Stüwe, 2007). In such scenario, the high GPE stored in the plateau (due to its thick crust and high elevation) would prevent internal deformation and impose a compressional stress field on its margins, forcing lateral, foreland-ward growth, instead of continued vertical growth (e.g., Molnar and Lyon-Caen, 1988). Local and global estimations of GPE and its contribution to the horizontal deviatoric stress field show indeed that the Central Andean orogen is characterized by high GPE compared to the

foreland and forearc areas, resulting in extensional deviatoric stresses within the orogen interior, and compressive deviatoric stresses on its margins (e.g., Flesch and Kreemer, 2010; Ghosh et al., 2009).

On another note, the observed localization of active deformation along high strength gradients could influence the position of the volcanic arc as well. Although the position of volcanic arcs in subduction systems is known to be controlled by the dehydration of the subducting slab at approximately 100 km depth (Tatsumi, 1986), the marked diversion of the volcanic arc (i.e. the Western Cordillera) towards the east, around the Atacama Block, is not associated with any change in the dip of the slab. Since the volcanic arc lies approximately along the boundary between the strong crust in the forearc and the weak crust in the orogen (Figure 6.1), the ascent of magma in this zone may have been facilitated due to a localized opening of fractured pathways, thus causing the diversion of the volcanic arc.

The seismic activity in the Coastal Cordillera and the Puna does not show any clear correlation with the high strength gradients. Most of the seismicity in the Coastal Cordillera is restricted to the area near the interface between the subducting slab and the upper plate (e.g., Allmendinger & González, 2009; Bloch et al., 2014; Figure 6.2). The Puna plateau presents a complex and areally extensive deformation system that has contributed to its Late Cenozoic uplift history (e.g., DeCelles et al., 2015b; Pingel et al., 2020), with N-S striking reverse faults and folds (e.g., Montero-López et al., 2020), WNW-ESE striking left-lateral transtensional fault systems, NE-SW striking right-lateral transpressive fault systems (e.g.; Norini et al., 2013; Riller et al., 2001; Zhou & Schoenbohm, 2015), and superposed normal faulting (e.g., Allmendinger et al., 1989; Montero López et al., 2014). Riller et al. (2012) have shown by means of analogue modelling that a N-S transition from weak to strong crust can produce broad and complex deformation systems as those reported for the Puna. The results of the rheological model support the existence of such N-S variations in the strength of the crust within the Central Andes, from a weak crust beneath the Puna plateau to a strong crust beneath the Pampean Ranges (Figure 5.4).

On the basis of the registered volcanic activity of the Puna and the results of seismic studies, it has been suggested that the widespread extensional processes observed within the plateau are possibly associated with gravitational collapse during the last m.y. of tectonic evolution of the plateau, accompanied by delamination of the lithospheric mantle approximately 7 Ma (e.g., Allmendinger, 1986; Beck et al., 2015; Daxberger and Riller, 2015; Drew et al., 2009; Montero Lopez et al., 2010; Murray et al., 2015; Schoenbohm and Strecker, 2009). In this line, Calixto et al. (2013) reported a complex pattern of low and high seismic velocities in the mantle, which they interpreted as delaminated blocks (high velocity) and hot asthenospheric material (low velocity). The modelled average density of the crust presented in Chapter 3 shows semi-circular low-density anomalies in the Puna (Figure 3.6) that could represent regions where delamination of the lower crust occurred.

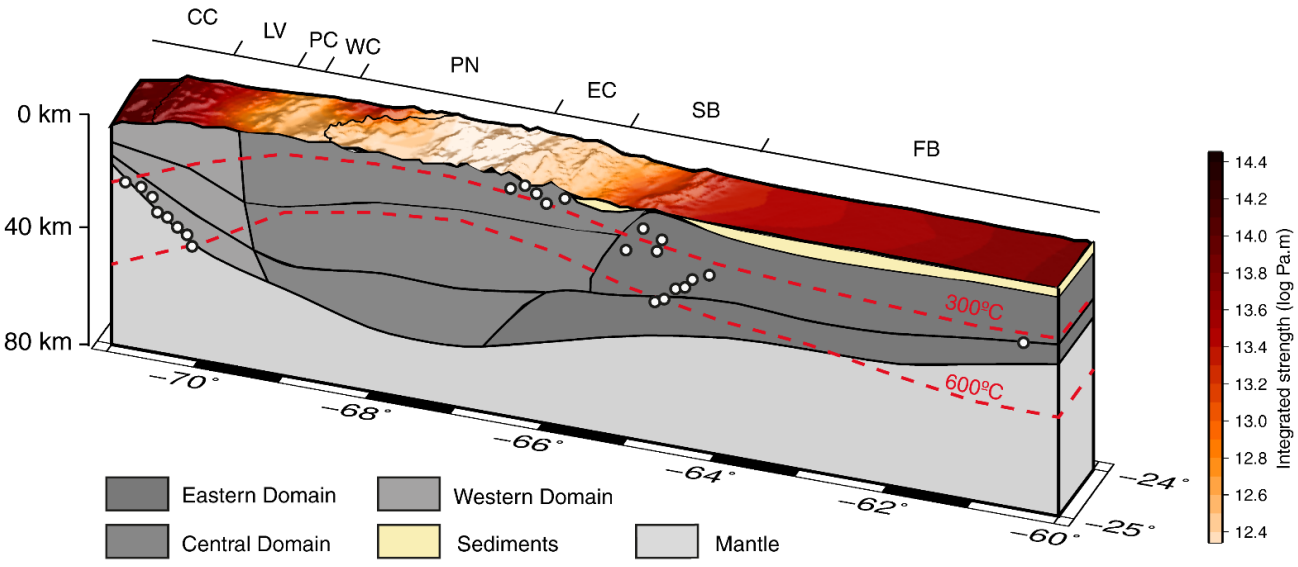

Figure 6.2: 3D vertical slice of the density model between 24°S and 25°S, showing the position of the 300°C and 600°C modelled isotherms (dashed red lines) and the integrated strength of the lithosphere (overlain on the topography). White circles with black rims represent the hypocenters in the region. The transitions between morphotectonic units are marked on the top of the diagram.

Some of the early investigations into the distribution of seismicity with depth suggested that brittle failure was restricted to depths above the 600°C isotherm in the mantle and the 300°C-450°C isotherms in the crust because, as a first approximation, mantle rheology is governed by the rheology of olivine and crustal rheology is governed by the rheology of quartz or plagioclase (e.g., Chen and Molnar, 1983; McKenzie et al., 2005). However, deep crustal seismic activity has been registered within the studied area, well below the modelled depths of the 300°C-450°C isotherms, being the 600°C isotherm the apparent boundary (Figures 6.2 and 6.3). Similar observations from different tectonic settings in western North America, the Dead Sea basin, the East African and Baikal rift systems, the Tien Shan foreland, and the northern Alpine foreland of Switzerland, challenged the early ideas and called for a more thorough investigation on both the seismic process and the rheological stratification of the lithosphere (Aldersons et al., 2003; Bryant and Jones, 1992; Camelbeek and Iranga, 1996; Deichmann, 1992; Déverchère et al., 2001; Nyblade and Langston, 1995; Sloan et al., 2011; Wong and Chapman, 1990).

A number of authors have found a good correlation between the location of brittle-ductile transitions (BDTs) and various proxies for the depth-frequency distribution of hypocenters, based on the establishment of rheological profiles of the lithosphere (e.g., Albaric et al., 2009; Chen & Molnar, 1983; Doser & Kanamori, 1986; Fernández-Ibáñez and Soto, 2008; Meissner & Strehlau, 1982; Sibson, 1982). Following those studies, the depth proxies used here to compare against the depth of the modelled BDTs are the depth at which the frequency of hypocenters starts to decrease (D_{dec}), the maximum depth of the hypocenters - equivalent to T_S – (D_{max}), and the depths above which 80% and 95% of the earthquakes occur (D_{80} and D_{95}, respectively).

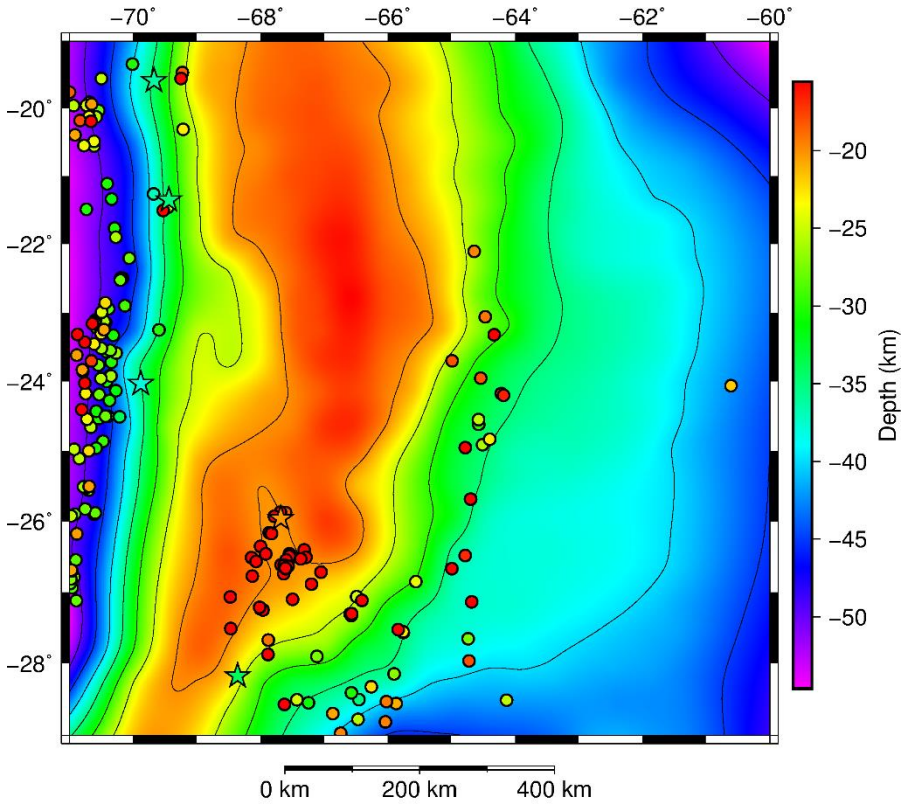

Figure 6.3: Modelled depth to the 600°C isotherm together with the distribution of hypocenters in the Central Andes (color-coded dots and stars). The same color scale is used for the depth of the isotherm and hypocenters. Dots and stars represent hypocenters that are shallower and deeper than the 600°C, respectively.

In order to test the different proposed hypotheses concerning how the configuration of the seismogenic layer relates to the modelled brittle-ductile transitions in the Central Andes, only hypocenters with less than 5 km of vertical uncertainty were selected and used to plot depth-frequency distribution histograms. These were constructed for the morphotectonic units presenting most of the seismic activity (Pampean Ranges, Santa Barbara System and Puna plateau; Figure 6.4). The depth distribution of seismicity in the Coastal Cordillera and surrounding areas was not analyzed because most of the seismic activity there occurs at the interface between the upper plate and the subducting slab (Figure 6.2), responding to different processes than those of intraplate seismicity.

The modelled BDTs in the crust beneath the Puna plateau, the Santa Barbara System and the Pampean Ranges lie at depths of 7-8 km, 16-17 km, and 21-22 km, respectively, being shallower than D_{dec}, D_{max}, D_{80} and D_{95} in each of the corresponding morphotectonic units (Figure 6.4). However, they follow the same trend as the hypocenter depth-frequency distributions, with greater depths towards the Pampean Ranges. Moreover, the discrepancies between the modelled depth of the BDTs and D_{dec} are between 1 and 5 km, which is within the uncertainty range for the depth of the hypocenters. Interestingly, D_{max} correlates with the upper crust-lower crust interface in the Santa Barbara System, and with the Moho in the Pampean Ranges.

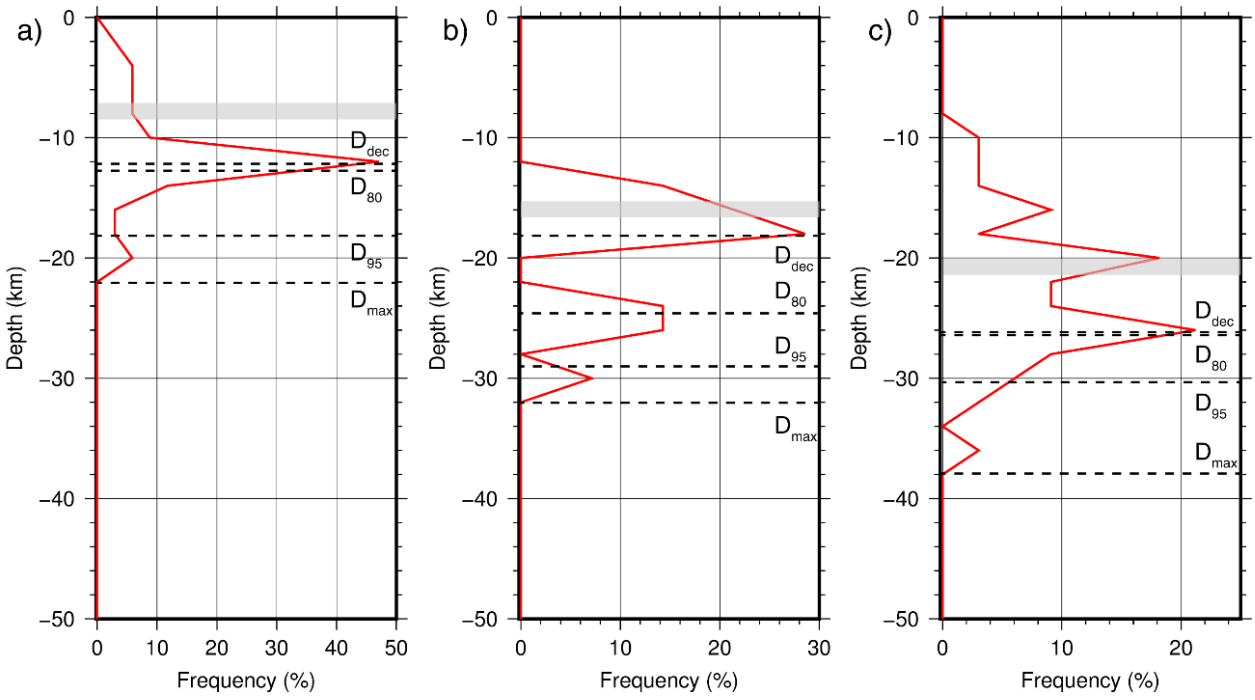

Figure 6.4: Depth-frequency distribution of hypocenters in (a) the Puna, (b) the Santa Barbara System, and (c) the Pampean Ranges. Dashed black lines show the position of different depth proxies for comparison with modelled brittle-ductile transitions (grey shaded blocks). D_{dec}: depth below which the frequency of hypocenters decreases; D_{80}: depth above which 80 % of the hypocenters occur; D_{95}: depth above which 95 % of the hypocenters occur; D_{max}: depth below which no hypocenters occur.

As observed in Figure 6.4, a proportion of earthquake hypocenters lie within the ductile regime, beneath the modelled brittle-ductile transitions. The occurrence of earthquakes below these transitions has been explained as being due to the propagation of aftershocks, or the presence of heterogeneities with strong lithologies that remain brittle (e.g., Fernández-Ibáñez and Soto, 2008; Sloan et al., 2011). Likewise, the recent mafic volcanism in the Puna, the Famatinian Ordovician magmatism in the Pampean Ranges, and the mafic extrusions from the Salta Rift in the Santa Barbara System (e.g., Drew et al., 2009; Rapela et al., 2018; Viramonte et al., 1999) may have left behind strong mafic residual rocks in the crust that could act as focal points for the initiation of seismic slip (e.g., the sensitivity analysis presented in Appendix D shows that brittle behavior is modelled for the lower crust of the Pampean Ranges when a diabase rheology is considered).

From a different perspective, research on the processes of earthquake generation has shown that brittle failure can occur in ductile shear zones, where processes such as grain-size reduction, shear heating, chemical alteration, dynamic recrystallization and phase changing weaken the rocks. Laboratory studies and models show that these processes can lower the strength of rocks and modify the slip behavior, favoring the occurrence of failure in the ductile regime (e.g., Bos and Spiers, 2002; Handy and Brun, 2004; Hobbs et al., 1986). Particularly in the Santa Barbara System and the Pampean Ranges, where there has been repeated reactivation of deep crustal structures (e.g.; Kley and Monaldi, 2002; Ramos et al., 2002; Strecker et al., 1989), the development of shear zones could explain the observed deep seismicity. As observed in Figure 6.2, some of the hypocenters within the Eastern Domain appear to lie on a west-dipping plane that could in fact represent a former extensional shear zone inherited from the Late Cretaceous Salta Rift (e.g.; Grier et al., 1991; Kley et al., 2005). Friction within such shear zones would be reduced, facilitating seismic slip (Petley-Ragan et al., 2019; Prieto et al., 2017).

In order to evaluate the influence of possible shear zones on the vertical distribution of strength, Figure 6.5 shows yield strength envelopes for the Santa Barbara System and the Pampean Ranges considering a reduction in the friction coefficient within the crust

from 0.75 to 0.2, as reported for natural fault systems (e.g., Zoback et al., 1987). As observed in the YSEs, a reduced friction coefficient in the Pampean Ranges results in deeper brittle-ductile transitions and an extensive brittle zone within the lower crust (Figure 6.5b), however, no major changes occur in the Santa Barbara System, where the lower crust remains ductile (Figure 6.5a). Only when the presence of mafic compositional heterogeneities is considered together with the reduction of friction, the lower crust of the Santa Barbara exhibits brittle behavior (Figure 6.5c).

The possible existence of localized compositional heterogeneities and/or shear zones is not resolved in the models presented in this dissertation because of their regional character and coarse resolution. However, it is interesting to note that the results of the employed modelling approach, when based on a well-constrained 3D geological model, correlate surprisingly well with the location of recent deformation and the general depth distribution of observed seismicity.

So far, only the earthquake distribution within the crust was discussed. With regards to the mantle, the only seismic activity within the modelling region is located in the subducting Nazca plate or in the mantle wedge close to the subduction plane. However, some earthquakes in the Pampean Ranges occur close to the Moho, and, taking into consideration the uncertainty in the vertical positions of hypocenters and the Moho depth, the mantle could therefore possibly present some seismicity. On a global scale, the apparent lack of intraplate seismicity in the upper mantle (Maggi et al.; 2000b, 2000a), lead Jackson (2002) to suggest that the mantle is weak. However, Burov (2010) has shown by means of thermo-mechanical modelling that the mantle can be strong under both brittle and ductile regimes without exhibiting seismicity. It follows that the absence of intraplate seismicity in the upper mantle of the Central Andes can be explained by the mantle being ductile, which does not prevent it from being strong, as shown by the yield strength envelopes (e.g., Figure 5.5c) and the integrated lithospheric strength in the foreland (Figure 5.4a).

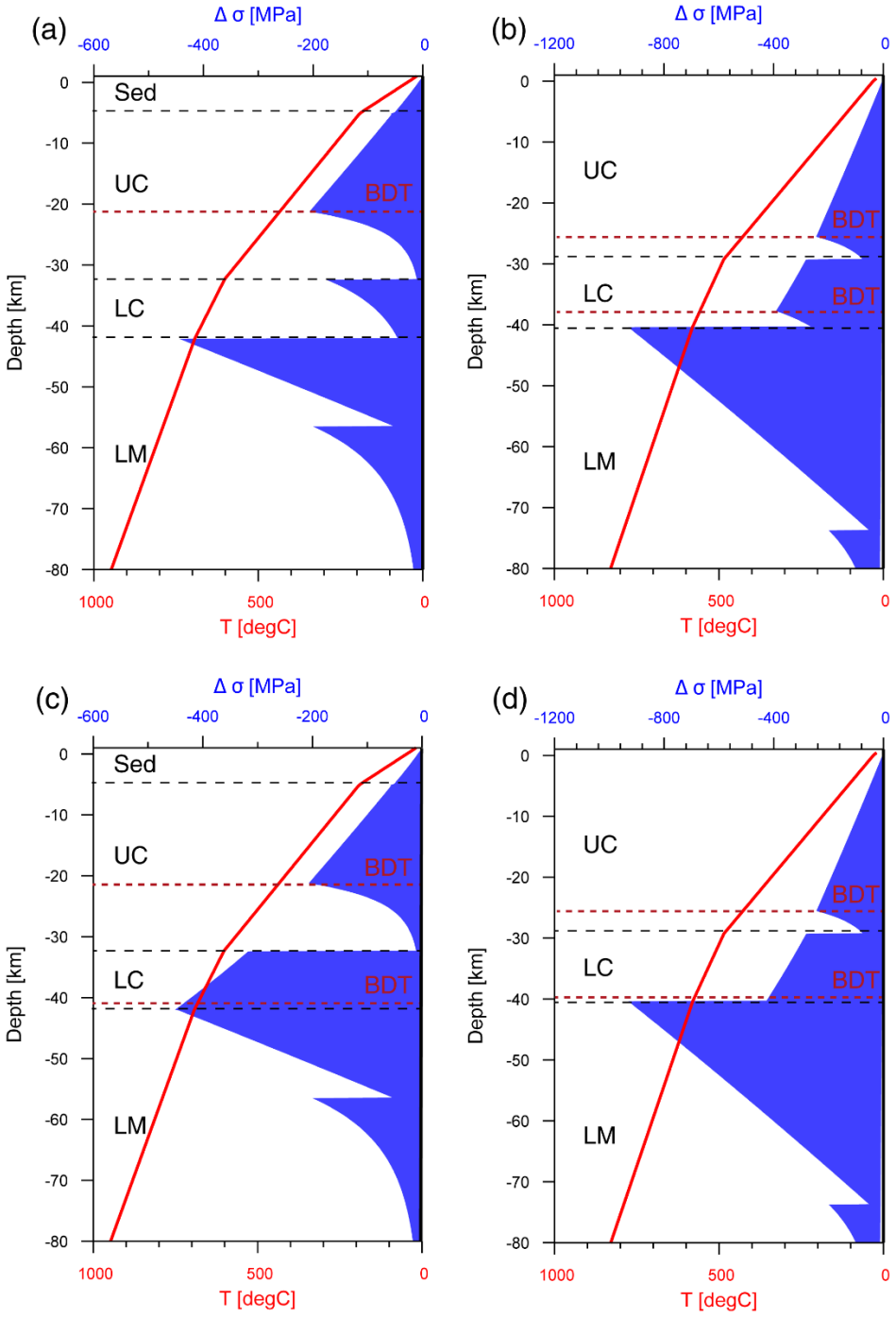

Figure 6.5: Yield strength envelopes for (a) the Santa Barbara System, and (b) the Pampean Ranges, considering a friction coefficient of 0.2 for the crust. In (c) and (d), a diabase rheology is considered (in addition to the reduction of friction) for the lower crust of the Santa Barbara System and the Pampean Ranges, respectively.

Chapter 7. Conclusions

The aim of this dissertation was to investigate the role of the heterogeneous lithospheric structure and composition of the Central Andes on its thermal field and strength distribution, and to analyze a possible control of temperature and strength on the observed active deformation processes in the form of seismic activity and neotectonic structures. In that respect, a data-based density model of the Central Andean lithosphere was constructed in which to calculate the temperature and strength distribution.

The results of the density model show that the crust is divided into three main regions corresponding to the forearc, orogen, and foreland, which are characterized by mafic, felsic, and intermediate compositions, respectively. This heterogenous crustal density distribution does not correlate with the existing models of Neoproterozoic-Cambrian terrane accretion; instead, it is coherent with the tectonic evolution of the region throughout the Phanerozoic. Considering a uniform intermediate initial composition (irrespective of the presence of different terranes), the extensive mafic magmatic activity in the location of the present-day forearc during the Jurassic could explain the reported mafic compositions, high velocity, and high density. In the present-day orogen, crustal recycling through processes of crustal thickening, melting, delamination and relamination, especially during the Early Paleozoic and the Cenozoic, could account for the observed felsic compositions, low velocity, and low density.

The modelled steady-state conductive thermal field exhibits a clear correlation with the heterogeneous nature of the crust, with higher temperatures in the thick and felsic orogenic crust than in the surrounding thinner and more mafic forearc and foreland areas. Furthermore, the observed inverse correlation between the modelled thermal field and the temperature at the lower boundary condition in the mantle suggests that, in the region, the crust exerts a major control on the deep temperature distribution. Although convective and advective processes are active in the Central Andes and thermal equilibrium has probably not yet been attained, the 3D thermal model reproduces measured surface heat-flow and shallow crustal temperature reasonably well, particularly in those regions where advective processes are less pronounced.

The modelled strength distribution is mainly governed by the thermal field, showing an inverse correlation between temperature and integrated strength. Any deviations from this correlation are explained by compositional crustal heterogeneities. Furthermore, the dynamic simulation for intraplate compression of the density model shows that the highest second invariants of the deviatoric strain rate coincide spatially with the highest strength gradients. Altogether, these results suggest that the heterogeneous nature of the crust is the main controlling factor on the strength distribution, and that it may influence the location where shortening is accommodated.

When comparing the results of the rheological and geodynamic models against the reported active deformation processes, it is observed that seismic activity and neotectonic structures occur preferentially in areas with high strength gradients and high second invariants of the deviatoric strain rate, suggesting that the models are consistent with the observations and that the heterogeneities of the crust have a strong influence on the localization of strain.

The depth distribution of hypocenters shows a correlation with the modelled strength distribution as well, with the depth at which the frequency of hypocenters starts to decrease (D_{dec}) located at the same depth level (within the range of uncertainties) of the modelled brittle-ductile transitions in the Pampean Ranges, Santa Barbara System and Puna plateau. Earthquakes occurring below the modelled brittle-ductile transitions could have originated in residual strong mafic rocks within the crust or shear zones where seismic slip is facilitated through a reduction in friction. Particularly in the Santa Barbara System, the presence of both, mafic rocks and friction reduction, is required to account for the deeper recorded seismic events.

In general, the cumulative results of the models indicate that the knowledge of the crustal structure and composition is crucial to better understand the present-day deformation of the region. Further information, especially on rock properties and temperature, could help to improve the models by considering couple thermo-hydraulic processes in the shallow upper crust and calibrating the results to measured data.

Appendix A

A Python tool (Meeßen, 2017) was used to calculate the S-wave velocity for a mantle rock with a specific composition (the average composition of mantle peridotite xenoliths; Lucassen et al., 2005) under different pressure and temperature conditions, including the effects of anharmonicity and anelasticity on seismic velocity:

$$V_s = \sqrt{\frac{\mu}{\rho}}(1 - \xi) \tag{A.1}$$

where V_s is the S-wave velocity, μ is the shear modulus, ρ is the density, and ξ is the attenuation term:

$$\xi = \frac{2}{Q \cdot tan(\pi a/2)} \tag{A.2}$$

where a is the frequency exponent, and Q is the attenuation due to anelasticity:

$$Q = A\omega^a exp\left(\frac{a(H + PV)}{RT}\right) \tag{A.3}$$

where A and R are constants, P is the pressure, T is the temperature, ω is the wave frequency, H is the activation energy, and V is the activation volume.

Shear modulus μ and density ρ for pressures up to 6 GPa can be expressed for each mineral phase as follows:

$$\rho = \rho_0 \left(1 - \alpha(T - T_0) + \frac{P - P_0}{K}\right) \tag{A.4}$$

$$M = M_0 + (T - T_0)\frac{\partial M}{\partial T} + (P - P_0)\frac{\partial M}{\partial P} \tag{A.5}$$

where K is compressibility, α is the thermal expansion coefficient, and M stands for either shear modulus μ or compressibility K. The properties $\alpha, \rho_0, M_0, \partial M/\partial T$ and $\partial M/\partial P$ for olivine, diopside and enstatite were taken from Cammarano et al. (2003), and for spinel from Goes et al. (2000). The parameters A, H and V to calculate Q were adopted from Sobolev et al. (1996). M and ρ were averaged in accordance with mineral proportion.

The Python code of Meeßen (2017) implements a look-up tables method. S-wave velocities and densities are calculated for all depths in the tomography dataset at temperatures between 300 and 3000K, in steps of 1 K, and stored in a table together with the corresponding temperatures. Depth is converted to pressure using the AK135 reference model of the Earth (Kennett et al., 1995). The appropriate temperature and density for a specific S-wave velocity at a particular depth in the tomography model are then obtained by linear interpolation of the temperatures and densities corresponding to the two closest calculated S-wave velocities in the table.

Appendix B

The secondary creep parameters were selected from published laboratory experiments on rocks with compositions representative of the modelled units. Since the properties reported for the same rock-type rheology by different authors are not always consistent, synthetic yield strength envelopes were plotted for a given reference strain rate and geotherm in order to visually examine the relative strength of the rock-types (Figure B.1). This method allowed the assignment of rock properties in a way that mafic domains are characterized by stronger rocks than felsic domains, and, within each domain, the lower crust is stronger than the upper crust (except in the Western Domain where serpentinization is proposed to occur; e.g., Prezzi et al., 2009).

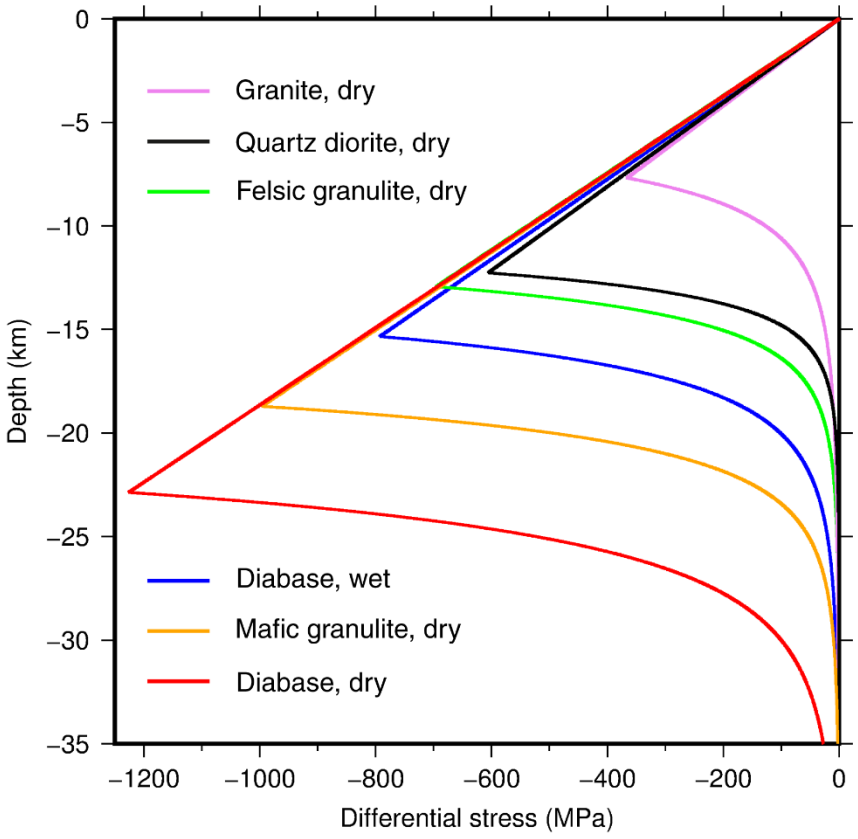

Figure B.0.1: Synthetic yield strength envelopes for the different rock-type rheology constructed using a uniform strain rate and geotherm.

Appendix C

The code LaMEM solves the coupled system of the three conservation equations of momentum (Eq. C.1), mass (Eq. C.2), and energy (Eq. C.3), with temperature, pressure and velocity as primary unknowns:

$$\frac{\partial \tau_{ij}}{\partial x_j} - \frac{\partial P}{\partial x_i} + \rho g_i = 0 \tag{C.1}$$

$$\frac{1}{K}\frac{DP}{Dt} - \alpha \frac{DT}{Dt} + \frac{\partial v_i}{\partial x_i} = 0 \tag{C.2}$$

$$\rho C_p \frac{DT}{Dt} = \frac{\partial}{\partial x_i}\left(\lambda \frac{\partial T}{\partial x_i}\right) + H \tag{C.3}$$

where i and j are coordinate indexes, x_i and x_j are spatial coordinates, ρ is density, P is pressure, K is bulk modulus, T is temperature, α is the thermal expansion coefficient, C_p is specific heat, λ is thermal conductivity, H is the volumetric heat source, D/Dt is the material time derivative, g_i is the i component of the gravity vector, v_i is the i component of the velocity vector, and $\tau_{ij} = \sigma_{ij} + P\delta_{ij} = 2\eta\dot{\varepsilon}_{ij} - P\delta_{ij}$ is the Cauchy stress deviator, with σ_{ij} being the deviatoric stress tensor, δ_{ij} the Kronecker delta (1 for $i = j$ and 0 otherwise), η the viscosity, and $\dot{\varepsilon}_{ij} = \frac{1}{2}\left(\frac{\partial v_i}{\partial x_j} + \frac{\partial v_j}{\partial x_i}\right) - \frac{1}{3}\frac{\partial v_k}{\partial x_k}\delta_{ij}$ the deviatoric strain rate tensor.

The elasto-visco-plastic constitutive equation for the deviatoric stress-strain rate is given by:

$$\dot{\varepsilon}_{ij} = \dot{\varepsilon}_{ij}^{el} + \dot{\varepsilon}_{ij}^{vs} + \dot{\varepsilon}_{ij}^{pl} = \frac{\overset{\nabla}{\tau}_{ij}}{2G} + \dot{\varepsilon}_{II}^{vs}\frac{\tau_{ij}}{\tau_{II}} + \dot{\varepsilon}_{II}^{pl}\frac{\tau_{ij}}{\tau_{II}} \tag{C.4}$$

where $\dot{\varepsilon}_{ij}^{el}$, $\dot{\varepsilon}_{ij}^{vs}$, and $\dot{\varepsilon}_{ij}^{pl}$ are the elastic, viscous, and plastic components of the deviatoric strain rate, respectively, G is the elastic shear modulus, the subscript II denotes the second invariant of the corresponding tensor (e.g. for the deviatoric strain rate $\dot{\varepsilon}_{II} = \sqrt{\frac{1}{2}\dot{\varepsilon}_{ij}\dot{\varepsilon}_{ij}}$), and $\overset{\nabla}{\tau}_{ij} = \frac{\partial \tau_{ij}}{\partial t} + \tau_{ik}\omega_{kj} - \omega_{ik}\tau_{kj}$ is the Jaumann objective stress rate, with $\omega_{ij} = \frac{1}{2}\left(\frac{\partial v_i}{\partial x_j} - \frac{\partial v_j}{\partial x_i}\right)$ being the spin tensor.

The volumetric heat source includes shear heating, controlled by the efficiency parameter $0 \leq \chi \leq 1$, and the radiogenic heat (A):

$$H = \chi\tau_{ij}\left(\dot{\varepsilon}_{ij}^{vs} + \dot{\varepsilon}_{ij}^{pl}\right) + \rho A \tag{C.5}$$

Appendix D

The sensitivity of the rheological model was tested with respect to the properties of the lower crust in the Eastern Domain. Three different rock-type rheology were considered (Table D.I), for which results are presented in integrated lithospheric strength maps (Figure D.1) and yield strength envelopes of the Subandean Ranges, Santa Barbara System, and Pampean Ranges (Figure D.2).

Table D.I: Rock properties for the lower crust in the Eastern Domain

Rock-type rheology	Power-law activation energy, $\boldsymbol{Q_p}$ (kJ mol^{-1})	Pre-exponential scaling factor, $\boldsymbol{A_p}$ (Pa^{-n} s^{-1})	Power-law exponent, $\boldsymbol{n}$
Mafic granulite, dry[1]	445	8.83E-22	4.2
Felsic granulite, dry[1]	243	2.01E-21	3.1
Diabase, dry[2]	485	5.05E-28	4.7

[1] Wilks and Carter (1990); [2] Afonso and Ranalli (2004).

The integrated lithospheric strength maps in Figure D.1 all reveal the same general trend, irrespective of the rock properties used for the lower crust in the Eastern Domain. The highest gradients of strength occur in the same regions, suggesting that the results and their correlation to the location of active deformation are robust.

Regarding the vertical distribution of strength, the yield strength envelopes in Figure D.2 show that the three morphotectonic units present a *jelly sandwich* type of lithosphere for the three different rock-types considered for the lower crust. There is an increase in strength from felsic granulite (Figure D.2, d, e & f) to mafic granulite (Figure D.2, a, b & c), and diabase (Figure D.2, g, h & i). A felsic granulite rheology for the lower crust results in decoupling between the crust and the mantle in the three morphotectonic units; the mafic granulite rheology differs only in the Pampean Ranges where the lower crust is coupled to the mantle; and the diabase rheology results in crust-mantle coupling in the three morphotectonic units.

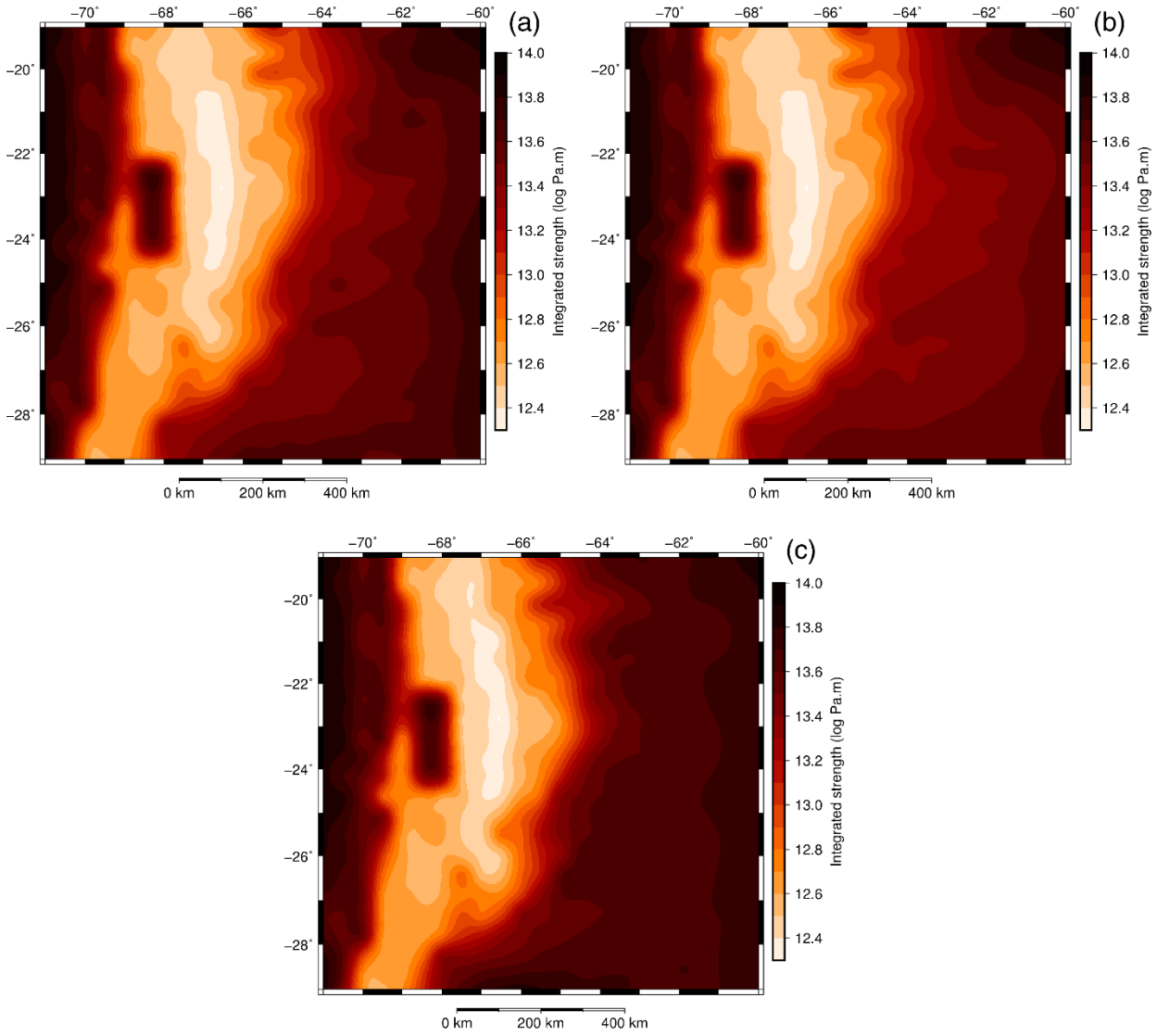

Figure D.0.1: Integrated lithospheric strength with (a) a mafic granulite, (b) a felsic granulite, and (c) a diabase rock-type rheology in the lower crust of the Eastern Domain.

Figure D.0.2: Yield strength envelopes for the Subandean Ranges, Santa Barbara System, and Pampean Ranges with mafic granulite (a, b, c, respectively), felsic granulite (d, e, f, respectively), and diabase (g, h, i, respectively) rock-type rheology for the lower crust in the Eastern Domain. Sed: Sediments; UC: upper crust; LC: lower crust; LM: lithospheric mantle; BDT: brittle-ductile transition.

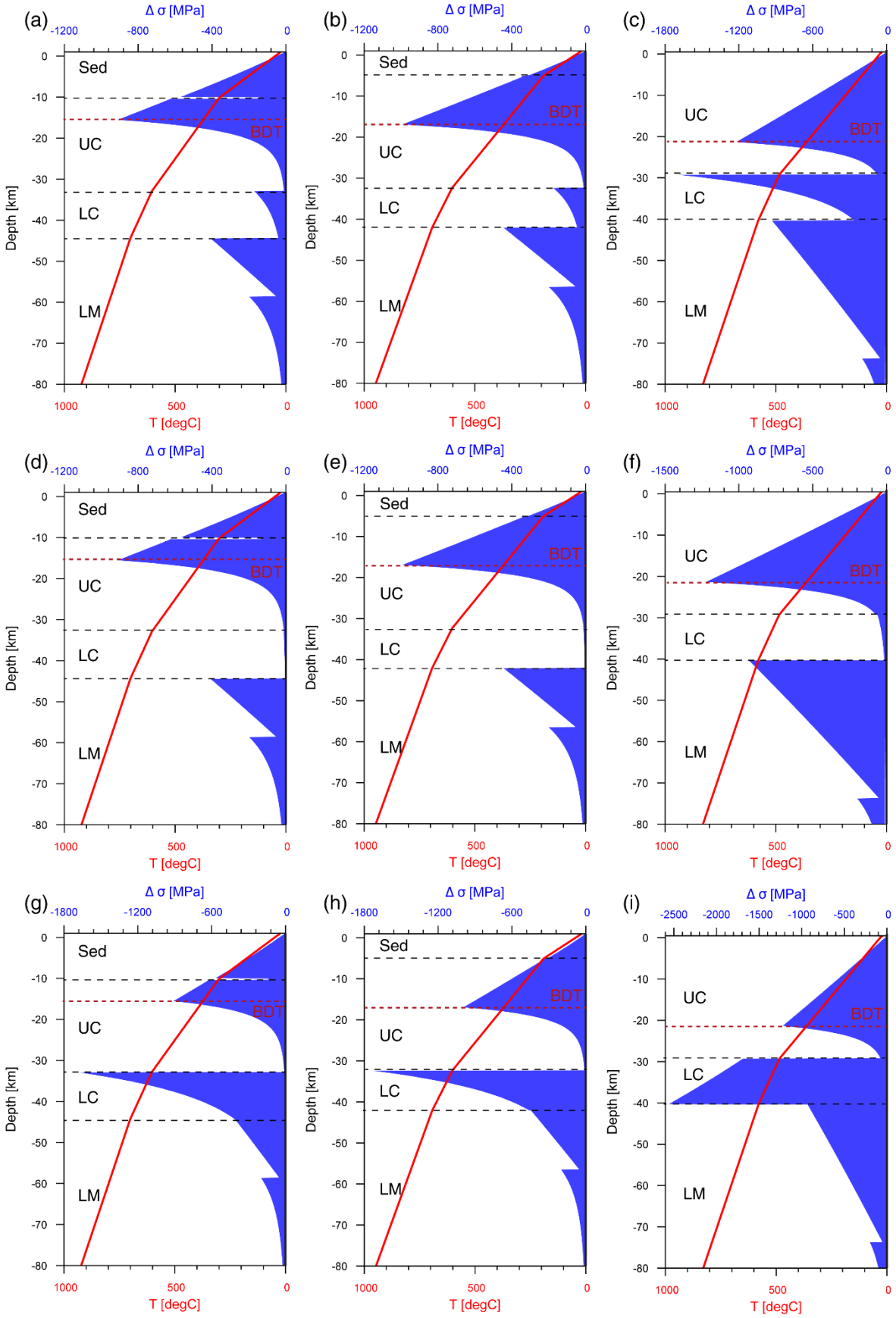
(a)
(b)
(c)
(d)
(e)
(f)
(g)
(h)
(i)
Δ σ [MPa]
Depth [km]
T [degC]
Sed
UC
LC
LM
BDT

The correlation between brittle-ductile transitions and hypocenters in the Santa Barbara System remains the same for each of the three different rock-types because there is no brittle behavior in the lower crust (Figure D.2, b, e & h). There is, however, a fully brittle lower crust in the Pampean Ranges for the diabase rheology (Figure D.2i). The presence of a brittle lower crust is in agreement with the observed seismicity down to the Moho in this morphotectonic unit, which is consistent with the possibility of strong mafic residual rocks in the Pampean Ranges being the focal points for the initiation of seismic slip in the deep lower crust.

Acknowledgements

This study was conducted within the framework of the International Research Training Group StRATEGy (SuRfAce processes, Tectonics and Georesources: The Andean foreland basin of Argentina), funded by CONICET (Consejo Nacional de Investigaciones Científicas y Técnicas) in Argentina and the DFG (Deutsche Forschungsgemeinschaft; grant STR 373/34-1) in Germany. I would like to thank both institutions for funding and supporting this project, and CONICET for granting me a Doctoral Fellowship to carry my studies. I am very thankful to the University of Potsdam and the German Research Center for Geosciences (GFZ) for their research and soft skills trainings, and for granting me access to their facilities to conduct my research.

I would like to thank my supervisors Claudia Prezzi, Magdalena Scheck-Wenderoth and Manfred Strecker, as well as my mentor Judith Bott for all their support and constructive criticism. They allowed me to work freely, while always giving me their advice and keeping me on a reasonable path to finish my dissertation. With them, I learnt how to conduct scientific research and the importance of scientific collaboration and science communication. At this point, I want to emphasize that I am thankful not only for their academic excellence, but also for their quality as persons, which is reflected on their research groups.

Thanks to all members of Section 4.5 at the GFZ, Magdalena, Judith, Mauro, Max, Cameron, Constanza, Nora, Björn, María Laura, Ershad, Denis, Antoine, Ángela, Katharina, Anna and Jessica, for their help during my stays there and for the fruitful and warmth work environment. Special thanks to Christian for all his support, his collaboration on my first publication, and his friendship. Many thanks as well to all members of StRATEGy in Germany and Argentina for the amazing opportunity to learn from the different projects and share discussions. I very much enjoyed the experience of working in such a multidisciplinary and multicultural group.

My gratitude goes also to Verónica Torres-Acosta, Henry Wichura, Andreas Bergner, Dagmar Fritz, Claudia Rössling and Frauke Stobbe, who helped me organize my first research stays in Potsdam and deal with all affairs concerning the university. I would like to thank Edward Sobel and Tanja Klaka-Tauscher as well for the organization of the doctoral defense.

Thanks to all the friends I made during this process, Ahmad, Martin, Joan, Alessia, Federica, Sarah, Jonas, Melanie, Ayelén, Matías, Eva, Caroline, Leonardo, and Flavia, who supported me and made the experience significatively better.

Many thanks as well to my parents, brothers and sister for supporting all my decisions and believing in me, even in the moments I did not. And finally, I am deeply grateful to Alejandro, who unconditionally supported me throughout the past years, every day, despite the distance.

Bibliography

Afonso, J.C., Ranalli, G., 2004. Crustal and mantle strengths in continental lithosphere: Is the jelly sandwich model obsolete? Tectonophysics 394, 221–232. https://doi.org/10.1016/j.tecto.2004.08.006

Albaric, J., Déverchère, J., Petit, C., Perrot, J., Le Gall, B., 2009. Crustal rheology and depth distribution of earthquakes: Insights from the central and southern East African Rift System. Tectonophysics 468, 28–41. https://doi.org/10.1016/j.tecto.2008.05.021

Aldersons, F., Ben-Avraham, Z., Hofstetter, A., Kissling, E., Al-Yazjeen, T., 2003. Lower-crustal strength under the Dead Sea basin from local earthquake data and rheological modeling. Earth Planet. Sci. Lett. 214, 129–142. https://doi.org/10.1016/S0012-821X(03)00381-9

Allmendinger, R.W., 1986. Tectonic development, southeastern border of the Puna Plateau, northwestern Argentine Andes. Geol. Soc. Am. Bull. 97(9), 1070–1082.

Allmendinger, R.W., Jordan, T.E., Kay, S.M., Isacks, B.L., 1997. The Evolution of the Altiplano-Puna Plateau of the Central Andes. Annu. Rev. Earth Planet. Sci. 25, 139–174. https://doi.org/10.1146/annurev.earth.25.1.139

Allmendinger, R.W., Strecker, M.R., Eremchuk, J.E., Francis, P., 1989. Neotectonic deformation of the southern Puna Plateau, northwestern Argentina. J. South Am. Earth Sci. 2, 111–130. https://doi.org/10.1016/0895-9811(89)90040-0

Alonso, R.N., Jordan, K., Tabutt, K., Vandervort, D., 1991. Giant Evaporite Belts in the Neogene Central Andes. Geology 19, 401–404.

Amante, C., Eakins, B.W., 2009. ETOPO1 1 Arc-Minute Global Relief Model: Procedures, Data Sources and Analysis. NOAA Tech. Memo. NESDIS NGDC-24. Natl. Geophys. Data Center, NOAA. https://doi.org/doi:10.7289/V5C8276M

Amilibia, A., Sàbat, F., McClay, K.R., Muñoz, J.A., Roca, E., Chong, G., 2008. The role of inherited tectono-sedimentary architecture in the development of the central Andean mountain belt: Insights from the Cordillera de Domeyko. J. Struct. Geol. 30, 1520–1539. https://doi.org/10.1016/j.jsg.2008.08.005

Andersen, O., Knudsen, P., 1998. Global marine gravity field from the ERS-1 and GEOSAT geodetic mission altimetry. J. Geophys. Res. 103, 8129–8137.

Arnous, A., Zeckra, M., Venerdini, A., Alvarado, P., Arrowsmith, R., Guillemoteau, J., Landgraf, A., Gutierrez, A., Strecker, M.R., 2020. Neotectonic Activity in the Low-Strain Broken Foreland (Santa Bárbara System) of the North-Western Argentinean Andes (26°S). Lithosphere 1, 1–25. https://doi.org/10.2113/2020/8888588

Assumpção, M., Feng, M., Tassara, A., Julià, J., 2013. Models of crustal thickness for South

America from seismic refraction, receiver functions and surface wave tomography. Tectonophysics 609, 82–96. https://doi.org/10.1016/j.tecto.2012.11.014

Assumpçao, M., Schimmel, M., Escalante, C., Barbosa, J.R., Rocha, M., Barros, L. V., 2004. Intraplate seismicity in SE Brazil: Stress concentration in lithospheric thin spots. Geophys. J. Int. 159, 390–399. https://doi.org/10.1111/j.1365-246X.2004.02357.x

Aydin, I., Karat, H.I., Koçak, A., 2005. Curie-point depth map of Turkey. Geophys. J. Int. 162, 633–640. https://doi.org/10.1111/j.1365-246X.2005.02617.x

Babeyko, A.Y., Sobolev, S. V., Trumbull, R.B., Oncken, O., Lavier, L.L., 2002. Numerical models of crustal scale convection and partial melting beneath the Altiplano-Puna plateau. Earth Planet. Sci. Lett. 199, 373–388. https://doi.org/10.1016/S0012-821X(02)00597-6

Babeyko, A.Y., Sobolev, S. V., Vietor, T., Oncken, O., Trumbull, R.B., 2006. Numerical Study of Weakening Processes in the Central Andean Back-Arc, in: Oncken, O., Chong, G., Franz, G., Giese, P., Götze, H.-J., Ramos, V.A., Strecker, M.R., Wigger, P. (Eds.), The Andes: Active Subduction Orogeny. Springer-Verlag Berlin Heidelberg, pp. 495–512. https://doi.org/10.1007/978-3-540-48684-8

Banzon, V., Smith, T.M., Chin, T.M., Liu, C., Hankins, W., 2016. A long-term record of blended satellite and in situ sea-surface temperature for climate monitoring, modeling and environmental studies. Earth Syst. Sci. Data 8, 165–176. https://doi.org/doi:10.5194/essd-8-165-2016

Barazangi, M., Isacks, B.L., 1976. Spatial distribution of earthquakes and subduction of the Nazca plate beneath South America. Geology 4, 686–692.

Bascuñán, S., Arriagada, C., Le Roux, J., Deckart, K., 2016. Unraveling the Peruvian Phase of the Central Andes: Stratigraphy, sedimentology and geochronology of the Salar de Atacama Basin (22°30-23°S), northern Chile. Basin Res. 28, 365–392. https://doi.org/10.1111/bre.12114

Beck, S.L., Zandt, G., 2002. The nature of orogenic crust in the central Andes. J. Geophys. Res. Solid Earth 107, ESE 7-1-ESE 7-16. https://doi.org/10.1029/2000JB000124

Beck, S.L., Zandt, G., Ward, K.M., Scire, A., 2015. Multiple styles and scales of lithospheric foundering beneath the Puna Plateau, central Andes, in: DeCelles, P.G., Ducea, M.N., Carrapa, B., Kapp, P.A. (Eds.), Geodynamics of a Cordilleran Orogenic System: The Central Andes of Argentina and Northern Chile. Geological Society of America, pp. 43–60. https://doi.org/10.1130/2015.1212(03)

Bhattacharyya, B.K., Leu, L.K., 1977. Spectral analysis of gravity and magnetic anomalies due to rectangular prismatic bodies. Geophysics.

Bianchi, M., Heit, B., Jakovlev, A., Yuan, X., Kay, S.M., Sandvol, E., Alonso, R.N., Coira, B.,

Brown, L., Kind, R., Comte, D., 2013. Teleseismic tomography of the southern Puna plateau in Argentina and adjacent regions. Tectonophysics 586, 65–83. https://doi.org/10.1016/j.tecto.2012.11.016

Blakely, R.J., 1996. Potential Theory in Gravity and Magnetic Applications. Cambridge University Press.

Bock, B., Bahlburg, H., Wörner, G., Zimmermann, U., 2000. Tracing Crustal Evolution in the Southern Central Andes from Late Precambrian to Permian with Geochemical and Nd and Pb Isotope Data. J. Geol. 108, 515–535. https://doi.org/10.1086/314422

Brocher, T.M., 2005. Empirical relations between elastic wavespeeds and density in the Earth's crust. Bull. Seismol. Soc. Am. 95, 2081–2092. https://doi.org/10.1785/0120050077

Brooks, B.A., Bevis, M., Whipple, K., Arrowsmith, J.A., Foster, J., Zapata, T., Kendrick, E., Minaya, E., Echalar, A., Blanco, M., Euillades, P., Sandoval, M., Smalley, R.J., 2011. Orogenic-wedge deformation and potential for great earthquakes in the central Andean backarc. Nat. Geosci. 4, 380–383.

Bryant, A.S., Jones, L.M., 1992. Anomalously deep crustal earthquakes in the Ventura Basin, Southern California. J. Geophys. Res. 97, 437–447. https://doi.org/10.1029/91JB02286

Burns, D.H., de Silva, S.L., Tepley, F., Schmitt, A.K., Loewen, M.W., 2015. Recording the transition from flare-up to steady-state arc magmatism at the Purico-Chascon volcanic complex, northern Chile. Earth Planet. Sci. Lett. 422, 75–86. https://doi.org/10.1016/j.epsl.2015.04.002

Burns, E.R., Williams, C.F., Ingebritsen, S.E., Voss, C.I., Spane, F.A., Deangelo, J., 2016. Understanding heat and groundwater flow through continental flood basalt provinces: Insights gained from alternative models of permeability/depth relationships for the Columbia Plateau, United States, in: Gleeson, T., Ingebritse, S.E. (Eds.), Crustal Permeability. John Wiley & Sons Ltd, pp. 137–154. https://doi.org/10.1002/9781119166573.ch13

Burov, E., Jaupart, C., Mareschal, J.C., 1998. Large-scale crustal heterogeneities and lithospheric strength in cratons. Earth Planet. Sci. Lett. 164, 205–219. https://doi.org/10.1016/S0012-821X(98)00205-2

Burov, E.B., 2010. The equivalent elastic thickness (Te), seismicity and the long-term rheology of continental lithosphere: Time to burn-out "crème brûlée"?. Insights from large-scale geodynamic modeling. Tectonophysics 484, 4–26. https://doi.org/10.1016/j.tecto.2009.06.013

Burov, E.B., Diament, M., 1995. The effective elastic thickness (Te) of continental lithosphere: what does it really mean? J. Geophys. Res. 100, 3905–3927.

https://doi.org/10.1029/94JB02770

Burov, E.B., Watts, A.B., 2006. The long-term strength of continental lithosphere : " jelly sandwich " or " crème brûlée "? GSA Today 16, 4–10. https://doi.org/10.1130/1052-5173(2006)016<4:TLTSOC>2.0.CO;2

Butler, R.W.H., Tavarnelli, E., Grasso, M., 2006. Structural inheritance in mountain belts: An Alpine–Apennine perspective. J. Struct. Geol. 28, 1893–1908. https://doi.org/10.1016/j.jsg.2006.09.006

Byerlee, J.D., 1968. Brittle-Ductile Transition in Rocks. J. Geophys. Res. 73, 4741–4750. https://doi.org/10.1029/JB073i014p04741

Cacace, M., Bayer, U., Marotta, A.M., 2008. Strain localization due to structural in-homogeneities in the Central European Basin System. Int. J. Earth Sci. 97, 899–913. https://doi.org/10.1007/s00531-007-0192-0

Cacace, M., Jacquey, A.B., 2017. Flexible parallel implicit modelling of coupled thermal–hydraulic–mechanical processes in fractured rocks. Solid Earth 8, 921–941. https://doi.org/10.5194/se-8-921-2017

Cacace, M., Scheck-Wenderoth, M., 2016. Why intracontinental basins subside longer: 3-D feedback effects of lithospheric cooling and sedimentation on the flexural strength of the lithosphere. J. Geophys. Res. Solid Earth 121, 3742–3761. https://doi.org/doi:10.1002/2015JB012682

Calixto, F.J., Sandvol, E., Kay, S., Mulcahy, P., Heit, B., Yuan, X., Coira, B., Comte, D., Alvarado, P., 2013. Velocity structure beneath the southern Puna plateau: Evidence for delamination. Geochemistry, Geophys. Geosystems 14, 4292–4305. https://doi.org/10.1002/ggge.20266

Camelbeek, T., Iranga, M., 1996. Deep crustal earthquakes and geometry of active faults along the Rukwa trough, East Africa. Geophys. J. Int. 124, 612–630. https://doi.org/10.1111/j.1365-246X.1996.tb07040.x

Cammarano, F., Goes, S., Vacher, P., Giardini, D., 2003. Inferring upper-mantle temperatures from seismic velocities. Phys. Earth Planet. Inter. 138, 197–222. https://doi.org/doi:10.1016/S0031-9201(03)00156-0

Casquet, C., Rapela, C.W., Pankhurst, R.J., Baldo, E.G., Galindo, C., Fanning, C.M., Dahlquist, J.A., Saavedra, J., 2012. A history of Proterozoic terranes in southern South America: From Rodinia to Gondwana. Geosci. Front. 3, 137–145. https://doi.org/10.1016/j.gsf.2011.11.004

Čermák, V., Rybach, L., 1982. Thermal conductivity and specific heat of minerals and rocks, in: Angenheister, G. (Ed.), Landolt-Börnstein: Numerical Data and Functional Relationships in Science and Technology, New Series, Group V (Geophysics and Space

Research), Vol. 1a (Physical Properties of Rocks). Springer Verlag, Berlin, Heidelberg and New York, pp. 305–343.

Chapman, D.S., 1986. Thermal gradients in the continental crust, in: Dawson, J.M., Carswell, D.A., Hall, J., Wedepohl, K.H. (Eds.), The Nature of the Lower Continental Crust. pp. 63–70.

Chebli, G.A., Mozetic, M.E., Rossello, E.A., Bühler, M., Caminos, R., 1999. Cuencas sedimentarias de la llanura Chacopampeana, in: Caminos, R. (Ed.), Geología Argentina. pp. 627–644.

Chen, L., Song, X., Gerya, T. V., Xu, T., Chen, Y., 2019. Crustal melting beneath orogenic plateaus: Insights from 3-D thermo-mechanical modeling. Tectonophysics 761, 1–15. https://doi.org/10.1016/j.tecto.2019.03.014

Chen, W., Molnar, P., 1983. Focal depths of intracontinental and intraplate earthquakes and their implications for the mechanical properties of the lithosphere. J. Geophys. Res. Solid Earth 88, 4183–4214. https://doi.org/10.1029/JB088iB05p04183

Chiozzi, P., Matsushima, J., Okubo, Y., Pasquale, V., Verdoya, M., 2005. Curie-point depth from spectral analysis of magnetic data in central – southern Europe. Phys. Earth Planet. Inter. 152, 267–276. https://doi.org/10.1016/j.pepi.2005.04.005

Chmielowski, J., Zandt, G., Haberland, C., 1999. The Central Andean Altiplano-Puna Magma Body. Geophys. Res. Lett. 26, 783–786. https://doi.org/10.1029/1999GL900078

Christensen, N.I., Mooney, W.D., 1995. Seismic velocity structure and composition of the continental crust: A global view. J. Geophys. Res. 100, 9761. https://doi.org/10.1029/95JB00259

Chulick, G.S., Detweiler, S., Mooney, W.D., 2013. Seismic structure of the crust and uppermost mantle of South America and surrounding oceanic basins. J. South Am. Earth Sci. 42, 260–276. https://doi.org/10.1016/j.jsames.2012.06.002

Coira, B., Kay, S.M., 1993. Implications of Quaternary volcanism at Cerro Tuzgle for crustal and mantle evolution of the high Puna Plateau, Central Andes, Argentina. Contrib. to Mineral. Petrol. 113, 40–58.

Coira, B., Koukharsky, M., Guevara, S.R., Cisterna, C.E., 2009. Puna (Argentina) and northern Chile Ordovician basic magmatism: A contribution to the tectonic setting. J. South Am. Earth Sci. 27, 24–35. https://doi.org/10.1016/j.jsames.2008.10.002

Collo, G., Ezpeleta, M., Dávila, F.M., Giménez, M., Soler, S., Martina, F., Ávila, P., Sánchez, F., Calegari, R., Lovecchio, J., Schiuma, M., 2018. Basin thermal structure in the Chilean-Pampean flat subduction zone, in: Folguera, A., Contreras Reyes, E., Heredia, N., Encinas, A., Iannelli, S.B., Oliveros, V., Dávila, F.M., Collo, G., Giambiagi, L.,

Maksymowicz, A., Iglesia Llanos, M.P., Turienzo, M., Naipauer, M., Orts, D., Litvak, V.D., Alvarez, O., Arriagada, C. (Eds.), The Evolution of the Chilean-Argentinean Andes. Springer International Publishing AG, pp. 537–564. https://doi.org/10.1007/978-3-319-67774-3_21

Comeau, M.J., Unsworth, M.J., Cordell, D., 2016. New constraints on the magma distribution and composition beneath Volcán Uturuncu and the southern Bolivian Altiplano from magnetotelluric data. Geosphere 12, 1391–1421. https://doi.org/10.1130/GES01277.1

Comeau, M.J., Unsworth, M.J., Ticona, F., Sunagua, M., 2015. Magnetotelluric images of magma distribution beneath Volcán Uturuncu, Bolivia: Implications for magma dynamics. Geology 43, 243–246. https://doi.org/10.1130/G36258.1

Costa, C.H., Owen, L.A., Ricci, W.A., Johnson, W.J., Halperin, A.D., 2018. Holocene activity and seismogenic capability of intraplate thrusts: Insights from the Pampean Ranges, Argentina. Tectonophysics 737, 57–70. https://doi.org/10.1016/j.tecto.2018.05.002

Coutand, I., Gautier, P., Cobbold, P.R., de Urreiztieta, M., Chauvin, A., Gapais, D., Rossello, E.A., Lopez-Gammundi, O., 2001. Style and history of Andean deformation, Puna Plateau, northwestern Argentina. Tectonics 20, 210–234.

Currie, C.A., Hyndman, R.D., 2006. The thermal structure of subduction zone back arcs. J. Geophys. Res. Solid Earth 111, B08404. https://doi.org/10.1029/2005JB004024

Daxberger, H., Riller, U., 2015. Kinematics of Neogene to Recent upper-crustal deformation in the southern Central Andes (23°-28°S) inferred from fault-slip analysis: Evidence for gravitational spreading of the Puna Plateau. Tectonophysics 642, 16–28. https://doi.org/10.1016/j.tecto.2014.12.003

de Silva, S., 1989. Altiplano-Puna volcanic complex of the Central Andes. Geology 17, 1102–1106.

Decelles, P.G., Ducea, M.N., Kapp, P., Zandt, G., 2009. Cyclicity in Cordilleran orogenic systems. Nat. Geosci. 2, 251–257. https://doi.org/10.1038/ngeo469

DeCelles, P.G., Zandt, G., Beck, S.L., Currie, C.A., Ducea, M.N., Kapp, P., Gehrels, G.E., Carrapa, B., Quade, J., Schoenbohm, L.M., 2015. Cyclical orogenic processes in the Cenozoic central Andes, in: DeCelles, P.G., Ducea, M.N., Carrapa, B., Kapp, P.A. (Eds.), Geodynamics of a Cordilleran Orogenic System: The Central Andes of Argentina and Northern Chile. Geological Society of America, pp. 459–490. https://doi.org/10.1130/2015.1212(22)

Deichmann, N., 1992. Structural and rheological implications of lower-crustal earthquakes below northern Switzerland. Phys. Earth Planet. Inter. 69, 270–280. https://doi.org/10.1016/0031-9201(92)90146-M

Desegaulx, P., Kooi, H., Cloetingh, S., 1991. Consequences of foreland basin development on thinned continental lithosphere: application to the Aquitaine basin (SW France). Earth Planet. Sci. Lett. 106, 116–132. https://doi.org/10.1016/0012-821X(91)90067-R

Déverchère, J., Petit, C., Gileva, N., Radziminovitch, N., Melnikova, V., San'kov, V., 2001. Depth distribution of earthquakes in the Baikal rift system and its implications for the rheology of the lithosphere. Geophys. J. Int. 146, 714–730. https://doi.org/10.1046/j.0956-540x.2001.1484.484.x

Devlin, S., Isacks, B.L., Pritchard, M.E., Barnhart, W.D., Lohman, R.B., 2012. Depths and focal mechanisms of crustal earthquakes in the central Andes determined from teleseismic waveform analysis and InSAR. Tectonics 31, TC2002. https://doi.org/https://doi.org/10.1029/2011TC002914

Díaz, D., Brasse, H., Ticona, F., 2012. Conductivity distribution beneath Lascar volcano (Northern Chile) and the Puna, inferred from magnetotelluric data. J. Volcanol. Geotherm. Res. 217–218, 21–29. https://doi.org/10.1016/j.jvolgeores.2011.12.007

Dorbath, C., Masson, F., 2000. Composition of the crust and upper-mantle in the Central Andes (19°30'S) inferred from P wave velocity and Poisson's ratio. Tectonophysics 327, 213–223.

Doser, D.I., Kanamori, H., 1986. Depth of seismicity in the Imperial Valley Region (1977–1983) and its relationship to heat flow, crustal structure and the October 15, 1979, earthquake. J. Geophys. Res. Solid Earth 91, 675–688. https://doi.org/10.1029/JB091iB01p00675

Drew, S.T., Ducea, M.N., Schoenbohm, L.M., 2009. Mafic volcanism on the Puna Plateau, NW Argentina: Implications for lithospheric composition and evolution with an emphasis on lithospheric foundering. Lithosphere 1, 305–318. https://doi.org/10.1130/L54.1

Dunn, J.F., Hartshorn, K.G., Hartshorn, P.W., 1995. Structural styles and hydrocarbon potential of the Subandean thrust belt of Southern Bolivia, in: Tankard, A.J., Suarez Soruco, R., Welsink, H.J. (Eds.), Petroleum Basins of South America. AAPG Memoir, vol. 62, pp. 523–543.

Dziewonski, A.M., Chou, T.-A., Woodhouse, J.H., 1981. Determination of earthquake source parameters from waveform data for studies of global and regional seismicity. J. Geophys. Res. 86, 2825–2852. https://doi.org/doi:10.1029/JB086iB04p02825

Ebbing, J., 2002. 3-D Dichteverteilung und isostatisches Verhalten der Lithosphäre in den Ostalpen. PhD thesis, Freie Univ. Berlin 143.

Eichelberger, N., McQuarrie, N., Ryan, J., Karimi, B., Beck, S., Zandt, G., 2015. Evolution of crustal thickening in the central Andes, Bolivia. Earth Planet. Sci. Lett. 426, 191–203. https://doi.org/10.1016/j.epsl.2015.06.035

Ekström, G., Nettles, M., Dziewonski, A.M., 2012. The global CMT project 2004-2010: Centroid-moment tensors for 13,017 earthquakes. Phys. Earth Planet. Inter. 200–201, 1–9. https://doi.org/doi:10.1016/j.pepi.2012.04.002

Elger, K., Oncken, O., Glodny, J., 2005. Plateau-style accumulation of deformation: southern Altiplano. Tectonics 24. https://doi.org/doi:10/1029/2004TC001675

Engdahl, E.R., Hilst, R. Van Der, Buland, R., 1998. Global Teleseismic Earthquake Relocation with Improved Travel Times and Procedures for Depth Determination. Bull. Seismol. Soc. Am. 88, 722–743.

Escayola, M.P., van Staal, C.R., Davis, W.J., 2011. The age and tectonic setting of the Puncoviscana Formation in northwestern Argentina: An accretionary complex related to Early Cambrian closure of the Puncoviscana Ocean and accretion of the Arequipa-Antofalla block. J. South Am. Earth Sci. 32, 438–459. https://doi.org/10.1016/j.jsames.2011.04.013

Feng, M., van der Lee, S., Assumpção, M., 2007. Upper mantle structure of South America from joint inversion of waveforms and fundamental mode group velocities of Rayleigh waves. J. Geophys. Res. Solid Earth 112, B04312. https://doi.org/10.1029/2006JB004449

Fernández-Ibáñez, F., Soto, J.I., 2008. Crustal rheology and seismicity in the Gibraltar Arc (western Mediterranean). Tectonics 27, TC2007. https://doi.org/https://doi.org/10.1029/2007TC002192

Flesch, L.M., Kreemer, C., 2010. Gravitational potential energy and regional stress and strain rate fields for continental plateaus: Examples from the central Andes and Colorado Plateau. Tectonophysics 482, 182–192. https://doi.org/10.1016/j.tecto.2009.07.014

Flóvenz, Ó.G., Saemundsson, K., 1993. Heat flow and geothermal processes in Iceland. Tectonophysics 225, 123–138. https://doi.org/10.1016/0040-1951(93)90253-G

Franz, G., Lucassen, F., Kramer, W., Trumbull, R.B., Romer, R.L., Wilke, H.-G., Viramonte, J.G., Becchio, R., Siebel, W., 2006. Crustal evolution at the Central Andean continental margin: a geochemical record of crustal growth, recycling and destruction, in: Oncken, O., Chong, G., Franz, G., Giese, P., Götze, H.-J., Ramos, V.A., Strecker, M.R., Wigger, P. (Eds.), The Andes: Active Subduction Orogeny. Springer, Berlin, pp. 45–64. https://doi.org/10.1007/978-3-540-48684-8_3

Fromm, R., Zandt, G., Beck, S.L., 2004. Crustal thickness beneath the Andes and Sierras Pampeanas at 30°S inferred from Pn apparent phase velocities. Geophys. Res. Lett. 31, n/a-n/a. https://doi.org/10.1029/2003GL019231

Furlong, K.P., Chapman, D.S., 2013. Heat Flow, Heat Generation, and the Thermal State of the Lithosphere. Annu. Rev. Earth Planet. Sci. 41, 385–410.

https://doi.org/https://doi.org/10.1146/annurev.earth.031208.100051

Garcia, E.S., Sandwell, D.T., Luttrell, K.M., 2014. An iterative spectral solution method for thin elastic plate flexure with variable rigidity. Geophys. J. Int. 200, 1012–1028. https://doi.org/10.1093/gji/ggu449

García, H.P.A., Gianni, G.M., Lupari, M.N., Sánchez, M.A., Soler, S.R., Ruiz, F., Lince Klinger, F.G., 2017. Effective elastic thickness in the Central Andes. Correlation to orogenic deformation styles and lower crust high-gravity anomaly. J. South Am. Earth Sci. https://doi.org/10.1016/j.jsames.2017.11.021

García, V.H., Hongn, F., Yagupsky, D., Pingel, H., Kinnaird, T., Winocur, D., Cristallini, E., Robinson, R.A.J., Strecker, M.R., 2019. Late Quaternary tectonics controlled by fault reactivation. Insights from a local transpressional system in the intermontane Lerma valley, Cordillera Oriental, NW Argentina. J. Struct. Geol. 128, 103875. https://doi.org/10.1016/j.jsg.2019.103875

Gerbault, M., Martinod, J., Hérail, G., 2003. Possible orogeny-parallel lower crustal flow and thickening in the Central Andes. Tectonophysics 399, 59–72. https://doi.org/10.1016/j.tecto.2004.12.015

Ghosh, A., Holt, W.E., Flesch, L.M., 2009. Contribution of gravitational potential energy differences to the global stress field. Geophys. J. Int. 179, 787–812. https://doi.org/10.1111/j.1365-246X.2009.04326.x

Global-Volcanism-Program, 2013. Volcanoes of the World, v. 4.9.0., Venzke, E. (ed.). Smithson. Institution.Downloaded 20 May 2020. https://doi.org/10.5479/si.GVP.VOTW4-2013

Goes, S., Govers, R., Vacher, P., 2000. Shallow mantle temperatures under Europe from P and S wave tomography. J. Geophys. Res. Earth 105, 11153–11169. https://doi.org/10.1029/1999jb900300

Goetze, C., 1978. The mechanism of creep in olivine. Philos. Trans. R. Soc. London. Ser. A, Math. Phys. Sci. 288, 99–119. https://doi.org/10.1098/rsta.1978.0008

Goetze, C., Evans, B., 1979. Stress and temperature in the bending lithosphere as constrained by experimental rock mechanics. Geophys. J. Int. 59, 463–478. https://doi.org/10.1111/j.1365-246X.1979.tb02567.x

Götze, H.-J., Lahmeyer, B., Schmidt, S., Strunk, S., Araneda, M., 1990. Central Andes gravity data base. Eos, Trans. Am. Geophys. Union 71, 401–407. https://doi.org/https://doi.org/10.1029/90EO00148

Götze, H.J., Krause, S., 2002. The Central Andean gravity high, a relic of an old subduction complex? J. South Am. Earth Sci. 14, 799–811. https://doi.org/10.1016/S0895-9811(01)00077-3

Graeber, F.M., 1997. Seismische Geschwindigkeiten und Hypozentren in den Südlichen Zentralen Anden aus der simultanen Inversion von Laufzeitdaten des seismologischen Experiments PISCO ’94 in Nordchile. Ph.D. thesis, GeoForschungszentrum Potsdam, Germany.

Graeber, F.M., Asch, G., 1999. Three-dimensional models of P-wave velocity and P- to S-velocity ratio in the southern central Andes by simultaneous inversion of local earthquake data. J. Geophys. Res. 104, 20237–20256.

Grier, M.E., Salfity, J.A., Allmendinger, R.W., 1991. Andean reactivation of the Cretaceous Salta rift, northwestern Argentina. J. South Am. Earth Sci. 4, 351–372. https://doi.org/10.1016/0895-9811(91)90007-8

Guzmán, S., Grosse, P., Montero-López, C., Hongn, F., Pilger, R., Petrinovic, I., Seggiaro, R., Aramayo, A., 2014. Spatial-temporal distribution of explosive volcanism in the 25-28°S segment of the Andean Central Volcanic Zone. Tectonophysics 636, 170–189. https://doi.org/10.1016/j.tecto.2014.08.013

Haberland, C., Rietbrock, A., 2001. Attenuation tomography in the western central Andes: A detailed insight into the structure of a magmatic arc. J. Geophys. Res. 106, 11151–11167.

Hacker, B.R., Kelemen, P.B., Behn, M.D., 2011. Differentiation of the continental crust by relamination. Earth Planet. Sci. Lett. 307, 501–516. https://doi.org/10.1016/j.epsl.2011.05.024

Hall, P.S., 2012. On the thermal evolution of the mantle wedge at subduction zones. Phys. Earth Planet. Inter. 198–199, 9–27. https://doi.org/10.1016/j.pepi.2012.03.004

Hamza, V.M., Dias, F.J.S.S., Gomes, A.J.L., Terceros, Z.G.D., 2005. Numerical and functional representations of regional heat flow in South America. Phys. Earth Planet. Inter. 152, 223–256. https://doi.org/10.1016/j.pepi.2005.04.009

Hamza, V.M., Muñoz, M., 1996. Heat flow map of South America. Geothermics 25, 599–646. https://doi.org/10.1016/S0375-6505(96)00025-9

Handy, M.R., Brun, J.P., 2004. Seismicity, structure and strength of the continental lithosphere. Earth Planet. Sci. Lett. 223, 427–441. https://doi.org/10.1016/j.epsl.2004.04.021

Hasterok, D., Webb, J., 2017. On the radiogenic heat production of igneous rocks. Geosci. Front. 8, 919–940. https://doi.org/10.1016/j.gsf.2017.03.006

Heit, B., 2005. Teleseismic tomographic images of the Central Andes at 21 ° S and 25 . 5 ° S : an inside look at the Altiplano and Puna plateaus. Diss. zur Erlangung des Doktorgrades am Fachbereich Geowissenschaften der Freien Univ. Berlin.

Heit, B., Bianchi, M., Yuan, X., Kay, S.M., Sandvol, E., Kumar, P., Kind, R., Alonso, R.N.,

Brown, L.D., Comte, D., 2014. Structure of the crust and the lithosphere beneath the southern Puna plateau from teleseismic receiver functions. Earth Planet. Sci. Lett. 385, 1–11. https://doi.org/10.1016/j.epsl.2013.10.017

Heit, B., Koulakov, I., Asch, G., Yuan, X., Kind, R., Alcocer-Rodriguez, I., Tawackoli, S., Wilke, H., 2008. More constraints to determine the seismic structure beneath the Central Andes at 21°S using teleseismic tomography analysis. J. South Am. Earth Sci. 25, 22–36. https://doi.org/10.1016/j.jsames.2007.08.009

Heit, B., Sodoudi, F., Yuan, X., Bianchi, M., Kind, R., 2007a. An S receiver function analysis of the lithospheric structure in South America. Geophys. Res. Lett. 34, L14307. https://doi.org/10.1029/2007GL030317

Heit, B., Yuan, X., Kind, R., Asch, G., 2007b. Lithospheric Dynamics in the Southernmost Andean Plateau (PUDEL). Dtsch. GeoForschungsZentrum GFZ. https://doi.org/10.14470/7O092361

Henriquez, S., DeCelles, P.G., Carrapa, B., Hughes, A., Davis, G., Alvarado, P., 2020. Deformation history of the Puna plateau, Central Andes of northwestern Argentina. J. Struct. Geol. https://doi.org/doi: https://doi.org/10.1016/j.jsg.2020.104133.

Henry, S., Pollack, H., 1988. Terrestrial Heat Flow Above the Andean Subduction Zone in Bolivia and Peru. J. Geophys. Res. 93, 153–162. https://doi.org/10.1029/JB093iB12p15153

Hilley, G.E., Strecker, M.R., 2005. Processes of oscillatory basin filling and excavation in a tectonically active orogen: Quebrada del Toro Basin, NW Argentina. Geol. Soc. Am. Bull. 117, 887–901. https://doi.org/10.1130/B25602.1

Hindle, D., Kley, J., Oncken, O., Sobolev, S., 2005. Crustal balance and crustal flux from shortening estimates in the Central Andes. Earth Planet. Sci. Lett. 230, 113–124. https://doi.org/10.1016/j.epsl.2004.11.004

Hobbs, B.E., Ord, A., Teyssier, C., 1986. Earthquakes in the ductile regime? Pure Appl. Geophys. 124, 309–336. https://doi.org/10.1007/BF00875730

Hsieh, H., Chen, C., Lin, P., Yen, H., 2014. Curie point depth from spectral analysis of magnetic data in Taiwan. J. Asian Earth Sci. 90, 26–33. https://doi.org/10.1016/j.jseaes.2014.04.007

Huerta, A.D., Royden, L.H., Hodges, K.V., 1998. The thermal structure of collisional orogens as a response to accretion, erosion and radiogenic heating. J. Geophys. Res. Solid Earth 103, 15287–15302. https://doi.org/10.1029/98JB00593

Hunt, C.P., Moskowitz, B.M., Banerjee, S.K., 2013. Magnetic Properties of Rocks and Minerals, in: Ahrens, T.J. (Ed.), Rock Physics & Phase Relations.

Husson, L., Moretti, I., 2002. Thermal regime of fold and thrust belts - An application to

the Bolivian Sub Andean Zone. Tectonophysics 345, 253–280. https://doi.org/10.1016/S0040-1951(01)00216-5

Hyndman, R.D., Currie, C.A., Mazzotti, S., Frederiksen, A., 2009. Temperature control of continental lithosphere elastic thickness, Te vs Vs. Earth Planet. Sci. Lett. 277, 539–548. https://doi.org/10.1016/j.epsl.2008.11.023

Hyndman, R.D., Currie, C.A., Mazzotti, S.P., 2005. Subduction zone backarcs, mobile belts, and orogenic heat. GSA Today 15, 4–10. https://doi.org/10.1130/1052-5173(2005)015<4:SZBMBA>2.0.CO;2

Hyndman, R.D., Peacock, S.M., 2003. Serpentinization of the forearc mantle. Earth Planet. Sci. Lett. 212, 417–432. https://doi.org/10.1016/S0012-821X(03)00263-2

Ibarra, F., Prezzi, C.B., 2019. The thermo-mechanical state of the Andes in the Altiplano-Puna region: insights from Curie isotherm and effective elastic thickness determination. Rev. la Asoc. Geol. Argentina 76, 352–362.

International Seismological Centre, 2020. ISC-EHB dataset. https://doi.org/https://doi.org/10.31905/PY08W6S3

Isacks, B.L., 1988. Uplift of the Central Andean Plateau and bending of the Bolivian Orocline. J. Geophys. Res. Solid Earth 93, 3211–3231. https://doi.org/10.1029/JB093iB04p03211

Ito, K., 1990. Regional Variations of the Cutoff Depth of Seismicity in the Crust and Their Relation to Heat Flow and Large Inland-Earthquakes. J. Phys. Earth 38, 223–250. https://doi.org/10.4294/jpe1952.38.223

Jackson, J., 2002. Strength of the continental lithosphere: Time to abandon the jelly sandwich? GSA Today 12, 4–9. https://doi.org/10.1130/1052-5173(2002)012<0004:SOTCLT>2.0.CO;2

Jacquey, A.B., Cacace, M., 2017. GOLEM, a MOOSE-based application v1.0. Zenodo. https://doi.org/10.5281/zenodo.999401

Jaupart, C., Mareschal, J.-C., 2007. Heat Flow and Thermal Structure of the Lithosphere. Treatise Geophys. 6, 217–252. https://doi.org/10.1016/B978-0-444-53802-4.00114-7

Jaupart, C., Mareschal, J.C., 2011. Heat generation and transport in the Earth. Cambridge University Press.

Jordan, T.E., Allmendinger, R.W., 1986. The Sierras Pampeanas of Argentina: a modern analogue of Rocky Mountain foreland deformation. Am. J. Sci. 286, 737–764.

Jordan, T.E., Isacks, B.L., Allmendinger, R.W., Brewer, J., Ramos, V.A., Ando, C., 1983. Andean tectonics related to geometry of the subducted Nazca plate. Geol. Soc. Am. Bull. 94, 341–361. https://doi.org/10.1130/0016-

7606(1983)94<341:ATRTGO>2.0.CO;2

Kaus, B.J.P., Popov, A.A., Baumann, T.S., Pusok, A.E., Bauville, A., Fernandez, N., Collignon, M., 2016. Forward and inverse modelling of lithospheric deformation on geological timescales. NIC Symp. 2016 - Proc. 48, 299–307.

Kay, S.M., Coira, B., 2009. Shallowing and steepening subduction zones, continental lithospheric loss, magmatism, and crustal flow under the central Andean Altiplano-Puna Plateau, in: Kay, S.M., Ramos, V.A., Dickinson, W.R. (Eds.), Backbone of the Americas: Shallow Subduction, Plateau Uplift, and Ridge and Terrane Collision. Geological Society of America, pp. 229–259. https://doi.org/10.1130/2009.1204(11).

Kay, S.M., Coira, B., Viramonte, J., 1994. Young mafic back arc volcanic rocks as indicators of continental lithospheric delamination beneath the Argentine Puna Plateau, Central Andes. J. Geophys. Res. 99, 24323–24339. https://doi.org/10.1029/94JB00896

Kay, S.M., Coira, B.L., Caffe, P.J., Chen, C.H., 2010. Regional chemical diversity, crustal and mantle sources and evolution of central Andean Puna plateau ignimbrites. J. Volcanol. Geotherm. Res. 198, 81–111. https://doi.org/10.1016/j.jvolgeores.2010.08.013

Kennett, B.L.N., Engdahl, E.R., Buland, R., 1995. Constraints on seismic velocities in the Earth from traveltimes. Geophys. J. Int. 122, 108–124. https://doi.org/10.1111/j.1365-246X.1995.tb03540.x

Kirby, S.H., 1983. Rheology of the lithosphere. Rev. Geophys. Sp. Phys. 21, 1458–1487.

Kirby, S.H., Kronenberg, A.K., 1987. Rheology of the lithosphere: Selected topics. Rev. Geophys. 25, 1219–1244. https://doi.org/10.1029/RG025i006p01219

Kley, J., Monaldi, C.R., 2002. Tectonic inversion in the Santa Bárbara System of the central Andean foreland thrust belt, northwestern Argentina. Tectonics 21, 1061–1079. https://doi.org/10.1029/2002TC902003

Kley, J., Monaldi, C.R., Salfity, J.A., 1999. Along-strike segmentation of the Andean foreland: Causes and consequences. Tectonophysics 301, 75–94. https://doi.org/10.1016/S0040-1951(98)90223-2

Kley, J., Rossello, E.A., Monaldi, C.R., Habighorst, B., 2005. Seismic and field evidence for selective inversion of Cretaceous normal faults, Salta rift, northwest Argentina. Tectonophysics 399, 155–172. https://doi.org/10.1016/j.tecto.2004.12.020

Koptev, A.I., Ershov, A. V., 2011. Thermal thickness of the Earth's lithosphere: a numerical model. Moscow Univ. Geol. Bull. 66, 323–330. https://doi.org/10.3103/S014587521105005X

Koulakov, I., Sobolev, S. V., Asch, G., 2006. P - And S-velocity images of the lithosphere-asthenosphere system in the Central Andes from local-source tomographic inversion.

Geophys. J. Int. 167, 106–126. https://doi.org/10.1111/j.1365-246X.2006.02949.x

Kreemer, C., Blewitt, G., Klein, E.C., 2014. A geodetic plate motion and Global Strain Rate Model. Geochemistry Geophys. Geosystems 15, 3849–3889. https://doi.org/10.1002/2014GC005407

Lamb, S., 2015. Cenozoic uplift of the Central Andes in northern Chile and Bolivia – reconciling paleoaltimetry with the geological evolution. Can. J. Earth Sci. 53, 1227–1245. https://doi.org/10.1139/cjes-2015-0071

Lamb, S., 2000. Active deformation in the Bolivian Andes, South America. J. Geophys. Res. 105, 2627–2653.

Lamb, S., Davis, P., 2003. Cenozoic climate change as a possible cause for the rise of the Andes. Nature 425, 792–797. https://doi.org/10.1038/nature02049

Lamontagne, M., Ranalli, G., 1996. Thermal and rheological constraints on the earthquake depth distribution in the Charlevoix, Canada, intraplate seismic zone. Tectonophysics 257, 55–69. https://doi.org/10.1016/0040-1951(95)00120-4

Lesher, C.E., Spera, F.J., 2015. Thermodynamic and Transport Properties of Silicate Melts and Magma, in: The Encyclopedia of Volcanoes. Elsevier Inc., pp. 113–141. https://doi.org/10.1016/B978-0-12-385938-9.00005-5

Lessel, K., 1997. Die Krustenstruktur der Zentralen Anden in Nordchile (21–24°S), abgeleitet aus 3D- Modellierungen refraktionsseismischer Daten. PhD thesis, Freie Univ. Berlin.

Li, Z.-H., Liu, M., Gerya, T., 2016. Lithosphere delamination in continental collisional orogens: A systematic numerical study. J. Geophys. Res. Solid Earth 121, 5186–5211. https://doi.org/10.1002/2016JB013106

Liang, X., Sandvol, E., Kay, S.M., Heit, B., Yuan, X., Mulcahy, P., Chen, C., Brown, L.D., Comte, D., Alvarado, P., 2014. Delamination of southern Puna lithosphere revealed by body wave attenuation tomography. J. Geophys. Res. Solid Earth 119, 549–566. https://doi.org/10.1002/2013JB010309

Lin, A.T., Watts, A.B., 2002. Origin of the West Taiwan basin by orogenic loading and flexure of a rifted continental margin. J. Geophys. Res. 107. https://doi.org/10.1029/2001JB000669

Liu, S., 2020. Controls of Foreland-Deformation Patterns in the Orogen-Foreland Shortening System. Universität Potsdam. https://doi.org/10.25932/publishup-44573

Löbens, S., Bense, F.A., Wemmer, K., Dunkl, I., Costa, C.H., Layer, P., Siegesmund, S., 2011. Exhumation and uplift of the Sierras Pampeanas: preliminary implications from K–Ar fault gouge dating and low-T thermochronology in the Sierra de Comechingones (Argentina). Int. J. Earth Sci. 100, 671–694.

https://doi.org/https://doi.org/10.1007/s00531-010-0608-0

Lowe, C., Ranalli, G., 1993. Density, temperature, and rheological models for the southeastern Canadian Cordillera: implications for its geodynamic evolution. Can. J. Earth Sci. 30, 77–93.

Lowell, R.P., Kolandaivelu, K., Rona, P.A., 2014. Hydrothermal Activity. Ref. Modul. Earth Syst. Environ. Sci. 1–19. https://doi.org/10.1016/B978-0-12-409548-9.09132-6

Lucassen, F., Becchio, R., Harmon, R., Kasemann, S., Franz, G., Trumbull, R., Wilke, H.-G., Romer, R.L., Dulski, P., 2001. Composition and density model of the continental crust at an active continental margin - the Central Andes between 21° and 27°S. Tectonophysics 341, 195–223. https://doi.org/10.1016/S0040-1951(01)00188-3

Lucassen, F., Becchio, R., Wilke, H.G., Franz, G., Thirlwall, M.F., Viramonte, J., Wemmer, K., 2000. Proterozoic-Paleozoic development of the basement of the Central Andes (18-26°S) - A mobile belt of the South American craton. J. South Am. Earth Sci. 13, 697–715. https://doi.org/10.1016/S0895-9811(00)00057-2

Lucassen, F., Escayola, M., Romer, R.L., Viramonte, J., Koch, K., Franz, G., 2002. Isotopic composition of Late Mesozoic basic and ultrabasic rocks from the Andes “23-32°S” - Implications for the Andean mantle. Contrib. to Mineral. Petrol. 143, 336–349. https://doi.org/10.1007/s00410-001-0344-3

Lucassen, F., Franz, G., 2005. The early Palaeozoic Orogen in the Central Andes: a non-collisional orogen comparable to the Cenozoic high plateau? Geol. Soc. London, Spec. Publ. 246, 257–273. https://doi.org/10.1144/GSL.SP.2005.246.01.09

Lucassen, F., Franz, G., Viramonte, J., Romer, R.L., Dulski, P., Lang, A., 2005. The late Cretaceous lithospheric mantle beneath the Central Andes: Evidence from phase equilibria and composition of mantle xenoliths. Lithos 82, 379–406. https://doi.org/10.1016/j.lithos.2004.08.002

Lucassen, F., Kramer, W., Bartsch, V., Wilke, H.G., Franz, G., Romer, R.L., Dulski, P., 2006. Nd, Pb, and Sr isotope composition of juvenile magmatism in the Mesozoic large magmatic province of northern Chile (18-27°S): Indications for a uniform subarc mantle. Contrib. to Mineral. Petrol. 152, 571–589. https://doi.org/10.1007/s00410-006-0119-y

Lucassen, F., Lewerenz, S., Franz, G., Viramonte, J., Mezger, K., 1999. Metamorphism, isotopic ages and composition of lower crustal granulite xenoliths from the Cretaceous Salta Rift, Argentina. Contrib. to Mineral. Petrol. 134, 325–341. https://doi.org/10.1007/s004100050488

Maggi, A., Jackson, J.A., McKenzie, D., Priestley, K., 2000a. Earthquake focal depths, effective elastic thickness, and the strength of the continental lithosphere. Geology 28, 495–498. https://doi.org/10.1130/0091-7613(2000)28<495:efdeet>2.0.co;2

Maggi, A., Jackson, J.A., Priestley, K., Baker, C., 2000b. A re-assessment of focal depth distributions in southern Iran, the Tien Shan and northern India: Do earthquakes really occur in the continental mantle? Geophys. J. Int. 143, 629–661. https://doi.org/10.1046/j.1365-246X.2000.00254.x

Magrin, A., Rossi, G., 2020. Deriving a New Crustal Model of Northern Adria: The Northern Adria Crust (NAC) Model. Front. Earth Sci. 8. https://doi.org/doi: 10.3389/feart.2020.00089

Maloney, K.T., Clarke, G.L., Klepeis, K.A., Quevedo, L., 2013. The Late Jurassic to present evolution of the Andean margin: Drivers and the geological record. Tectonics 32, 1049–1065. https://doi.org/10.1002/tect.20067

Mareschal, J.-C., 1994. Thermal regime and post-orogenic extension in collision belts. Tectonophysics 238, 471–484.

Marquillas, R.A., del Papa, C., Sabino, I.F., 2005. Sedimentary aspects and paleoenvironmental evolution of a rift basin: Salta Group (Cretaceous-Paleogene), northwestern Argentina. Int. J. Earth Sci. 94, 94–113. https://doi.org/10.1007/s00531-004-0443-2

Marquillas, R.A., Salfity, J.A., 1988. Tectonic framework and correlations of the Cretaceous-Eocene Salta Group: Argentina, in: Bahlburg, H., Breitkreuz, C., Giese, P. (Eds.), The Southern Central Andes. Lecture Notes in Earth Sciences, Vol 17. Springer-Verlag, Berlin Heidelberg New York, pp. 119–136.

Marshak, S., Nelson, W.J., McBride, J.H., 2003. Phanerozoic strike-slip faulting in the continental interior platform of the United States: examples from the Laramide Orogen, Midcontinent, and Ancestral Rocky Mountains. Geol. Soc. London Spec. Publ. 210, 159–184. https://doi.org/10.1144/GSL.SP.2003.210.01.10

Masek, J.., Isacks, B.L., Gubbels, T.., Fielding, E.., 1994. Erosion and tectonics at the margins of continental plateaus. Jounral Geophys. Res. 99, 13941–13956. https://doi.org/10.1029/94JB00461

Maus, S., Barckhausen, U., Berkenbosch, H., Bournas, N., Brozena, J., Childers, V., Dostaler, F., Fairhead, J., Finn, C., von Frese, R., Gaina, C., Golynsky, S., Kucks, R., Lühr, H., Milligan, P., Mogren, S., Müller, R., Olesen, O., Pilkington, M., Saltus, R., Schreckenberger, B., Thébault, E., Caratori Tontini, F., 2009. EMAG2: A 2–arc min resolution Earth Magnetic Anomaly Grid compiled from satellite, airborne, and marine magnetic measurements. Geochemistry Geophys. Geosystems 10. https://doi.org/doi: 10.1029/2009GC002471

McKenzie, D., Jackson, J., Priestley, K., 2005. Thermal structure of oceanic and continental lithosphere. Earth Planet. Sci. Lett. 233, 337–349. https://doi.org/10.1016/j.epsl.2005.02.005

McLeod, C.L., Davidson, J.P., Nowell, G.M., de Silva, S.L., Schmitt, A.K., 2013. Characterizing the continental basement of the central andes: Constraints from bolivian crustal xenoliths. Bull. Geol. Soc. Am. 125, 985–997. https://doi.org/10.1130/B30721.1

McQuarrie, N., Horton, B.K., Zandt, G., Beck, S.L., Decelles, P.G., 2005. Lithospheric evolution of the Andean fold-thrust belt, Bolivia, and the origin of the central Andean plateau. Tectonophysics 399, 15–37. https://doi.org/doi:10.1016/j.tecto.2004.12.013

Meeßen, C., 2019. pyGMS: lithosphere-scale rheological analyses of GMS models in Python (Version v1.0.0). https://doi.org/10.5281/zenodo.3338066

Meeßen, C., 2017. VelocityConversion. V. v1.0.1. GFZ Data Services. https://doi.org/10.5880/GFZ.6.1.2017.001

Meeßen, C., Sippel, J., Scheck-Wenderoth, M., Heine, C., Strecker, M.R., 2018. Crustal Structure of the Andean Foreland in Northern Argentina: Results From Data-Integrative Three-Dimensional Density Modeling. J. Geophys. Res. Solid Earth 123, 1875–1903. https://doi.org/10.1002/2017JB014296

Meigs, A.J., Nabelek, J., 2010. Crustal-scale pure shear foreland deformation of western Argentina. Geophys. Res. Lett. 37, L11304. https://doi.org/10.1029/2010GL043220

Meissner, R., Strehlau, J., 1982. Limits of stresses in continental crust and their relation to the depth-frequency distribution of shallow eartquakes. Tectonics 1, 73–89. https://doi.org/10.1029/TC001i001p00073

Metcalf, K., Kapp, P., 2015. Along-strike variations in crustal seismicity and modern lithospheric structure of the central Andean forearc, in: DeCelles, P.G., Ducea, M.N., Carrapa, B., Kapp, P. (Eds.), Geodynamics of a Cordilleran Orogenic System: The Central Andes of Argentina and Northern Chile. Geological Society of America. https://doi.org/10.1130/2015.1212(04)

Mingramm, A., Russo, A., Pozzo, A., Cazau, L., 1979. Sierras Subandinas, in: Turner, J.C.M. (Ed.), Geología Regional Argentina, Vol. 1. Academia Nacional de Ciencias, Córdoba, pp. 95–138.

Moisio, K., Kaikkonen, P., 2015. Stress, rheological structure and earthquakes in the POLAR profile in the northern Fennoscandian Shield. Int. J. Earth Sci. 104, 221–239. https://doi.org/10.1007/s00531-014-1061-2

Molnar, P., England, P., Martinod, J., 1993. Mantle dynamics, uplift of the Tibetan Plateau, and the Indian Monsoon. Rev. Geophys. 31, 357–396. https://doi.org/10.1029/93RG02030

Molnar, P., Lyon-Caen, H., 1988. Some simple physical aspects of the support, structure, and evolution of mountain belts, in: Clark Jr, S.P., Clark Burchfiel, B., Suppe, J. (Eds.),

Processes in Continental Lithospheric Deformation. Geological Society of America, pp. 179–208. https://doi.org/10.1130/SPE218-p179

Molnar, P., Tapponnier, P., 1975. Cenozoic Tectonics of Asia: Effects of a Continental Collision. Science (80-.). 189, 419–426. https://doi.org/10.1126/science.189.4201.419

Mon, R., Salfity, J.A., 1995. Tectonic evolution of the Andes of northern Argentina, in: Tankard, A.J., Suarez Soruco, R., Welsink, H.J. (Eds.), Petroleum Basins of South America. AAPG Memoir, vol. 62, pp. 269–283.

Montero-López, C., Hongn, F., López Steinmetz, R.L., Aramayo, A., Pingel, H., Strecker, M.R., Cottle, J.M., Bianchi, C., 2020. Development of an incipient Paleogene topography between the present-day Eastern Andean Plateau (Puna) and the Eastern Cordillera, southern Central Andes, NW Argentina. Basin Res. 00, 1–24. https://doi.org/10.1111/bre.12510

Montero López, C., Strecker, M.R., Schildgen, T.F., Hongn, F., Guzmán, S., Bookhagen, B., Sudo, M., 2014. Local high relief at the southern margin of the Andean plateau by 9 Ma: evidence from ignimbritic valley fills and river incision. Terra Nov. 26, 454–460. https://doi.org/10.1111/ter.12120

Mooney, W.D., Ritsema, J., Hwang, Y.K., 2012. Crustal seismicity and the earthquake catalog maximum moment magnitude (Mcmax) in stable continental regions (SCRs): Correlation with the seismic velocity of the lithosphere. Earth Planet. Sci. Lett. 357–358, 78–83. https://doi.org/10.1016/j.epsl.2012.08.032

Mpodozis, C., Ramos, V.A., 1989. The Andes of Chile and Argentina, in: Ericksen, G.E., Cañas, M.T., Reinemud, J.A. (Eds.), Geology of the Andes and Its Relation to Hydrocarbon and Mineral Resources. Circumpacific Council for Energy and Mineral Resources, Volume 11, pp. 59–90.

Mulcahy, P., Chen, C., Kay, S.M., Brown, L.D., Isacks, B.L., Sandvol, E., Heit, B., Yuan, X., Coira, B.L., 2014. Central Andean mantle and crustal seismicity beneath the Southen Puna plateau and the northern margin of the Chilean-Pampean flat slab. Tectonics 33, 1636–1658. https://doi.org/10.1002/2013TC003393

New, M., Lister, D., Hulme, M., Makin, I., 2002. A high-resolution data set of surface climate over global land areas. Clim. Res. 21, 1–25. https://doi.org/10.3354/cr021001

Norini, G., Baez, W., Becchio, R., Viramonte, J., Giordano, G., Arnosio, M., Pinton, A., Groppelli, G., 2013. The Calama-Olacapato-El Toro fault system in the Puna Plateau, Central Andes: Geodynamic implications and stratovolcanoes emplacement. Tectonophysics 608, 1280–1297. https://doi.org/10.1016/j.tecto.2013.06.013

Nwankwo, L.I., Shehu, A.T., 2015. Evaluation of Curie-point depths, geothermal gradients and near-surface heat flow from high-resolution aeromagnetic (HRAM) data of the

entire Sokoto Basin, Nigeria. J. Volcanol. Geotherm. Res. 305, 45–55. https://doi.org/10.1016/j.jvolgeores.2015.09.017

Nyblade, A., Langston, C., 1995. East African earthquakes below 20 km and their implications for crustal structure. Geophys. J. Int. 121, 49–62. https://doi.org/10.1111/j.1365-246X.1995.tb03510.x

Okubo, Y., Graf, R.J., Hansen, R.O., Ogawa, K., Tsu, H., 1985. Curie point depths of the Island of Kyushu and surrounding areas, Japan. Geophysics. https://doi.org/10.1190/1.1441926

Oncken, Onno, Chong, G., Franz, G., Giese, P., Götze, H.-J., Ramos, V.A., Strecker, M.R., Wigger, P., 2006. The Andes: Active Subduction Orogeny. Springer-Verlag Berlin Heidelberg. https://doi.org/10.1007/978-3-540-48684-8

Oncken, O., Hindle, D., Kley, J., Elger, K., Victor, P., Schemmann, K., 2006. Deformation of the central Andean upper plate system—Facts, fiction, and constraints for plateau models, in: Oncken, O., Chong, G., Franz, G., Giese, P., Götze, H.-J., Ramos, V.A., Strecker, M.R., Wigger, P. (Eds.), The Andes: Active Subduction Orogeny. Berlin, Springer-Verlag, Frontiers in Earth Science Series, pp. 3–27.

Ouimet, W.B., Cook, K.L., 2010. Building the central Andes through axial lower crustal flow. Tectonics 29, TC3010. https://doi.org/10.1029/2009TC002460

Pankhurst, R.J., Rapela, C.W., 1998. The Proto-Andean margin of Gondwana. Geol. Soc. London Spec. Publ. 142.

Pankhurst, R.J., Rapela, C.W., Fanning, C.M., 2000. Age and origin of coeval TTG, I- and S-type granites in the Famatinian belt of NW Argentina. Trans. R. Soc. Edinb. Earth Sci. 91, 151–168. https://doi.org/10.1017/S0263593300007343

Pavlenkova, N.I., Pilipenko, V.N., Verpakhovskaja, A.O., Pavlenkova, G.A., Filonenko, V.P., 2009. Crustal structure in Chile and Okhotsk Sea regions. Tectonophysics 472, 28–38. https://doi.org/10.1016/j.tecto.2008.08.018

Peacock, S.M., 1996. Thermal and petrologic structure of subduction zones, in: Bebout, G.E., Scholl, D.W., Kirby, S.H., Platt, J.P. (Eds.), Subduction: Top to Bottom. AGU Geophysical Monograph, Washington D. C., pp. 119–133.

Petley-Ragan, A., Ben-Zion, Y., Austrheim, H., Ildefonse, B., Renard, F., Jamtveit, B., 2019. Dynamic earthquake rupture in the lower crust. Sci. Adv. 5, EAAW0913. https://doi.org/10.1126/sciadv.aaw0913

Pingel, H., Strecker, M.R., Mulch, A., Alonso, R.N., Cottle, J., Rohrmann, A., 2020. Late Cenozoic topographic evolution of the Eastern Cordillera and Puna Plateau margin in the southern Central Andes (NW Argentina). Earth Planet. Sci. Lett. 535, 116112. https://doi.org/10.1016/j.epsl.2020.116112

Platt, J.P., England, P., 1994. Convective removal of lithosphere beneath mountain belts: thermal and mechanical consequences. Am. J. Sci. 294, 307–336. https://doi.org/10.2475/ajs.294.3.307

Prezzi, C., Iglesia Llanos, M.P., Götze, H.J., Schmidt, S., 2014. Thermal and geodynamic contributions to the elevation of the Altiplano-Puna plateau. Phys. Earth Planet. Inter. 237, 51–64. https://doi.org/10.1016/j.pepi.2014.10.002

Prezzi, C.B., Götze, H.J., Schmidt, S., 2009. 3D density model of the Central Andes. Phys. Earth Planet. Inter. 177, 217–234. https://doi.org/10.1016/j.pepi.2009.09.004

Prieto, G.A., Froment, B., Yu, C., Poli, P., Abercrombie, R., 2017. Earthquake rupture below the brittle-ductile transition in continental lithospheric mantle. Sci. Adv. 3, E1602642. https://doi.org/10.1126/sciadv.1602642

Proyecto Multinacional Andino: Geociencia para las Comunidades Andinas, 2008. Atlas de deformaciones cuaternarias de los Andes. Servicio Nacional de Geología y Minería, Publicación Geológica Multinacional, No. 7, 320 p.

Quade, J., Dettinger, M.P., Carrapa, B., Decelles, P., Murray, K.E., Huntington, K.W., Cartwright, A., Canavan, R.R., Gehrels, G., Clementz, M., 2015. The growth of the central Andes, 22° S-26° S, in: DeCelles, P.G., Ducea, M.N., Carrapa, B., Kapp, P.A. (Eds.), Geodynamics of a Cordilleran Orogenic System: The Central Andes of Argentina and Northern Chile. Geological Society of America, pp. 277–308. https://doi.org/10.1130/2015.1212(15)

Ramos, V.A., 2010. The tectonic regime along the Andes: Present-day and Mesozoic regimes. Geol. J. 45, 2–25. https://doi.org/10.1002/gj.1193

Ramos, V.A., 2009. Anatomy and global context of the Andes: Main geologic features and the Andean orogenic cycle, in: Kay, S.M., Ramos, V.A., Dickinson, W. (Eds.), Backbone of the Americas: Shallow Subduction, Plateau Uplift, and Ridge and Terrane Collision. Geological Society of America, pp. 31–65. https://doi.org/10.1130/MEM204

Ramos, V.A., 2008. The Basement of the Central Andes: The Arequipa and Related Terranes. Annu. Rev. Earth Planet. Sci. 36, 289–324. https://doi.org/10.1146/annurev.earth.36.031207.124304

Ramos, V.A., 1999. Las provincias geológicas del territorio argentino, in: Caminos, R. (Ed.), Geología Argentina. Instituto de Geología y Recursos Minerales, Anales 29, pp. 41–96.

Ramos, V.A., Cristallini, E.O., Perez, D.J., 2002. The Pampean flat-slab of the Central Andes. J. South Am. Earth Sci. 15, 59–78. https://doi.org/10.1016/S0895-9811(02)00006-8

Ramos, V.A., Vujovich, G., Martino, R., Otamendi, J., 2010. Pampia: A large cratonic block missing in the Rodinia supercontinent. J. Geodyn. 50, 243–255.

https://doi.org/10.1016/j.jog.2010.01.019

Ranalli, G., 2003. How soft is the crust? Tectonophysics 361, 319–320. https://doi.org/10.1016/S0040-1951(02)00607-8

Ranalli, G., 1997. Rheology of the lithosphere in space and time, in: Burg, J.-P., Ford, M. (Eds.), Orogeny Through Time. Geological Society of London Special Publications, pp. 19–37. https://doi.org/10.1144/GSL.SP.1997.121.01.02

Ranalli, G., 1995. Rheology of the Earth, Second Edi. ed. Chapman & Hall.

Ranalli, G., Adams, M., 2013. Rheological contrast at the continental Moho: Effects of composition, temperature, deformation mechanism, and tectonic regime. Tectonophysics 609, 480–490. https://doi.org/10.1016/j.tecto.2012.10.037

Ranalli, G., Murphy, D.C., 1987. Rheological stratification of the lithosphere. Tectonophysics 132, 281–295. https://doi.org/10.1016/0040-1951(87)90348-9

Rapalini, A.E., 2005. The accretionary history of southern South America from the latest Proterozoic to the Late Palaeozoic: some palaeomagnetic constraints. Geol. Soc. London, Spec. Publ. 246, 305–328. https://doi.org/10.1144/GSL.SP.2005.246.01.12

Rapela, C.W., Pankhurst, R.J., Casquet, C., Dahlquist, J.A., Fanning, C.M., Baldo, E.G., Galindo, C., Alasino, P.H., Ramacciotti, C.D., Verdecchia, S.O., Murra, J.A., Basei, M.A.S., 2018. A review of the Famatinian Ordovician magmatism in southern South America : evidence of lithosphere reworking and continental subduction in the early proto-Andean margin of Gondwana. Earth-Science Rev. 187, 259–285. https://doi.org/10.1016/j.earscirev.2018.10.006

Rapela, C.W., Pankhurst, R.J., Casquet, C., Fanning, C.M., Baldo, E.G., González-Casado, J.M., Galindo, C., Dahlquist, J., 2007. The Río de la Plata craton and the assembly of SW Gondwana. Earth-Science Rev. 83, 49–82.

Rapela, C.W., Verdecchia, S.O., Casquet, C., Pankhurst, R.J., Baldo, E.G., Galindo, C., Murra, J.A., Dahlquist, J.A., Fanning, C.M., 2016. Identifying Laurentian and SW Gondwana sources in the Neoproterozoic to Early Paleozoic metasedimentary rocks of the Sierras Pampeanas: Paleogeographic and tectonic implications. Gondwana Res. 32, 193–212. https://doi.org/10.1016/j.gr.2015.02.010

Reutter, K.-J., Charrier, R., Götze, H.-J., Schurr, B., Wigger, P., Scheuber, E., Giese, P., Reuther, C.-D., Schmidt, S., Rietbrock, A., Chong, G., Belmonte-Pool, A., 2006. The Salar de Atacama Basin: a Subsiding Block within the Western Edge of the Altiplano-Puna Plateau. The Andes 303–325. https://doi.org/10.1007/978-3-540-48684-8_14

Reynolds, R.W., Smith, T.M., Liu, C., Chelton, D.B., Casey, K.S., Schlax, M.G., 2007. Daily high-resolution-blended analyses for sea surface temperature. J. Clim. 20, 5473–5496. https://doi.org/10.1016/S0012-821X(01)00333-8

Richter, F.., Rowley, D.., DePaolo, D.J., 1992. Sr isotope evolution of seawater: the role of tectonics. Earth Planet. Sci. Lett. 109, 11–23. https://doi.org/10.1016/0012-821X(92)90070-C

Rietbrock, A., Asch, G., Chong, G., Giese, P., 1997. ANCORP '96—Seismicity along the ANCORP traverse in northern Chile. Eos, Trans. Am. Geophys. Union 78(46).

Riller, U., Cruden, A.R., Boutelier, D., Schrank, C.E., 2012. The causes of sinuous crustal-scale deformation patterns in hot orogens : Evidence from scaled analogue experiments and the southern Central Andes. J. Struct. Geol. 37, 65–74. https://doi.org/10.1016/j.jsg.2012.02.002

Riller, U., Petrinovic, I., Ramelow, J., Strecker, M.R., Oncken, O., 2001a. Late Cenozoic tectonism, collapse caldera and plateau formation in the central Andes. Earth Planet. Sci. Lett. 188, 299–311.

Riller, U., Petrinovic, I., Ramelow, J., Strecker, M.R., Oncken, O., 2001b. Late Cenozoic tectonism, collapse caldera and plateau formation in the central Andes. Earth Planet. Sci. Lett. 188, 299–311. https://doi.org/10.1016/S0012-821X(01)00333-8

Risse, A., Trumbull, R.B., Kay, S.M., Coira, B., Romer, R.L., 2013. Multi-stage evolution of late neogene mantle-derived magmas from the central andes back-arc in the southern Puna plateau of Argentina. J. Petrol. 54, 1963–1995. https://doi.org/10.1093/petrology/egt038

Rosa, M.L., Collaço, B., Assumpção, M., Sabbione, N., Sánchez, G., 2016. Thin crust beneath the Chaco-Paraná Basin by surface-wave tomography. J. South Am. Earth Sci. 66, 1–14. https://doi.org/10.1016/j.jsames.2015.11.010

Rossel, P., Oliveros, V., Ducea, M.N., Charrier, R., Scaillet, S., Retamal, L., Figueroa, O., 2013. The Early Andean subduction system as an analog to island arcs: Evidence from across-arc geochemical variations in northern Chile. Lithos 179, 211–230. https://doi.org/10.1016/j.lithos.2013.08.014

Royden, L., 1996. Coupling and decoupling of crust and mantle in convergent orogens: implications for strain partitioning in the crust. Jounral Geophys. Res. 101, 17679–17705. https://doi.org/10.1029/96JB00951

Ruddiman, W.F., Raymo, M.E., Prell, W.L., Kutzbach, J.E., 1997. The uplift-climate connection: a synthesis, in: Ruddiman, W.F. (Ed.), Tectonic Uplift and Climate Change. Springer, Boston, MA, pp. 471–515. https://doi.org/10.1007/978-1-4615-5935-1_20

Russo, R., Silver, P.G., 1996. Cordillera formation, mantle dynamics, and the Wilson cycle. Geology 24, 511–514. https://doi.org/10.1130/0091-7613(1996)024<0511:CFMDAT>2.3.CO;2

Ryan, J., Beck, S., Zandt, G., Wagner, L., Minaya, E., Tavera, H., 2016. Central Andean

crustal structure from receiver function analysis. Tectonophysics 682, 120–133. https://doi.org/10.1016/j.tecto.2016.04.048

Salomon, C., 2018. Finite element modelling of the geodynamic processes of the Central Andes subduction zone: A Reference Model. Geod. Geodyn. 9, 246–251. https://doi.org/10.1016/j.geog.2017.11.007

Sandiford, M., McLaren, S., 2002. Tectonic feedback and the ordering of heat producing elements within the continental lithosphere. Earth Planet. Sci. Lett. 204, 133–150. https://doi.org/10.1016/S0012-821X(02)00958-5

Santibáñez, I., Cembrano, J., García-Pérez, T., Costa, C., Yáñez, G., Marquardt, C., Arancibia, G., González, G., 2019. Crustal faults in the Chilean Andes: geological constraints and seismic potential. Andean Geol. 46, 32–65. https://doi.org/10.5027/andgeoV46n1-3067

Schaeffer, A.J., Lebedev, S., 2013. Global shear speed structure of the upper mantle and transition zone. Geophys. J. Int. 194, 417–449. https://doi.org/10.1093/gji/ggt095

Scheck-Wenderoth, M., Maystrenko, Y.P., 2013. Deep control on shallow heat in sedimentary basins. Energy Procedia 40, 266–275. https://doi.org/10.1016/j.egypro.2013.08.031

Schellart, W.P., 2017. Andean mountain building and magmatic arc migration driven by subduction-induced whole mantle flow. Nat. Commun. 8. https://doi.org/10.1038/s41467-017-01847-z

Schemmann, K., 2007. Scale-related strain evolution at convergent margins and effects due to parameter changes - insights from nature and experiment. PhD Thesis, (Scientific Technical Report STR ; 07/09), Potsdam : Deutsches GeoForschungsZentrum GFZ, Getr. Zählung p. https://doi.org/10.1007/s004100000214

Scheuber, E., Bogdanic, T., Jensen, A., Reutter, K., 1994. Tectonic development of the north Chilean Andes in relation to plate convergence and magmatism since the Jurassic, in: Reutter, K., Scheuber, E., Wigger, P. (Eds.), Tectonics of the Southern Central Andes. Berlin Heidelberg New York, pp. 7–22.

Scheuber, E., Reutter, K., 1992. Magmatic arc tectonics in the Central Andes between 21° and 25°S. Tectonophysics 205, 127–140. https://doi.org/10.1134/S1023193511090047

Schilling, F.R., Trumbull, R.B., Brasse, H., Haberland, C., Asch, G., Bruhn, D., Mai, K., Haak, V., Giese, Peter, Muñoz, M., Ramelow, J., Rietbrock, A., Ricaldi, E., Vietor, T., 2006. Partial Melting in the Central Andean Crust: a Review of Geophysical, Petrophysical, and Petrologic Evidence, in: Oncken, O., Chong, G., Franz, G., Giese, P., Götze, H.-J., Ramos, V.A., Strecker, M.R., Wigger, P. (Eds.), The Andes: Active Subduction Orogeny.

Springer-Verlag Berlin Heidelberg, pp. 459–474.

Schmidt, S., Plonka, C., Götze, H.J., Lahmeyer, B., 2011. Hybrid modelling of gravity, gravity gradients and magnetic fields. Geophys. Prospect. 59, 1046–1051. https://doi.org/10.1111/j.1365-2478.2011.00999.x

Schmitt, A., de Silva, S., Trumbull, R., Emmermann, R., 2001. Magma evolution in the Purico ignimbrite complex, northern Chile: evidence for zoning of a dacitic magma by injection of rhyolitic melts following mafic recharge. Contrib. to Mineral. Petrol. 140, 680–700. https://doi.org/10.1007/s004100000214

Schmitz, M., Kley, J., 1997. The Geometry of the Central Andean Backarc Crust: Joint Interpretation of Cross-section Balancing and Seismic Refraction Data. J. South Am. Earth Sci. 10, 99–110.

Schoenbohm, L., Strecker, M.R., 2009. Normal faulting along the southern margin of the Puna Plateau, northwest Argentina. Tectonics 28, TC5008. https://doi.org/10.1029/2008TC002341

Schoenbohm, L.M., Strecker, M.R., 2009. Normal faulting along the southern margin of the Puna Plateau, northwest Argentina. Tectonics 28, TC5008. https://doi.org/10.1029/2008TC002341

Scholz, C.H., 1988. The brittle-plastic transition and the depth of seismic faulting. Geol. Rundschau 77, 319–328. https://doi.org/10.1007/BF01848693

Schurr, B., Asch, G., Rietbrock, A., Kind, R., Pardo, M., Heit, B., Monfret, T., 1999. Seismicity and average velocities beneath the Argentine Puna Plateau. Geophys. Res. Lett. 26, 3025–3028. https://doi.org/10.1029/1999GL005385

Schurr, B., Asch, G., Rietbrock, A., Trumbull, R., Haberland, C., 2003. Complex patterns of fluid and melt transport in the central Andean subduction zone revealed by attenuation tomography. Earth Planet. Sci. Lett. 215, 105–119. https://doi.org/10.1016/S0012-821X(03)00441-2

Schurr, B., Rietbrock, A., 2004. Deep seismic structure of the Atacama basin, northern Chile. Geophys. Res. Lett. 31, 10–13. https://doi.org/10.1029/2004GL019796

Schurr, B., Rietbrock, A., Asch, G., Kind, R., Oncken, O., 2006. Evidence for lithospheric detachment in the central Andes from local earthquake tomography. Tectonophysics 415, 203–223. https://doi.org/10.1016/j.tecto.2005.12.007

Siame, L.L., Sébrier, M., Bellier, O., Bourlès, D., Costa, C.H., Ahumada, E.A., Gardini, C.E., Cisneros, H., 2015. Active basement uplift of Sierra Pie de Palo (Northwestern Argentina): Rates and inception from 10Be cosmogenic nuclide concentrations. Tectonics 34, 1129–1153. https://doi.org/10.1002/2014TC003771

Sibson, R.H., 1982. Fault zone models, heat flow and the depth distribution of earthquakes

in the continental crust of the United States. Bull. Seismol. Soc. Am. 72, 151–163.

Siks, B.C., Horton, B.K., 2011. Growth and fragmentation of the Andean foreland basin during eastward advance of fold-thrust deformation, Puna plateau and Eastern Cordillera, northern Argentina. Tectonics 30, 1–27. https://doi.org/10.1029/2011TC002944

Sillitoe, R.H., 1972. Relation of metals provinces in western America to subduction of oceanic lithosphere. Geol. Soc. Am. Bull. 83, 813–818. https://doi.org/10.1130/0016-7606(1972)83[813:ROMPIW]2.0.CO;2

Sloan, R.A., Jackson, J.A., Mckenzie, D., Priestley, K., 2011. Earthquake depth distributions in central Asia, and their relations with lithosphere thickness, shortening and extension. Geophys. J. Int. 185, 1–29. https://doi.org/10.1111/j.1365-246X.2010.04882.x

Sobel, E.R., Strecker, M.R., 2003. Uplift, exhumation and precipitation: Tectonic and climatic control of Late Cenozoic landscape evolution in the northern Sierras Pampeanas, Argentina. Basin Res. 15, 431–451. https://doi.org/10.1046/j.1365-2117.2003.00214.x

Sobolev, S. V., Babeyko, A.Y., 2005. What drives orogeny in the Andes? Geology 33, 617–620. https://doi.org/10.1130/G21557.1

Sobolev, S. V., Zeyen, H., Stoll, G., Werling, F., Altherr, R., Fuchs, K., 1996. Upper mantle temperatures from teleseismic tomography of French Massif Central including effects of composition, mineral reactions, anharmonicity, anelasticity and partial melt. Earth Planet. Sci. Lett. 139, 147–163. https://doi.org/10.1016/0012-821X(95)00238-8

Soler, S., 2015. Métodos Espectrales para la Determinación de la Profundidad del Punto de Curie y el Espesor Elástico de la Corteza Terrestre. Tesina Grado. Univ. Nac. Rosario.

Somoza, R., 1988. Updated Nazca (Farallon)—South America relative motions during the last 40 m.y.: Implications for mountain building in the central Andean region. J. South Am. Earth Sci. 11, 211–215. https://doi.org/10.1016/S0895-9811(98)00012-1

Spector, A., Grant, F.S., 1970. Statistical Models for Interpreting Aeromagnetic Data. Geophysics. https://doi.org/10.1190/1.1440092

Springer, M., 1999. Interpretation of heat-flow density in the Central Andes. Tectonophysics 306, 377–395. https://doi.org/10.1016/S0040-1951(99)00067-0

Springer, M., Förster, A., 1998. Heat-flow density across the central Andean subduction zone. Tectonophysics 291, 123–139. https://doi.org/10.1016/S0040-1951(98)00035-3

Stern, C.R., 2004. Active Andean volcanism: its geologic and tectonic setting. Rev. geológica Chile 31, 161–206.

Strecker, M.R., Cerveny, P., Bloom, A.L., Malizia, D., 1989. Late Cenozoic tectonism and landscape development in the foreland of the Andes: Northern Sierras Pampeanas (26°-28°S), Argentina. Tectonics 8, 517–534. https://doi.org/10.1029/TC008i003p00517

Stüwe, K., 2007. Goedynamics of the Lithosphere. An Introduction, 2nd ed. Springer-Verlag Berlin Heidelberg. https://doi.org/10.1007/978-3-540-71237-4

Swenson, J.L., Beck, S.L., Zandt, G., 2000. Crustal structure of the Altiplano from broadband regional waveform modeling: Implications for the composition of thick continental crust. J. Geophys. Res. 105, 607. https://doi.org/10.1029/1999JB900327

Tanaka, A., Okubo, Y., Matsubayashi, O., 1999. Curie point depth based on spectrum analysis of the magnetic anomaly data in East and Southeast Asia. Tectonophysics 306, 461–470. https://doi.org/10.1016/S0040-1951(99)00072-4

Tassara, A., Götze, H.J., Schmidt, S., Hackney, R., 2006. Three-dimensional density model of the Nazca plate and the Andean continental margin. J. Geophys. Res. Solid Earth 111, B09404. https://doi.org/10.1029/2005JB003976

Tassara, A., Yáñez, G., 2003. Relación entre el espesor elástico de la litosfera y la segmentación tectónica del margen andino (15-47°S). Rev. geológica Chile 30, 1–27. https://doi.org/10.4067/S0716-02082003000200002

Tatsumi, Y., 1986. Formation of volcanic front in subduction zones. Geophys. Res. Lett. 13, 717–720. https://doi.org/10.1029/GL013i008p00717

Tesauro, M., Kaban, M.K., Cloetingh, S.A.P.L., 2013. Global model for the lithospheric strength and effective elastic thickness. Tectonophysics 602, 78–86. https://doi.org/10.1016/j.tecto.2013.01.006

Tesauro, M., Kaban, M.K., Mooney, W.D., 2015. Variations of the lithospheric stregth and elastic thickness in North America. Geochemistry Geophys. Geosystems 16, 2197–2220.

Thebault, E., Vervelidou, F., 2015. A statistical spatial power spectrum of the Earth's lithospheric magnetic field. Geophys. J. Int. 201, 605–620. https://doi.org/10.1093/gji/ggu463

Toselli, A.J., Rossi, J.N., Rapela, C.W., 1978. El basamento metamórfico de la Sierra de Quilmes, República Argentina. Asoc. Geológica Argentina Rev. 33, 105–112.

Trindade, R.I.F., D'Agrella-Filho, M.S., Epof, I., Brito Neves, B.B., 2006. Paleomagnetism of the early Cambrian Itabaiana mafic dikes, NE Brazil, and implications for the final assembly of Gondwana and its proximity to Laurentia. Earth Planet. Sci. Lett. 244, 361–377.

Trumbull, R.B., Riller, U., Oncken, O., Scheuber, E., Munier, K., Hongn, F., 2006. The time-

space distribution of Cenozoic arc volcanism in the southcentral Andes: A new data compilation and some tectonic implications, in: Oncken, O., Chong, G., Franz, G., Giese, P., Götze, H.-J., Ramos, V.A., Strecker, M.R., Wigger, P. (Eds.), The Andes: Active Subduction Orogeny. Springer-Verlag Berlin Heidelberg, pp. 29–44.

Tse, S.T., Rice, J.R., 1986. Crustal earthquake instability in relation to the depth variation of frictional slip properties. J. Geophys. Res. Solid Earth 91, 9452–9472. https://doi.org/10.1029/JB091iB09p09452

Vanderhaeghe, O., 2012. The thermal-mechanical evolution of crustal orogenic belts at convergent plate boundaries: A reappraisal of the orogenic cycle. J. Geodyn. 56–57, 124–145. https://doi.org/10.1016/j.jog.2011.10.004

Vanderhaeghe, O., Medvedev, S., Fullsack, P., Beaumont, C., Jamieson, R.A., 2003. Evolution of orogenic wedges and continental plateaux: insights from crustal thermal-mechanical models overlying subducting mantle lithosphere. Geophys. J. Int. 153, 27–51. https://doi.org/10.1046/j.1365-246X.2003.01861.x

Vauchez, A., Barruol, G., 1996. Shear-wave splitting in the Appalachians and the Pyrenees: importance of the inherited tectonic fabric of the lithosphere. Phys. Earth Planet. Inter. 95, 127–138. https://doi.org/10.1016/0031-9201(95)03125-1

Vauchez, A., Tommasi, A., Barruol, G., 1998. Rheological heterogeneity, mechanical anisotropy and deformation of the continental lithosphere. Tectonophysics 296, 61–86. https://doi.org/10.1016/S0040-1951(98)00137-1

Vilà, M., Fernández, M., Jiménez-Munt, I., 2010. Radiogenic heat production variability of some common lithological groups and its significance to lithospheric thermal modeling. Tectonophysics 490, 152–164. https://doi.org/10.1016/j.tecto.2010.05.003

Viramonte, J.G., Galliski, M.A., Araña Saavedra, V., Aparicio, A., Garcia Cacho, L., Martín Escorza, C., 1984. El finivolcanismo básico de la depresión de Arizaro, provincia de Salta. IX Congr. Geológico Argentino Actas 1 234–251.

Viramonte, J.G., Kay, S.M., Becchio, R., Escayola, M., Novitski, I., 1999. Cretaceous rift related magmatism in central-western South America. J. South Am. Earth Sci. 12, 109–121. https://doi.org/10.1016/S0895-9811(99)00009-7

Von Hillebrandt, A., Bartsch, V., Bebiolka, A., Kossler, A., Kramer, W., Wilke, H.G., Wittmann, S., 2000. The paleogeographic evolution in a volcanic-arc/back-arc setting during the Mesozoic in northern Chile. Zeitschrift für Angew. Geol. SH1 2000 87–93.

Ward, K.M., Porter, R.C., Zandt, G., Beck, S.L., Wagner, L.S., Minaya, E., Tavera, H., 2013. Ambient noise tomography across the Central Andes. Geophys. J. Int. 194, 1559–1573. https://doi.org/10.1093/gji/ggt166

Ward, K.M., Zandt, G., Beck, S.L., Christensen, D.H., McFarlin, H., 2014. Seismic imaging of

the magmatic underpinnings beneath the Altiplano-Puna volcanic complex from the joint inversion of surface wave dispersion and receiver functions. Earth Planet. Sci. Lett. 404, 43–53. https://doi.org/10.1016/j.epsl.2014.07.022

Wasilewski, P.J., Thomas, H.H., Mayhew, M.A., 1979. The Moho as a magnetic boundary. Geophys. Res. Lett. 6, 541–544.

Watts, A., Lamb, S., Fairhead, J., Dewey, J., 1995. Lithospheric flexure and bending of the Central Andes. Earth Planet. Sci. Lett. 134, 9–21.

Watts, A.B., 1988. Gravity anomalies, crustal structure and flexure of the lithosphere at the Baltimore Canyon Trough. Earth Planet. Sci. Lett. 88, 221–238. https://doi.org/10.1016/0012-821X(88)90174-4

Watts, A.B., Burov, E.B., 2003. Lithospheric strength and its relationship to the elastic and seismogenic layer thickness 213, 113–131. https://doi.org/10.1016/S0012-821X(03)00289-9

Weiss, J.R., Brooks, B.A., Arrowsmith, R., Vergani, G., 2015. Spatial and temporal distribution of deformation at the front of the Andean orogenic wedge in southern Bolivia. J. Geophys. Res. Solid Earth 120, 1909–1931. https://doi.org/10.1002/2014JB011763

Weiss, P., Foex, G., 1911. Étude de l'aimantation des corps ferromagnétiques au-dessus du point de Curie. J. Phys. Théorique Appliquée 1, 274–287.

Weston, J., Engdahl, E.R., Harris, J., Di Giacomo, D., Storchack, D.A., 2018. ISC-EHB: Reconstruction of a robust earthquake dataset. Geophys. J. Int. 214, 474–484. https://doi.org/doi: 10.1093/gji/ggy155

Whitman, D., Isacks, B.L., Kay, S.M., 1996. Lithospheric structure and along-strike segmentation of the Central Andean Plateau: seismic Q, magmatism, flexure, topography and tectonics. Tectonophysics 259, 29–40. https://doi.org/10.1016/0040-1951(95)00130-1

Wigger, P.J., Schmitz, M., Araneda, M., Asch, G., Baldzuhn, S., Giese, P., Heinsohn, W.-D., Martínez, E., Ricaldi, E., Röwer, P., Viramonte, J., 1994. Variation in the Crustal Structure of the Southern Central Andes Deduced from Seismic Refraction Investigations, in: Reutter, K.-J., Scheuber, E., Wigger, P.J. (Eds.), Tectonics of the Southern Central Andes. Springer-Verlag, pp. 23–48.

Wilks, K.R., Carter, N.L., 1990. Rheology of some continental lower crustal rocks. Tectonophysics 182, 57–77. https://doi.org/10.1016/0040-1951(90)90342-6

Wölbern, I., Heit, B., Yuan, X., Asch, G., Kind, R., Viramonte, J., Tawackoli, S., Wilke, H., 2009. Receiver function images from the Moho and the slab beneath the Altiplano and Puna plateaus in the Central Andes. Geophys. J. Int. 177, 296–308.

https://doi.org/10.1111/j.1365-246X.2008.04075.x

Wong, I.G., Chapman, D.S., 1990. Deep intraplate earthquakes in the western United States and their relationship to lithospheric temperatures. Bull. Seismol. Soc. Am. 80, 589–599.

Wörner, G., Lezaun, J., Beck, A., Heber, V., Lucassen, F., Zinngrebe, E., Rössling, R., Wilke, H.G., 2000. Precambrian and early Paleozoic evolution of the Andean basement at Belen (northern Chile) and Cerro Uyarani (western Bolivia Altiplano). J. South Am. Earth Sci. 13, 717–737. https://doi.org/10.1016/S0895-9811(00)00056-0

Yang, Y., Liu, M., 2003. A 3-D geodynamic model of lateral crustal flow during Andean mountain building. Geophys. Res. Lett. 30, 2093. https://doi.org/10.1029/2003GL018308

Yin, A., Harrison, M.T., 2000. Geologic Evolution of the Himalayan-Tibetan Orogen. Annu. Rev. Earth Planet. Sci. 28, 211–280. https://doi.org/10.1146/annurev.earth.28.1.211

Yuan, X., Sobolev, S. V., Kind, R., 2002. Moho topography in the Central Andes and its geodynamic implications. Earth Planet. Sci. Lett. 199, 389–402. https://doi.org/10.1016/S0012-821X(02)00589-7

Yuan, X., Sobolev, S. V., Kind, R., Oncken, O., Group, A.W., 2000. Subduction and collision processes in the Central Andes constrained by converted seismic phases. Nature 408, 958–961.

Zandt, G., Ammon, C.J., 1995. Continental crust composition constrained by measurements of crustal Poisson's ratio. Nature 374, 152–154.

Zandt, G., Leidig, M., Chmielowski, J., Baumont, D., Yuan, X., 2003. Seismic detection and characterization of the Altiplano-Puna magma body, Central Andes, in: Ben-Zion, Y. (Ed.), Seismic Motion, Lithospheric Structures, Earthquake and Volcanic Sources: The Keiiti Aki Volume. Birkhäuser, Basel, pp. 789–807. https://doi.org/10.1007/978-3-0348-8010-7_14

Zhou, R., Schoenbohm, L.M., 2015. Late Miocene upper-crustal deformation within the interior of the southern Puna Plateau, central Andes. Lithosphere 7, 336–352. https://doi.org/10.1130/L396.1

Zoback, M.D., Zoback, M. Lou, Mount, V.S., Suppe, J., Eaton, J.P., Healy, J.H., Oppenheimer, D., Reasenberg, P., Jones, L., Raleigh, C.B., Wong, I.G., Scotti, O., Wentworth, C., 1987. New evidence on the state of stress of the San Andreas fault system. Science (80-.). 238, 1105–1111.